

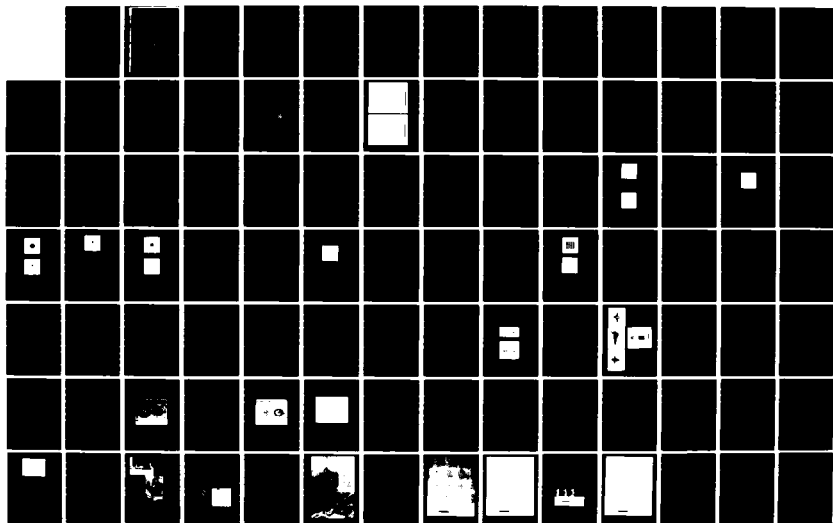
AD-A150 098

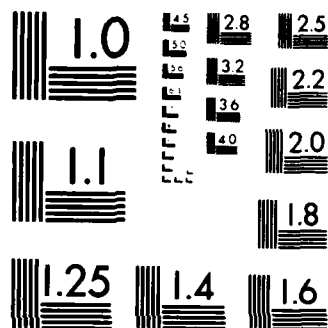
RESEARCH IN IMAGE UNDERSTANDING AS APPLIED TO 3-D
TOMOGRAPHIC IMAGING WIT. (U) MOORE SCHOOL OF ELECTRICAL
ENGINEERING PHILADELPHIA PA ELECTR. N H FARHAT ET AL.
30 NOV 84 EO/MO-7 AFOSR-TR-84-1230 F/G 17/9

1/2

UNCLASSIFIED

NL





MICROCOPY RESOLUTION TEST CHART
NATIONAL BUREAU OF STANDARDS-1963-A

AFOSR-TN- 84- 000



AD-A150 098

ANNUAL REPORT

IN IMAGE UNDERSTANDING AS APPLIED TO 3-D TOMO
IMAGING WITH NEAR OPTICAL RESOLUTION

Prepared for

AIR FORCE OFFICE OF SCIENTIFIC RESEARCH
BUILDING 410, BOLLING AIR FORCE BASE
Washington D.C. 20332



UNIVERSITY OF PENNSYLVANIA

UNIVERSITY of PENNSYLVANIA
The Moore School of Electrical Engineering
PHILADELPHIA, PENNSYLVANIA 19104

SECRET
A

Approved for public release;
distribution unlimited.

85 01 14 122

UNIVERSITY OF PENNSYLVANIA
THE MOORE SCHOOL OF ELECTRICAL ENGINEERING
ELECTRO-OPTICS AND MICROWAVE OPTICS LABORATORY
PHILADELPHIA, PA 19104

ANNUAL REPORT

RESEARCH IN IMAGE UNDERSTANDING AS APPLIED TO 3-D TOMOGRAPHIC
IMAGING WITH NEAR OPTICAL RESOLUTION

Prepared for

AIR FORCE OFFICE OF SCIENTIFIC RESEARCH
BUILDING 410, BOLLING AIR FORCE BASE
Washington, D.C. 20332

Under Grant

AFOSR 81-0240 C
7/1/83-8/31/84

Prepared by:

N. H. Farhat

Contributors:

T.H. Chu
Lie Szu Chang
N. Farhat
D. Jaggard
K. Schultz
C.L. Werner

23 85

November 30, 1984

EO/MO Report No. 7

UNCLASSIFIED

SECURITY CLASSIFICATION OF THIS PAGE (When Data Entered)

LT Col Carter

REPORT DOCUMENTATION PAGE		READ INSTRUCTIONS BEFORE COMPLETING FORM
1. REPORT NUMBER AEO/MO 7	2. GOVT ACCESSION NO. AD 4150 098	3. RECIPIENT'S CATALOG NUMBER
4. TITLE (and Subtitle) RESEARCH IN IMAGE UNDERSTANDING AS APPLIED TO 3-D TOMOGRAPHIC IMAGING WITH NEAR OPTICAL RESOLUTION.		5. TYPE OF REPORT & PERIOD COVERED ANNUAL 7/1/83 ~ 8/31/84
		6. PERFORMING ORG. REPORT NUMBER
7. AUTHOR(s) Prepared by N. H. Farhat		8. CONTRACT OR GRANT NUMBER(s) AFOSR 81-0240
9. PERFORMING ORGANIZATION NAME AND ADDRESS University of Pennsylvania The Moore School of Electrical Engineering 200 South 33rd St., Phila., Pa. 19104		10. PROGRAM ELEMENT, PROJECT, TASK AREA & WORK UNIT NUMBERS 6110AF, 2305, B1
11. CONTROLLING OFFICE NAME AND ADDRESS United States Air Force Air Force Office of Scientific Research / NE Building 410, Bolling A.F.B., D.C., 20332		12. REPORT DATE November 30, 1984
14. MONITORING AGENCY NAME & ADDRESS (if different from Controlling Office) As Above		13. NUMBER OF PAGES 123
		15. SECURITY CLASS. (of this report) Unclassified
		15a. DECLASSIFICATION/DOWNGRADING SCHEDULE
16. DISTRIBUTION STATEMENT (of this Report) Approved for release: distribution unlimited The United States Government is authorized to reproduce and distribute reprints for governmental purposes notwithstanding any copyright notation hereon.		
17. DISTRIBUTION STATEMENT (of the abstract entered in Block 20, if different from Report)		
18. SUPPLEMENTARY NOTES		
19. KEY WORDS (Continue on reverse side if necessary and identify by block number) Radar imaging, coherent and incoherent 3-D imaging, microwave tomography, wave- length diversity, polarization diversity, image reconstruction, filtered back- projection, the Fourier camera, dielectric imaging, measurement methodologies.		
20. ABSTRACT (Continue on reverse side if necessary and identify by block number) Our research in high resolution microwave imaging has to date focused broadly on the study and development of efficient and cost-effective data acquisition and image reconstruction methods for use in λ and polarization diversity 3-D tomographic imaging. The techniques developed, combine angular, spectral, and polarization diversity measurements with a unique target derived reference (TDR) technique to produce images of the scattering centers on complex-shaped bodies with unprecedented resolution and quality, as reported here, that exceed by far		

DD FORM 1473

1 JAN 73

EDITION OF 1 NOV 65 IS OBSOLETE

UNCLASSIFIED

anything reported to this date. Analytical studies of information content, speckle suppression, and resolution show however that image quality can further be enhanced and made to approach and even exceed the resolution of optical systems when the imaging of remote objects specially through the earth's atmosphere is desired.

During the period of this report a new method for interpreting and processing high-frequency electromagnetic scattering data has been studied. The method enables image reconstruction by filtered back-projection instead of the customary Fourier inversion method used earlier in our work. Applied to the imaging of conducting bodies such as the B-52 scale model and to simple inhomogeneous dielectric bodies, the method is capable of producing images with equal quality to those obtained previously by 2-D Fourier inversion. A detailed comparison of the computational requirements of the filtered back-projection and the Fourier inversion methods and the quality of their retrieved images shows that each method has advantages and disadvantages. The back-projection method appears however to lend itself to high speed opto-electronic implementation which may prove to be of practical value over purely digital implementation.

Experimental verification of the concept of the Fourier Camera within the scope of our research in high-speed multi-dimensional signal processing by reduction of dimensionality is also presented. Fourier transforms of several incoherently illuminated simple objects have been obtained and compared to results of numerical simulation. The results are in good agreement. An exciting finding of this aspect of our research is that the Fourier camera analyzes the spatial frequency content of natural scenes in polar format in a manner quite similar to that advanced by Fourier models of the human visual system. This opens a new avenue for research into modeling and emulation of the eye-brain system that can be useful in pattern recognition, artificial intelligence, machine vision, and remote sensing.

Continuation of our earlier work in microwave tomographic imaging of dielectric objects as a potential tool for nondestructive evaluation has resulted in noticeable improvement in the fidelity of images of several simple test targets consisting of hollow plexiglass concentric and nonconcentric cylinders and cylinder/plate structures. Both Fourier inversion and filtered back-projection image reconstruction techniques were used yielding nearly equal results. Several methods for 1-D dielectric profile reconstruction from reflection coefficient data were also studied. These 1-D inversion methods are usually more accurate than simple Fourier inversion and therefore have the potential for providing higher resolution images of inhomogeneous dielectric bodies provided they can be extended to 3-D, as for example may be possible by invoking the filtered back-projection algorithm. This issue will be addressed in our future research. If successful a very powerful means for applying the extensive repertoire of exact 1-D inverse scattering techniques to 3-D object reconstruction will become available.

In yet another aspect of our research, high quality projective and tomographic imaging of incoherently emitting 3-D objects has been experimentally verified for the first time employing cross-spectral power density measurements. For simplicity of implementation, the experiments were conducted with incoherent white-noise-like acoustic emission instead of incoherent electromagnetic radiation. High quality projection images of 3-D distribution of noise-emitting acoustic "point" sources were obtained so far as presented here. The results are of practical value in passive 3-D imaging and surveillance.

Finally during this period a systematic study of the effect of angular aperture size on image quality in λ and polarization diversity imaging was completed. The results clearly point to the advantage of using millimeter wave spectral windows in the data acquisition specially when only limited angular

windows are available. For this reason, and other considerations, plans were completed during the period of this report to extend the operation of our Experimental Microwave Measurement and Imaging Facility to the millimeter wave range of the spectrum and for modifications that will enable conducting bistatic scattering measurements. Bistatic measurements are needed to enrich the accessed p-space with information and to better assess the role of polarization in image formation. Accordingly, a proposal for acquisition of the required instrumentation under the DoD University Research Instrumentation Program was prepared and submitted during this period and was recently approved for funding starting January 85. The new upgraded facility will be immensely valuable in the study of real-time high resolution microwave/millimeter wave tomographic imaging of remote objects.

Real-time true 3-D microwave imaging of distant objects with near optical resolution or better will provide a very valuable tool in several applications of interest to the Air Force. These include: damage assessment for remote aerospace targets, identification and classification of unidentified aerospace objects including space debris, radar cross-section reduction (*diaphonization*), nondestructive evaluation (NDE) of dielectric and composite materials that do not lend themselves to ultrasound inspection such as solid propellant grains, and 3-D analysis and mapping of storm centers.

1	2	3	4
5	6	7	8
9	10	11	12
13	14	15	16
17	18	19	20
21	22	23	24
25	26	27	28
29	30	31	32
33	34	35	36
37	38	39	40
41	42	43	44
45	46	47	48
49	50	51	52
53	54	55	56
57	58	59	60
61	62	63	64
65	66	67	68
69	70	71	72
73	74	75	76
77	78	79	80
81	82	83	84
85	86	87	88
89	90	91	92
93	94	95	96
97	98	99	100

TABLE OF CONTENTS

	<u>Page</u>
1. INTRODUCTION	1
2. CURRENT PROGRESS	3
2.1 Microwave Image Reconstruction by Backprojection	3
2.2 High-Speed Fourier Camera and Fourier Model of Human Vision	17
2.3 Image Enhancement Studies	56
2.4 Dielectric Imaging	60
2.5 Projective and Tomographic Imaging of Incoherent 3-D Objects by Cross-Spectral Power Density Measurement	73
2.6 Influence of the Sizes of the Angular and Spectral Apertures on Retrieved Image Quality	89
2.7 Measurement System and Methodologies	99
3. DISCUSSION AND NEW RESEARCH DIRECTIONS	108
4. LIST OF PUBLICATIONS AND OTHER ACTIVITIES	119
5. REFERENCES	121

RESEARCH IN IMAGE UNDERSTANDING AND METHODOLOGIES AS APPLIED
TO 3-D MICROWAVE TOMOGRAPHIC AND PROJECTIVE IMAGING
WITH NEAR-OPTICAL RESOLUTION

1. INTRODUCTION

During the present period our research program in image understanding and methodologies as applied to 3-D microwave tomographic and projective imaging by wavelength, angular, and polarization diversity has concentrated on several of the research tasks listed and discussed in our comprehensive 1983 research proposal where a three year research program was proposed. The tasks pursued during the current period were:

- i. Analysis and experimental demonstration of the first *filtered back-projection* image reconstruction utilizing realistic microwave scattering data.
- ii. Continued study of the imaging of dielectric bodies with special emphasis on the development of a new theoretical approach suited for 1-D and 3-D dielectric profiles. The results obtained indicate that image reconstruction algorithms based on the Rytov approximation and the back-propagation algorithm that are more exact than those of the inverse scattering formulation based on the Born approximation (no multiple scattering) are possible and will therefore be investigated more actively in future research.
- iii. Continued study of dynamic data acquisition and efficient image reconstruction techniques that are optimally suited for use in high resolution 3-D imaging of moving microwave scatterers. This has yielded improved imagery of our test targets in which details of the engine assemblies on both the B-52 and the space shuttle are visible.

- iv. High quality projective imaging of 3-D incoherent objects consisting of collections of point emitters by cross-spectral power density (spectrally-selective cross-correlation) measurements employing spectral and angular diversity. Considerable improvement of the image quality compared to our initial results in this task were obtained. These projection images pave the way to true 3-D tomographic imaging of incoherent emitters which will be pursued in our future and proposed research.
- v. Further study of our incoherent opto-electronic Fourier transforming method, which is being referred to now as the *Fourier camera*.

This latter study included the experimental verification of the operational principle of the Fourier camera and the discovery of two important characteristics of its operation. One is the finding that the Fourier camera can analyze the spatial frequency and spectral contents of a scene in exactly the same manner advanced by a recent Fourier model of human vision. The second finding pertains to the analytical demonstration that the Fourier camera can measure the cross-spectral density of a scene. The spectral power density appears to be the quantity processed by the eye-retina system.

The above findings make the Fourier camera a unique tool in modeling and imitating human and insect vision, in remote-sensing and airborne surveillance, and in robotic vision. The Fourier camera appears also to be compatible with several existing approaches to automated feature extraction (reduction of dimensionality of the data) and classification. For these reasons, considerable attention will be given in our proposed research to this task.

A more detailed description of the achievements listed briefly above and of the resulting new research directions is given next.

Next a list of publications, thesis, and other activities is given followed by a list of personnel and references.

2. CURRENT PROGRESS

In this section, we give a more detailed description of our recent accomplishments and findings under the tasks briefly outlined above. The implications of these findings and their bearing on future direction of our research are also given.

2.1 Microwave Image Reconstruction by Backprojection

Research in this task shows that a method exists for image reconstruction other than that of Fourier inversion used in our work to date. The method is based on a backprojection algorithm similar to that employed in medical computerized axial tomography. The electromagnetic inverse scattering basis for the technique is briefly described here together with a Fourier optics interpretation of the backprojection algorithm. Examples of images obtained applying the backprojection algorithm to realistic microwave scattering data collected in our anechoic chamber facility are presented and compared with those obtained using Fourier inversion.

Theoretical Basis

It is well known that monostatic or bistatic multiaspect frequency response measurement can be used to access the Fourier transform of a scattering object. The far field measured in the direction of the unit vector

\bar{l}_R due to plane wave illumination in the direction of the unit vector \bar{l}_i of a perfectly conducting scattering body is given by,

$$\psi(\bar{p}, R) = \frac{jke^{-j2kR}}{2\pi R} \Gamma(\bar{p}) \quad (1)$$

where we have assumed monostatic probing ($\bar{l}_R = -\bar{l}_i$) with R being the distance between the transmitter/receiver and the origin in the object and where,

$$\Gamma(\bar{p}) = \int_{\text{obj}} \gamma(\bar{r}) e^{j\bar{p} \cdot \bar{r}} d\bar{r} \quad (2)$$

is obtained from the measured field (1) as,

$$\Gamma(\bar{p}) = - \frac{j2\pi R}{k} e^{j2kR} \psi(\bar{p}, R) \quad (3)$$

\bar{p} and \bar{r} being position vectors in Fourier space and object space respectively, $k = \frac{\omega}{c}$ is the wavenumber and,

$$\bar{p} = k (\bar{l}_R - \bar{l}_i) = p \bar{l}_p \quad (4)$$

with,

$$p = |\bar{p}| = \sqrt{\bar{p} \cdot \bar{p}} = 2k \cos \frac{\alpha}{2} \quad (5)$$

Here α is the angle between \bar{l}_R and \bar{l}_i and the monostatic case is denoted by $\alpha = 0$. The scattering function $\gamma(\bar{r})$ represents the 3-D distribution and strengths of scattering centers on the object. It is given by the 3-D Fourier inversion of $\Gamma(\bar{p})$,

$$\gamma(\bar{r}) = \frac{1}{(2\pi)^3} \int \Gamma(\bar{p}) e^{-j\bar{p} \cdot \bar{r}} d\bar{p} \quad (6)$$

Equations (2) to (5) indicate that the 3-D Fourier space of the scattering object, i.e., the Fourier transform of the scattering function, can be measured by changing k for various fixed values of \bar{l}_p over a finite region of \bar{p} -space (Fourier space) along radial lines emanating from the origin of a p_x, p_y, p_z coordinate system. The exact shape and size of the accessed Fourier volume depends on the values assumed by the vector \bar{p} i.e., on the spectral window utilized and on the range of aspect angles of the object for which the scattered field is measured. Equations (3) and (6) provided the basis for the Fourier inversion image reconstruction employed in our work to date.

To simplify the following analysis of the *backprojection algorithm* for image reconstruction we assume without loss of generality of the results, that $\gamma(\bar{r})$ consists of a collection of point scatterers of amplitudes a_i located at \bar{r}_i which can be represented by an array of three dimensional delta functions of weights a_i , that is,

$$\gamma(\bar{r}) = \sum_i a_i \delta(\bar{r} - \bar{r}_i) \quad (7)$$

where δ is the Dirac delta function. Combining eqs. (2) and (7) yields,

$$\Gamma(\bar{p}) = \sum_i a_i e^{j\bar{p} \cdot \bar{r}_i} \quad (8)$$

Now for any fixed direction \bar{l}_p , eq. (1) can be written as merely a function of ω ,

$$\psi(\omega) = \frac{j\omega e^{-j2\frac{\omega}{c}R}}{2\pi R c} \Gamma\left(2\frac{\omega}{c} \bar{l}_R\right) \quad \omega_1 < \omega < \omega_2 \quad (9)$$

The inverse Fourier transform of $\psi(\omega)/\omega$ represents the temporal impulse response of the object as measured from the aspect or direction \bar{l}_R . This will be,

$$g(t) \triangleq F \left\{ \frac{\psi(\omega)}{\omega} \right\} = \frac{j}{(2\pi)^2 R c} \int_{-\infty}^{\infty} H(\omega) e^{-j\frac{\omega}{c} R} \Gamma\left(2\frac{\omega}{c} \bar{l}_R\right) e^{j\omega t} d\omega \quad (10)$$

where F designates the Fourier transform and,

$$H(\omega) = \begin{cases} 1 & \dots \omega_1 < \omega < \omega_2 \\ 0 & \dots \text{elsewhere} \end{cases} \quad (11)$$

represents the rectangular spectral window utilized in the measurement extending from ω_1 to ω_2 . Making use of eqs. (8) in (10) and making use of eq. (4) and (5) we obtain,

$$\begin{aligned} g(t) &= \frac{j}{2\pi R c} \int_{-\infty}^{\infty} H(\omega) \sum_i a_i e^{j2\frac{\omega}{c} \bar{l}_R \cdot \bar{r}_i} e^{-j2\frac{\omega}{c} R} e^{j\omega t} d\omega \\ &= \frac{j}{2\pi R c} h(t) * \sum_i a_i \delta\left[t - \frac{2R}{c} + \frac{2}{c} (\bar{r}_i \cdot \bar{l}_R)\right] \end{aligned} \quad (12)$$

or,

$$g(t) = \frac{j}{(2\pi)^2 R c} \sum_i a_i h\left[t - \frac{2R}{c} + \frac{2}{c} (\bar{r}_i \cdot \bar{l}_R)\right] \quad (13)$$

where $h(t)$ is the inverse Fourier transform of $H(\omega)$. The advantage of using wide spectral windows that make $h(t)$ approach a delta function is now obvious.

In that case the temporal impulse response of the object as measured from a given direction \bar{l}_R will be composed of a train of narrow time delayed impulses occurring at,

$$t_i = \frac{2}{c} (R - \bar{r}_i \cdot \bar{l}_R) \quad (14)$$

The scattering from all centers for which

$$\bar{r}_i \cdot \bar{l}_R = \text{const} \quad (15)$$

are seen to occur at the same time. Equation (15) is that of a plane normal to \bar{l}_R . Therefore all scattering centers lying in a plane normal to \bar{l}_R will contribute to the same delayed $h(t)$ in eq. 13. The impulse response $g(t)$ represents therefore the projection of the scattering strengths of all those scattering centers of the object that lie in planes normal to \bar{l}_R on a line in the \bar{l}_R direction. In other words $g(t)$ measures the projection of the 3-D scattering function $\gamma(\bar{r})$ of the object on a line parallel to \bar{l}_R which we call the *projection line*. By repeating the measurement $g(t)$ for a sufficiently large number of different directions \bar{l}_R (different object aspects), enough such 3-D to 1-D projections can be obtained to allow reconstructing $\gamma(\bar{r})$ by backprojection. The required backprojection algorithm would consist of:

(a) Alignment of the various $g(t)$ s in time to eliminate any unequal propagation time delay $2R/c$ as could occur when an array of transmitter/receiver stations is employed in interrogating the object from different aspects and the range R between each station and a prescribed origin on the object are not equal. One way of making this alignment is the TDR method described extensively in our earlier publications (see 3 and 4 of list of publications)

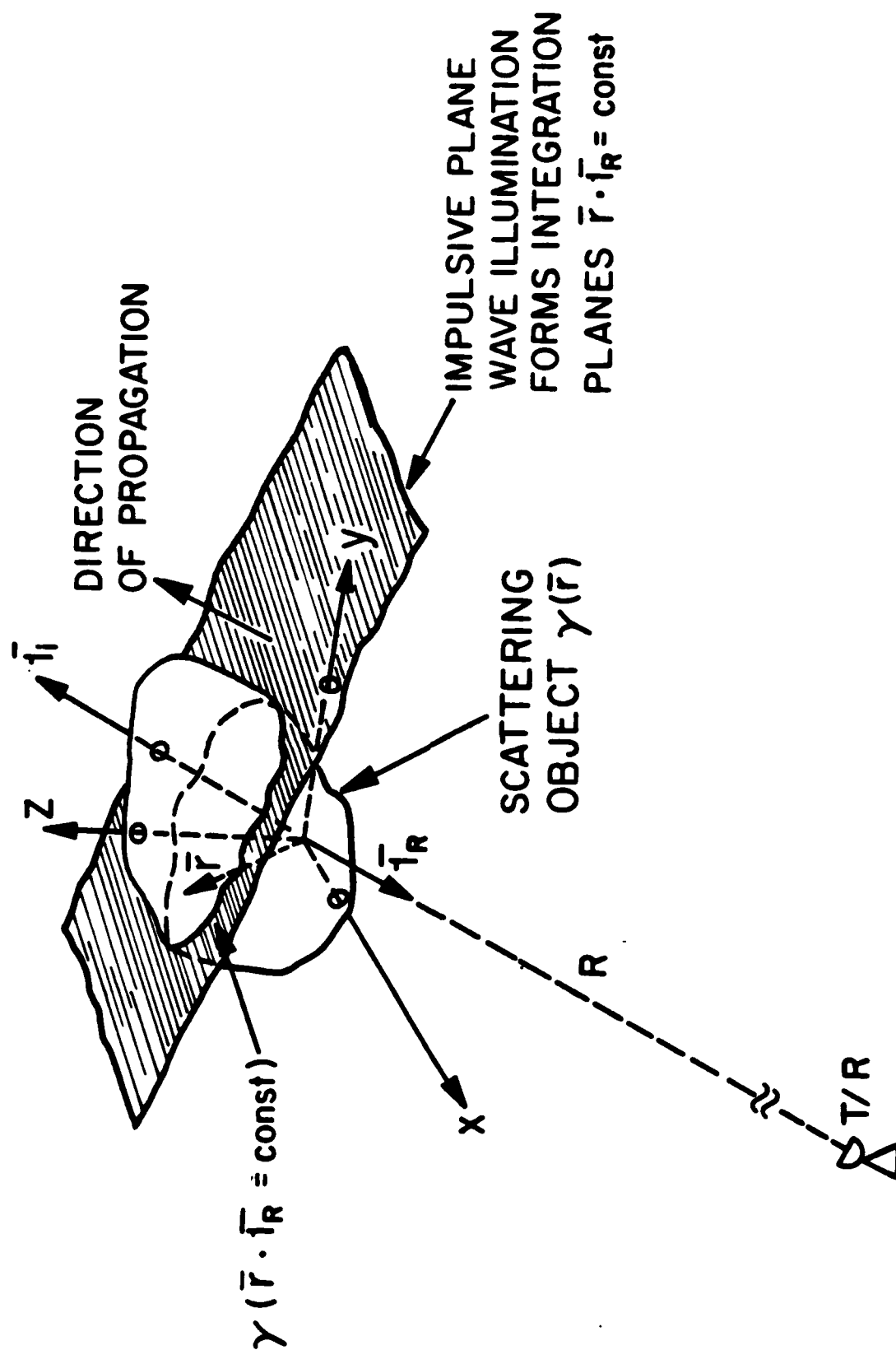


Fig. 1. Illustrating 3-D to 1-D projection in inverse scattering.

Another is based on cross-correlating the impulse responses $g(t)$ belonging to angularly adjacent observation (looks). Since for adjacent aspect angles the $g(t)$ s will be caused predominantly by the same scattering centers they will be highly correlated. The time displacement between adjacent $g(t)$'s required to achieve maximum correlation will represent then the relative shift in the location of the scattering centroid of the object. The shifts between successive angularly adjacent looks is then used to sequentially correct the time delays of the $g(t)$ s to obtain the required alignment. Once this time alignment or equivalent range "tweeking" is achieved one proceeds to the next step of the algorithm.

(b) The second step of the backprojection algorithm consist of orienting the range corrected functions $g(t)$ in 3-D space along the directions of their \bar{l}_R vectors and backprojecting or "smearing" the values of each $g(t)$ in space into planes normal to the lines of projection and adding the results in 3-D space to reconstruct an image of $\gamma(\bar{r})$.

Our work to date has focused on accessing a single slice in the Fourier space of the scattering object by changing the object orientation in azimuth only. A projection image of the scattering centers of the object is then retrieved by Fourier inversion of the polar formatted slice data or "slice hologram". Clearly each radial line in the polar formatted \bar{p} -space slice represents the frequency response of the object measured from a different aspect angle. Fourier inversion of the data in a given radial line yields, as discussed earlier a "temporal response" or "finite-width-impulse response" which represents essentially the projection of the scattering centers of the 3-D object on a line in the \bar{l}_p direction. In other words, multiaspect fre-

quency response measurements of an object represent indirectly the projection of the scattering centers of the 3-D object on lines of different orientations determined by the directions of viewing. This suggests as pointed out earlier that image reconstruction should be implementable using some sort of back-projection algorithm. Indeed the working of such an algorithm can be appreciated by examining the coherent optical Fourier transform arrangement of Fig. 1(a) utilized in optical image retrieval. The reconstructed image resulting from the optical Fourier transform of the fan-shaped pattern $\Gamma(p, \phi)$ of the projection or slice hologram in Fig. 2(a) can be viewed as being produced by coherent superposition of the Fourier transforms of the individual radial (constant ϕ) lines in the hologram. An example of the Fourier transform of two such lines is shown in Fig. 2(b) where the Fourier transform of each line is seen to be smeared uniformly in the Fourier plane or image plane in a direction normal to each line. Super position of these two smeared complex field patterns in the image plane provides the contribution of the data in the two radial hologram lines to the image. This Fourier optics interpretation of the optical image retrieval process should also be implementable digitally by Fourier inversion of the individual frequency responses in the projection hologram (or slice hologram) for each ϕ to obtain a collection of corresponding temporal responses. By proper temporal and angular alignment of these temporal responses as described earlier and by smearing or back-projecting each in a direction normal to its angular orientation and adding the values of the backprojection at every point we expect to reconstruct the image of the object. One aim of our backprojection reconstruction effort is to analyze and study backprojection algorithms digitally to see whether

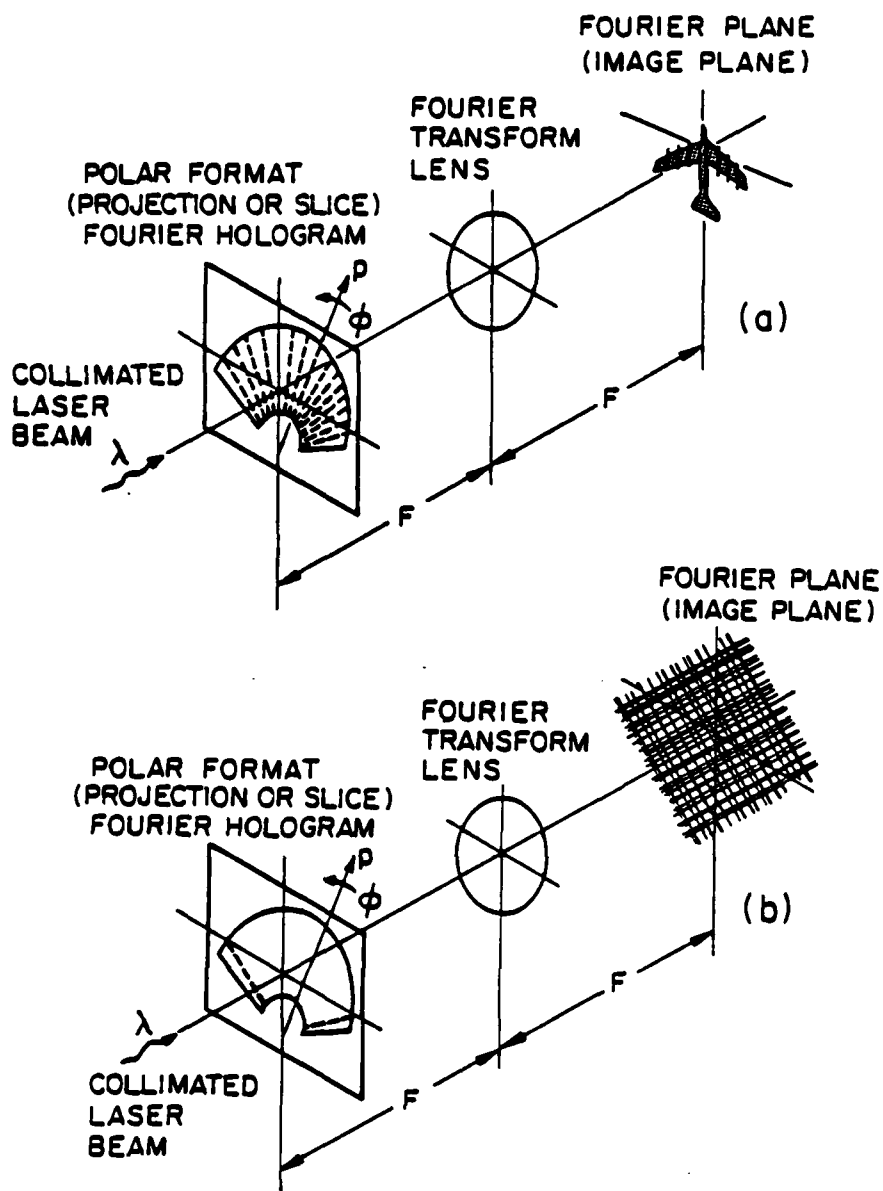


Fig. 2. Fourier optics interpretation of the back-projection algorithm.
 (a) Optical Fourier transform of \bar{p} -space projection or slice hologram. (b) Contribution of two \bar{p} -space lines to retrieved image.

they offer any advantages over the digital 2-D interpolation/Fourier inversion method used in obtaining the images given in our earlier work. For example an apparent advantage of the back-projection algorithm over the FFT algorithm is that it does not require data transformation by four nearest neighbors interpolation from polar to rectangular format as needed when applying the 2-D digital Fourier transform. Data interpolation may therefore appear not to be necessary. Unfortunately this is not so since interpolation of each backprojection on a rectangular image format is necessary in image reconstruction. A clear advantage however is that the range normalization and "phase tweaking" algorithm described in earlier work (see 3 and 4 of list of publications) are directly applicable to the temporal response data for synthesis of a TDR. It is also an aim of this aspect of our study to apply a variety of filtering operations, that have been successfully utilized in tomographic x-ray reconstruction by back-projection, to the temporal response data before backprojecting and reconstructing the image and to assess their influence on image quality.

Experimental Results

Results of an image retrieved by digital implementation of the backprojection algorithm described above are presented in Fig. 3. The data utilized is that of the B-52 scale model test object collected as described elsewhere (see 3 and 4 of list of publications) and employed there to retrieve the images by means of four nearest neighbors interpolation from polar to rectangular format followed by Fourier inversion. Figure 3(a) shows a sequence of 4 photographs illustrating how the image emerges gradually in the backprojection process as data from an increasing number of 3-D to 1-D projections are added. In Fig. 3(b),

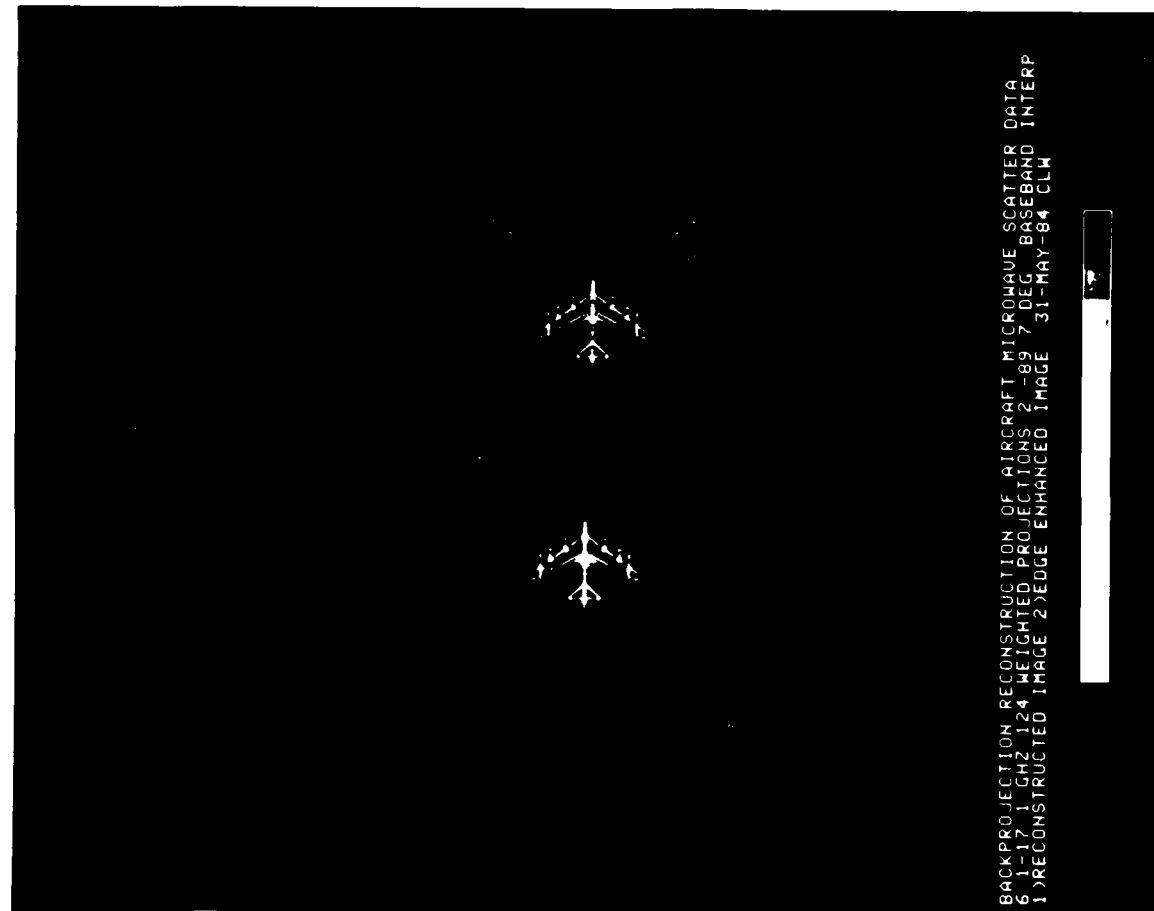
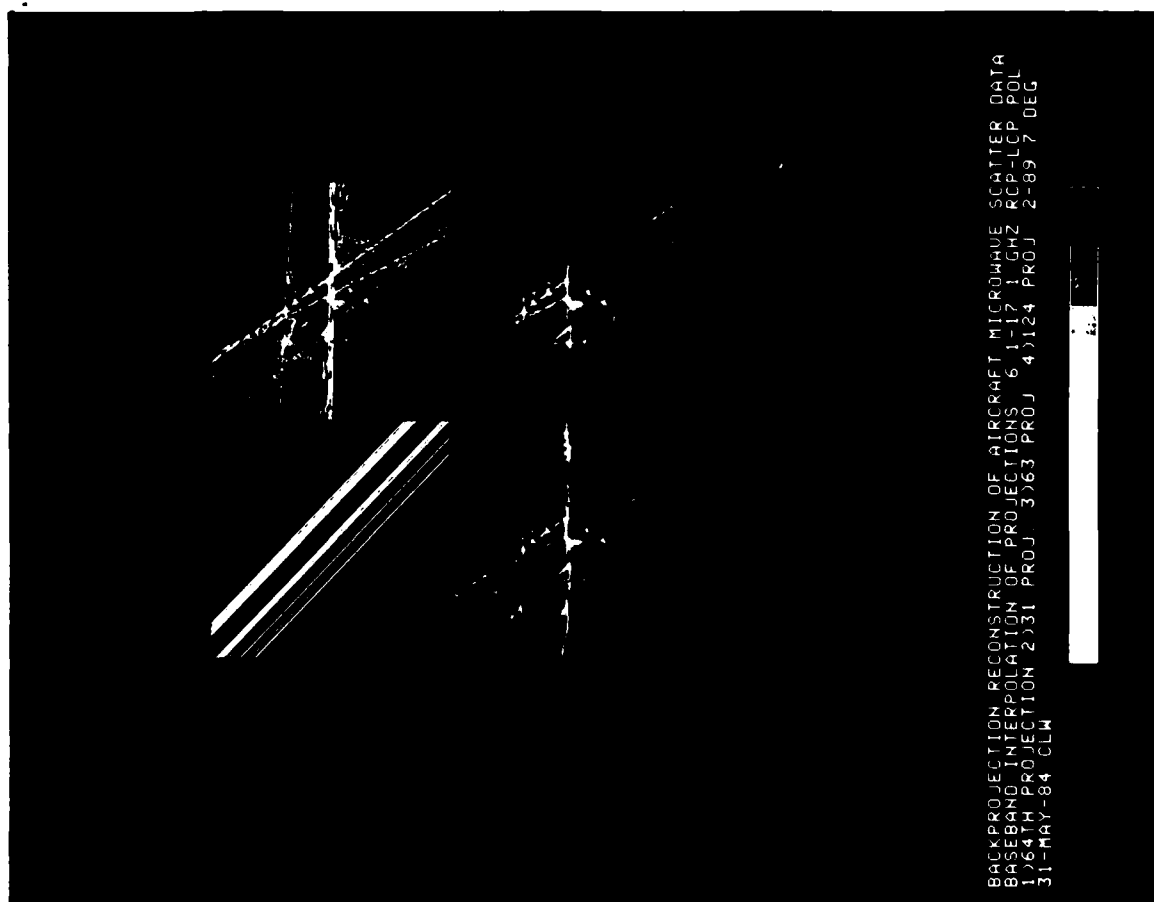


Fig. 3. Results of backprojection reconstruction employing baseband interpolation. Test object: scale model of B-52. Spectral window: (6-17) GHz in 128 frequency steps, angular aperture: 90° extending from head on to broadside in 128 looks. (a) Top left - image retrieved by back-projection of the impulse response of the 64-th look, top right: from 31 looks, bottom left: 63 looks, bottom right: 124 looks. (b) Polarization and symmetry enhanced backprojection image (left) and its edge enhanced version (right).

the polarization and symmetry enhanced version of the image in the lower right quadrant of Fig. 3(a) is shown (left) together with its edge enhanced version (right). In obtaining the result in Fig. 3(a) each line in the \bar{p} -space data utilized was individually multiplied by a ramp function or passed through an R&L filter [1] before Fourier inversion to obtain the corresponding temporal impulse response or 3-D to 1-D projection of the object. Because of the positive range of the spectral window utilized ($f_1 < f < f_2$), $f_1 = 6$ GHz, $f_2 = 17$ GHz, the impulse responses are complex and contain a high frequency carrier of frequency proportional to $(f_1 + f_2)/2$. The presence of this carrier would ordinarily make backprojection followed by interpolation on the rectangular image grid prone to error as indeed was evident in our earliest backprojection reconstructions. A base band interpolation method was therefore devised to handle the carrier in the backprojection algorithm such as to minimize errors and obtain the images shown in Fig. 3(b). When compared to images of the B-52 obtained by direct Fourier inversion, the backprojection images presented here are seen to be nearly identical. The images shown in Fig. 3(b) represent the first backprojection reconstruction of a microwave object from realistic data. Growing interest in the back projection algorithm is becoming evident in the literature [2],[3] for some of the reasons indicated earlier. Work on this aspect of our research program is continuing. We find that the backprojection formulation of image reconstruction in inverse scattering can be useful for the understanding and interpretation of the near field inverse scattering problem when the object is illuminated by a spherical wave instead of a planar wave and the receiver (monostatic with the transmitter) is not located in the far field of the object but in its near field instead. Some reflection on this situation in light of the backprojection algorithm described above shows that all scattering centers lying on a spherical surface through the object will contribute to the same detail in the *spherical impulse response*

of this situation as depicted in the 2-D sketch of Fig. 4(a). In the bistatic case, i.e., when the transmitter and the receiver are not located at the same point, all scattering centers lying on an ellipsoidal surface running through the object with the transmitter and the receiver as its focal points will contribute to the same echo in the *ellipsoidal impulse response* encountered in this case as depicted in Fig. 4(b). Near field inverse scattering is important in two aspects of our work. One is in the formulation of a generalized theory of holography, and synthetic aperture radar (SAR) where the object is normally illuminated by a spherical wavefront and the monostatic receiver is in the near field of the illuminated ground swath. Another area of research which will benefit from this near field formulation is our dielectric imaging task for non-destructive evaluation and noninvasive imaging. One must keep in mind however that for inhomogeneous dielectric bodies the constant delay surfaces will depart from spherical or ellipsoidal and that such departures must be determined and taken into account in some kind of an iterative backprojection algorithm. Future research in this task will therefore include numerical and experimental study of the near field inverse scattering formulation based on indirect impulse measurement (i.e., Fourier inversion of the corrected frequency response) and back projection of the resulting echos along spherical or ellipsoidal surfaces.

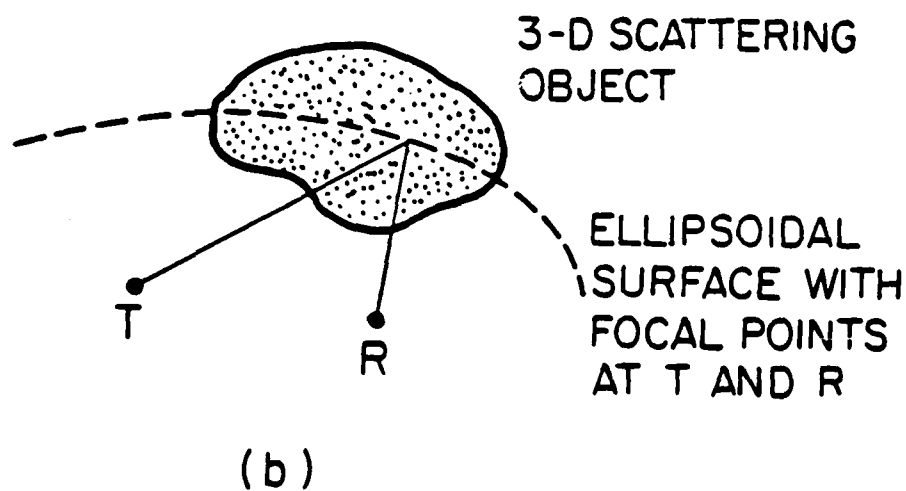
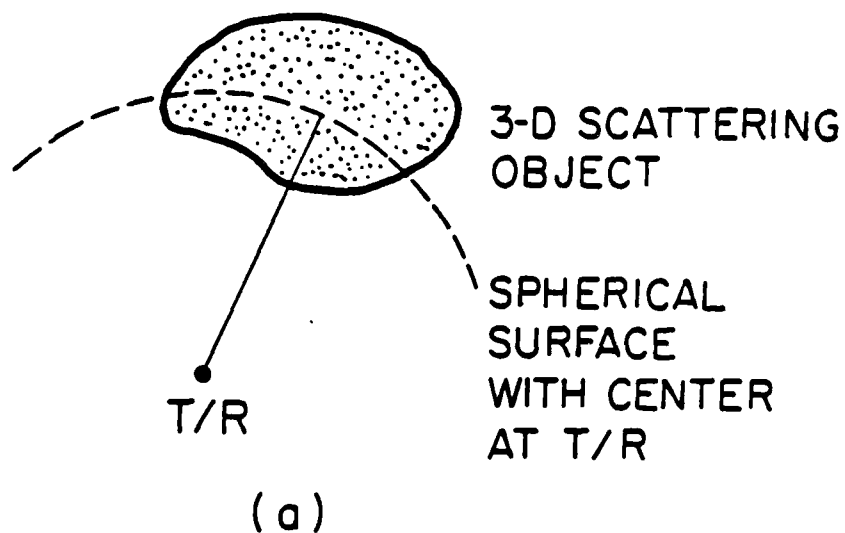


Fig. 4. Geometries for the interpretation of near-field inverse scattering. (a) monostatic case, (b) bistatic case. (T = transmitter, R = receiver)

2.2 High-Speed Fourier Camera and Fourier Model of Human Vision

In earlier work [4] we described an incoherent opto-electronic Fourier transformation scheme based on reduction of dimensionality through application of the projection slice theorem associated with the multi-dimensional Fourier transform. The motivation for the scheme was the devising of an ultra high-speed 2-D Fourier transformation scheme that can be utilized in true 3-D tomographic image reconstruction from λ and polarization diversity, imaging radar data. The scheme offers high sensitivity and speed, wide dynamic-range (because of a novel method for eliminating the dynamic-bias problem that plagues most incoherent opto-electronic processing schemes), and an ability to perform Fourier transformation of real scenes (hence the name *Fourier Camera*) or of 2-D complex functions through color coding. In addition the scheme lends itself readily to trade-off between the degrees of serial and parallel processing that may be employed as a means of tailoring throughput and cost to the requirements of specific applications.

During the current research period performance evaluation of an optical bench implementation of the Fourier camera was undertaken. The results of this evaluation are presented next.

Performance Evaluation

Based on the theory of operation and device implementation discussed in the previous work [4], experiments were set up and carried out using optical gear, electronic instrumentation, and a MINC 11/2 minicomputer at the Electro-Optics and Microwave-Optics Laboratory. Several simple test object scenes with well known Fourier transforms were chosen and used to study and evaluate system performance. The results obtained with these test object scenes were compared with the results of numerical simulations carried out on the MINC 11/2.

The analysis of our opto-electronic scheme has been carried out for four test object scenes, namely, uniform illumination, pinhole, and homogeneous (uniformly illuminated) circular aperture and rectangular aperture. Details of the analysis and experimental results are presented below. The case of uniform illumination is shown also to provide a simple and effective means for aligning the positive and negative portion of mask frequencies with corresponding detector photosites.

(i) Uniform Illumination

If we ignore the effect of diffraction by the entrance pupil of the processor, the Fourier transform of this object scene will be a Dirac Delta function that is invariant with the rotational angle α of the object scene. The object function in this case is given by

$$f(x,y) = \text{constant} \quad (16)$$

where for simplicity we take the constant to be unity representing the

uniform brightness or radiance of the plane. Then the projection on the x axis is,

$$f_p(x) = I \text{ for all } x \quad (17)$$

where I is the constant intensity depending on the irradiance in the uniform illumination. For simplicity we take $I=1$.

This function is smeared in the y-direction then spatially modulated in the x direction by the sine/cosine mask, and integrated in the x-direction as described in [4]. The integrated output of the cosine mask is,

$$F_c(\omega_r) = \int f_p(x) [1 + \cos(\omega_r x)_+] dx - \int f_p(x) [1 + \cos(\omega_r x)_-] dx \quad (18)$$

where ω_r is used instead of ω_x in equation (18) in anticipation of the axial symmetry of the result,

and

$$-\omega_{rm} \leq \omega_r \leq \omega_{rm}$$

and in our case $\omega_{rm} = 32$ user's unit in the present system. In equation (18) $\cos(\omega_r x)_+$ and $\cos(\omega_r x)_-$ denote respectively the transmittance of the positive and negative cosine portions of the sine/cosine mask used to implement optoelectronically a bipolar mask transmittance in incoherent light [4].

Expression (18) can be simplified to

$$\int f_p(x) \cos(\omega_r x) dx \quad (19)$$

Note equations (18) and (19) illustrate mathematically the operation of our novel opto-electronic bipolar mask scheme. Using a similar

derivation, the integrated output of the sine mask can be shown to be,

$$F_s(\omega_r) = \int f_p(x) \sin(\omega_r x) dx \quad (20)$$

Thus the resultant 1-D Fourier transform for all rotation angles is given by,

$$\begin{aligned} F(\omega_r) &= F_c(\omega_r) + j F_s(\omega_r) \\ &= \int f_p(x) \cos(\omega_r x) dx + j \int f_p(x) \sin(\omega_r x) dx \\ &= \int e^{j\omega_r x} dx = 2\pi \delta(\omega_r) \end{aligned} \quad (21)$$

for, $0^\circ \leq \alpha < 180^\circ$ and $-\omega_{rm} \leq \omega_r \leq \omega_{rm}$

which is a Dirac Delta "function" in the 2-D Fourier transform plane.

Strictly speaking since the width of the sine/cosine mask is finite the above result should be modified as follows: For example, for a mask of width W , we have

$$\begin{aligned} &\int_{-\frac{W}{2}}^{\frac{W}{2}} f_p(x) e^{j\omega_r x} dx \\ &= \int_{-\frac{W}{2}}^{\frac{W}{2}} e^{j\omega_r x} dx = W \text{sinc}\left(\omega_r \frac{W}{2}\right) \end{aligned} \quad (22)$$

$$0^\circ \leq \alpha < 180^\circ \quad \text{and} \quad -\omega_{rm} \leq \omega_r \leq \omega_{rm}$$

which in view of the independence on α is a radial sinc function in the 2-D Fourier transform plane.

The case of uniform illumination is important from a practical view point as will be seen below for registering the detector photosites with the outputs of the various frequencies of the sine/cosine mask. It is straight-forward to show that the intensity of light emerging from the positive and negative segments of any frequency line of the mask is constant. Thus when perfect alignment is established, the output of the detector array will be zero for all frequencies except for $\omega_x = 0$. Recall that the outputs of each two adjacent photosites receiving the outputs of the positive and negative cycles of any given mask frequency are subtracted.

(ii) Pinhole Illumination (Dirac Delta Function);

The object function $f(x,y)$ in this case is given by the Delta "function",

$$f(x,y) = \delta(x,y) \quad (23)$$

Then the spatially projected image $f_p(x)$, which is also invariant to the rotational angle α of the object scene is given as:

$$f_p(x) = \delta(x) \quad (24)$$

Thus the resultant 1-D Fourier transform, which is the same for all rotation angles, is given by

$$\begin{aligned} F(\omega_r) &= F_c(\omega_r) + j F_s(\omega_r) \\ &= \int f_p(x) \cos(\omega_r x) dx + j \int f_p(x) \sin(\omega_r x) dx \\ &= \int \delta(x) e^{j\omega_r x} dx = 1 \end{aligned} \quad (25)$$

$$0^\circ \leq \alpha < 180^\circ \quad \text{and} \quad -\omega_{rm} \leq \omega_r \leq \omega_{rm}$$

which is the constant output we expect for the Fourier transform of a pinhole approximating a Dirac Delta "function".

(iii) Homogeneous Circular Aperture (Disc)

As in the preceding case the circular symmetry of this object function implies that its spatial projection does not change with object rotation

a. The object function in this case is given by

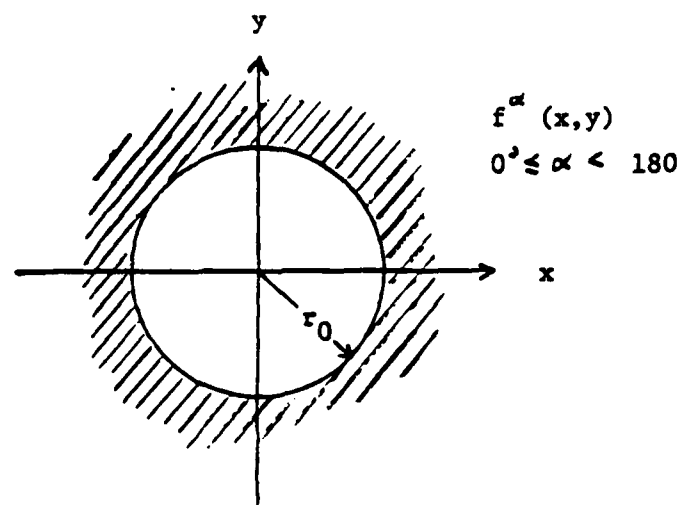
$$f(x,y) = \begin{cases} x^2 + y^2 \leq r_o^2 & ; \\ 0 & , \text{ elsewhere} \end{cases} \quad (26)$$

The radius r_o of the aperture, was chosen such that the extent of the image impinging on the sine/cosine mask is equal to or smaller than the width of the sine/cosine mask. In practice, this can be realized by adjusting the magnification of the objective lens of the system. Note the size of the projected image will not change the nature of the transform only its scale. Referring to Fig. 5, the projected image of the object scene is given by

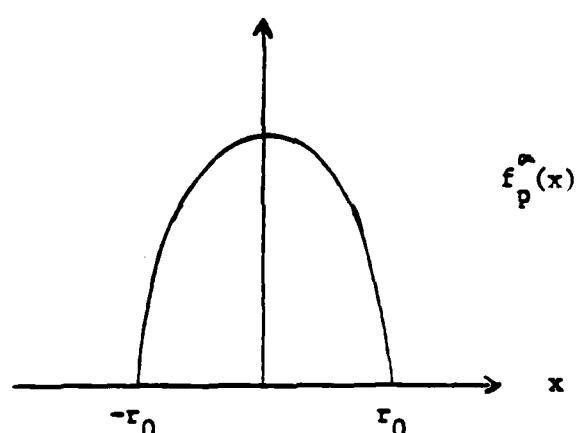
$$f_p(x) = 2 (r_o^2 - x^2)^{1/2} \quad -r_o \leq x \leq r_o \quad (27)$$

Following the steps of equations (18) to (20) we obtain,

$$\begin{aligned} F(\omega_r) &= \int f_p(x) e^{j\omega_r x} dx \\ &= \int_{-r_o}^{r_o} 2(r_o^2 - x^2)^{1/2} e^{j\omega_r x} dx \\ &= 2 \int_{-\infty}^{\infty} \text{rect}\left(\frac{x}{2r_o}\right) (r_o^2 - x^2)^{1/2} e^{j\omega_r x} dx \\ &= 4r_o \text{sinc}(r_o \omega_r) * \int_{-\infty}^{\infty} (r_o^2 - x^2)^{1/2} e^{j\omega_r x} dx \end{aligned} \quad (28)$$



(a)



(b)

Fig. 5. Homogeneous circular aperture and its x-axis projection. Because of circular symmetry projection is independent of α .

The integral part of (28) can be simplified as follows:

$$\begin{aligned}
 \text{Int} &= \int_{-\infty}^{\infty} (r_o^2 - x^2)^{\frac{1}{2}} e^{j\omega_r x} dx \\
 &= r_o^2 \int_{-\infty}^{\infty} [1 - (\frac{x}{r_o})^2]^{\frac{1}{2}} e^{j\omega_r r_o (\frac{x}{r_o})} d(\frac{x}{r_o}) \\
 &= r_o^2 \int_{-\infty}^{\infty} (1 - \xi^2)^{\frac{1}{2}} e^{jr_o \omega_r \xi} d\xi
 \end{aligned} \tag{29}$$

By making the following substitutions:

$$\begin{aligned}
 \xi &\rightarrow \omega \\
 r_o \omega_r &\rightarrow \tau
 \end{aligned} \tag{30}$$

Expression (29) yields [5],

$$\text{Int} = 2\pi r_o^2 \frac{J_1(r_o \omega_r)}{2 r_o \omega_r} = \pi r_o^2 \frac{J_1(r_o \omega_r)}{r_o \omega_r} \tag{31}$$

The resultant circularly symmetric Fourier transform (for all the rotational angles) can therefore be expressed by,

$$F(\omega_r) = 4\pi r_o^3 \text{sinc}(r_o \omega_r) * \frac{J_1(r_o \omega_r)}{\omega_r} \tag{32}$$

$$0^\circ \leq \alpha < 180^\circ \quad \text{and} \quad -\omega_{rm} \leq \omega_r \leq \omega_{rm}$$

which is the expected result: a Bessel function radial dependence modulated by the sinc function envelope caused by the limited extent of the circular aperture object scene.

(iv) Homogeneous Rectangular Aperture (Square)

To simplify the task of analyzing the rectangular aperture, we only examine the closed form expression for the output of the processor for specific rotational angles α . The characteristic detail of the resultant 2-D Fourier transform along the direction α is obtained both numerically and experimentally. The analysis for all rotational angles is obtained by using a computer simulation which will be discussed later. The homogeneous square object function of side A (see Fig. 6) is given now by,

$$f(x,y) = \text{rect} \left(\frac{x}{A}, \frac{y}{A} \right) \quad (33)$$

The size of this rectangular aperture is chosen such that the maximum extent of its projected image is equal to or smaller than the width W of sine/cosine mask (i.e. $\sqrt{2A} < W$).

For the rotational angles of 0° or 90° , the projection of the object scene is given by (see Fig. 6),

$$f_p(x) = A \text{rect} \left(\frac{x}{A} \right) \quad \alpha = 0^\circ \text{ or } 90^\circ \quad (34)$$

Following the same steps of equations (18) to (20), we arrive at:

$$\begin{aligned} F(\omega_r) &= \int_{-A/2}^{A/2} f_p(x) e^{j\omega_r x} dx \\ &= \int_{-A/2}^{A/2} A e^{j\omega_r x} dx = A^2 \text{sinc} \left(\omega_r \frac{A}{2} \right) \end{aligned} \quad (35)$$

where $\alpha = 0^\circ$ or 90° , and $-\omega_{rm} \leq \omega_r \leq \omega_{rm}$.

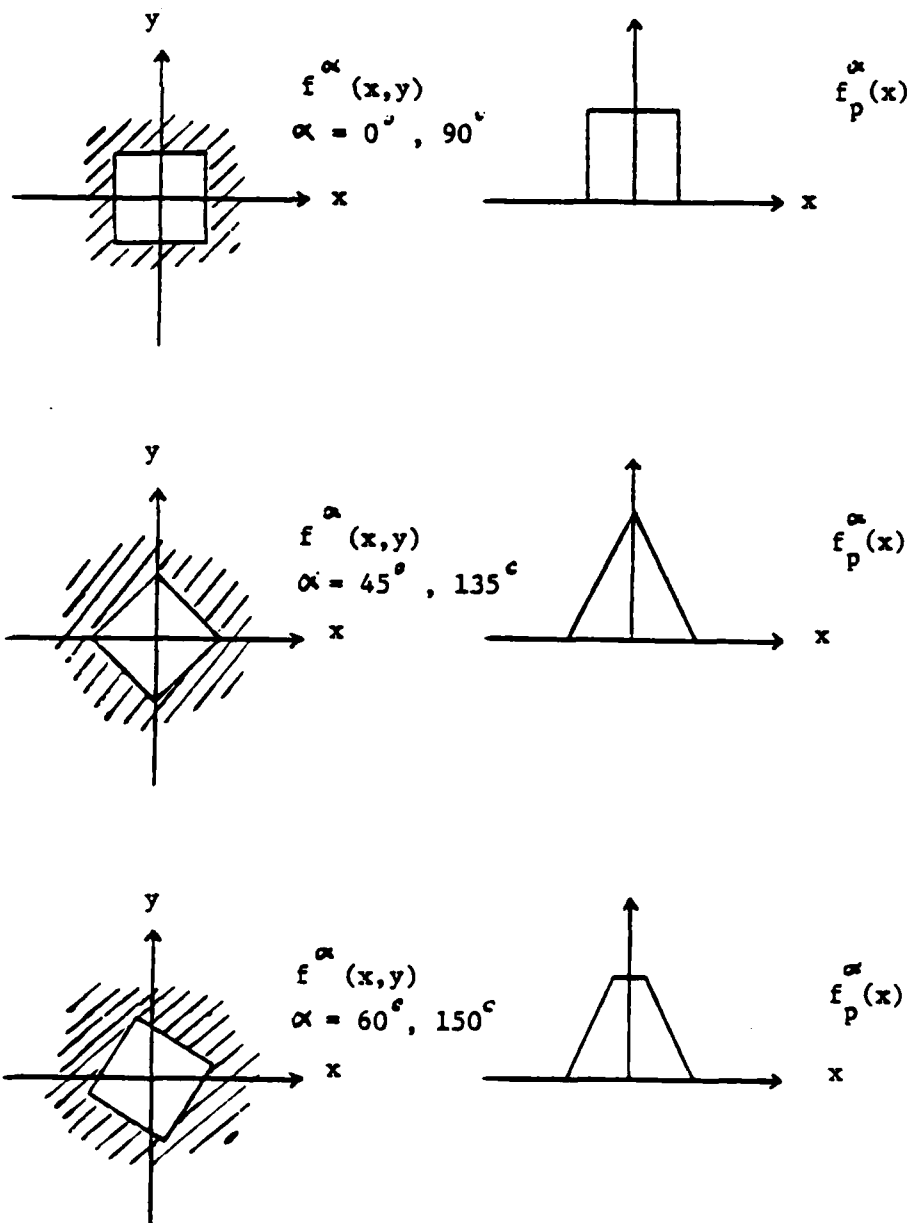


Fig. 6. Homogeneous rectangular (square) aperture at various rotation angles α (left) and corresponding x-axis projections (right).

For the rotational angles of 45° or 135° , the projection is (see Fig. 5),

$$f_p(x) = \sqrt{2}A \left[1 - \frac{|x|}{A/\sqrt{2}} \right] \quad |x| < \frac{A}{\sqrt{2}} \quad \alpha = 45^\circ \text{ or } 135^\circ \quad (36)$$

and

$$\begin{aligned} F(\omega_r) &= \int f_p(x) e^{j\omega_r x} dx \\ &= \int \left[\sqrt{2} \operatorname{rect} \left(\frac{x}{A/\sqrt{2}} \right) * \sqrt{2} \operatorname{rect} \left(\frac{x}{A/\sqrt{2}} \right) \right] e^{j\omega_r x} dx \\ &= \left[\int \sqrt{2} \operatorname{rect} \left(\frac{x}{A/\sqrt{2}} \right) e^{j\omega_r x} dx \right]^2 \\ &= A^2 \operatorname{sinc}^2 \left(\frac{\omega_r A}{2\sqrt{2}} \right) \end{aligned} \quad (37)$$

where $\alpha = 45^\circ$ or 135° and $-\omega_{rm} \leq \omega_r \leq \omega_{rm}$. For the rotational angles of 60° or 150° , the projection is (see Fig. 5),

$$f_p(x) = \begin{cases} \frac{2A}{\sqrt{3}} & |x| \leq \left(\frac{\sqrt{3}-1}{4} \right) A ; \\ \left(1 + \frac{1}{\sqrt{3}} \right) A \left[1 - \frac{|x|}{\left(\frac{\sqrt{3}+1}{4} \right)} \right] , & \left(\frac{\sqrt{3}-1}{4} \right) A \leq |x| \leq \left(\frac{\sqrt{3}+1}{4} \right) A ; \\ 0 & , \quad \text{elsewhere} \end{cases} \quad (38)$$

and

$$\begin{aligned} F(\omega_r) &= \int f_p(x) e^{j\omega_r x} dx \\ &= \frac{4}{\sqrt{3}} \int \left[\operatorname{rect} \left(\frac{x}{A/2} \right) * \operatorname{rect} \left(\frac{x}{\sqrt{3}A/2} \right) \right] e^{j\omega_r x} dx \\ &= \frac{4}{\sqrt{3}} \left[\int \operatorname{rect} \left(\frac{x}{A/2} \right) e^{j\omega_r x} dx \right] \left[\int \operatorname{rect} \left(\frac{x}{\sqrt{3}A/2} \right) e^{j\omega_r x} dx \right] \\ &= A^2 \operatorname{sinc} \left(\frac{\omega_r A}{4} \right) \operatorname{sinc} \left(\frac{\sqrt{3}\omega_r A}{4} \right) \end{aligned} \quad (39)$$

where $\alpha = 60^\circ$ or 150° and $-\omega_{rm} < \omega_r < \omega_{rm}$. The results above show that the significant sidelobes of the 2-D Fourier transform of a rectangular aperture are distributed as expected along the ω_x and ω_y axis of the Fourier transform plane.

(v) Bar Stripe Object

The task of analyzing this bar stripe object or rectangular grating aperture can be simplified by examining the closed form expression for the output of the processor for only specific rotational angles. The object function for this case (see Fig. 7) is given now by,

$$f(x,y) = \sum_{n=-M}^M \text{rect} \left(\frac{x-nc}{B} \right) \frac{y}{A} \quad (40)$$

where A is the length of each bar of the grating pattern, and $B = A/3$, $c = 6.5 \times A/32$, $M = 2$ in our case.

The size of the bar stripe or grating pattern was also chosen such that the maximum extent of its projected image is smaller than or equal to the width W of sine/cosine mask. For a rotational angle $\alpha = 0^\circ$, the spatially projected image of the object scene is given by (see Fig. 7).

$$f_p(x) = A \sum_{n=-M}^M \text{rect} \left(\frac{x-nc}{B} \right) \quad (41)$$

Therefore,

$$\begin{aligned} F(\omega_r) &= \int f_p(x) e^{j\omega_r x} dx, \quad \omega_r = \omega_y \\ &= A \sum_{n=-M}^M \int \text{rect} \left(\frac{x-nc}{B} \right) e^{j\omega_r x} dx \\ &= A \sum_{n=-M}^M e^{j\omega_r nc} \int_{-B/2}^{B/2} e^{j\omega_r x} dx = AB \text{sinc} \left(\frac{\omega_r B}{2} \right) \sum_{n=-M}^M e^{j\omega_r nc} \end{aligned} \quad (42)$$

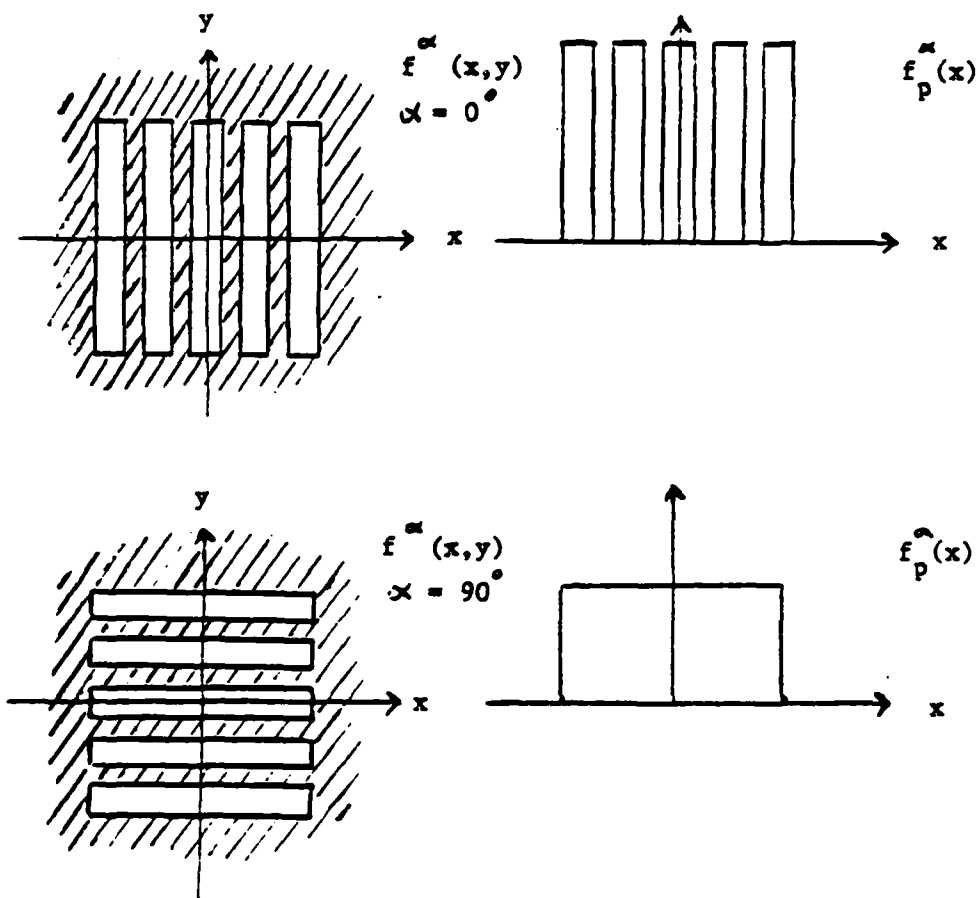


Fig. 7. Bar stripe object (left) and its x-axis projections for two rotational angles α (right).

$$= AB \text{sinc}\left(\frac{\omega_r B}{2}\right) \left[1 + 2 \sum_{m=1}^M \cos(\omega_r mc)\right], \quad \omega_r = \omega_y \quad (43)$$

For the rotational angle $\alpha = 90^\circ$, the projection is (see Fig. 7),

$$f_p(x) = (2M+1)B \text{ rect}\left(\frac{x}{A}\right) \quad (44)$$

and

$$\begin{aligned} F(\omega_r) &= \int f_p(x) e^{j\omega_r x} dx \\ &= (2M+1) AB \text{sinc}\left(\frac{\omega_r A}{2}\right), \quad \omega_r = \omega_x \end{aligned} \quad (45)$$

Equations (43) and (45) show that the significant sidelobes of the 2-D Fourier transform of a rectangular grating are distributed as expected along the ω_x and ω_y axis of the Fourier transform plane. Note that the constant scaling factor of (45) is $(2M+1)$ times larger than that of (43). In other words, (45) dominates the characteristics of the resultant Fourier transform.

Results of the above analysis provide us with a simple means for verifying and evaluating the performance of the Fourier transform processor for each of the test objects. For the first two test objects (uniform illumination and pinhole), the closed form expressions obtained serve as comparison for the experimental results obtained for these objects. The experimental result for the uniform illumination and pinhole are shown in Fig. 8 and Fig. 9 respectively. In these and in all other photographs

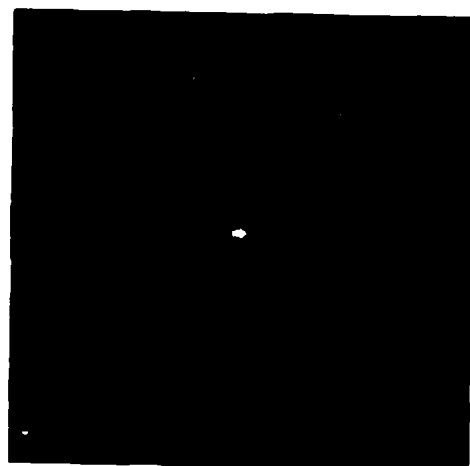


Fig. 8. Output of Fourier transform processor for a uniform object scene (Uniform input illumination) showing the expected Dirac Delta function.

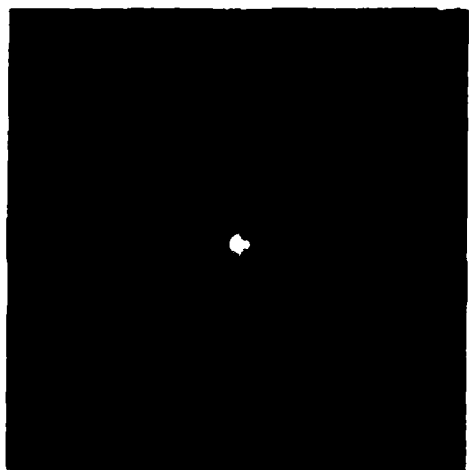


Fig. 9. Same output as in Fig. 24 but showing the effect of detector array misalignment.

of the output patterns presented, a linear weighting (ramp function) in the radial direction was applied to avoid overexposure of the central portion of the photographed patterns because of increased brightness due to the convergence of the radial display format towards the origin. As we know, the output Fourier transform of a uniform illuminated object as obtained in the analysis above is a Dirac Delta function. Figure 8 shows that the experimental output of the processor is consistent with the analytical result. Since the uniform illumination provides us with a practical means to register the detector photosites with the various frequencies of the sine/cosine, it is instructive to examine the effects of a misregistration of the detector array with outputs of the sine/cosine mask on the output of our processor. An illustration of the effect of misregistration, obtained by shifting the detector array vertically, is given in Fig. 9. The resulting asymmetrically broadened pattern is caused by the misregistration of the detector photosites with the various frequencies of the sine/cosine and by a shift of the rotational center of radially formatted displayed data.

For the pinhole object scene, the analysis shows that the output Fourier transform of the processor is constant. Figure 10 illustrates an experimentally obtained F.T. of the pinhole. The result is seen to be consistent with the analysis.

To facilitate the evaluation of the experimental results for the remaining test objects, plots and photographs of the processor output were obtained in a numerical simulation using the analytical expressions derived above. For the circular aperture object scene given in Fig. 11(a) both the simulated

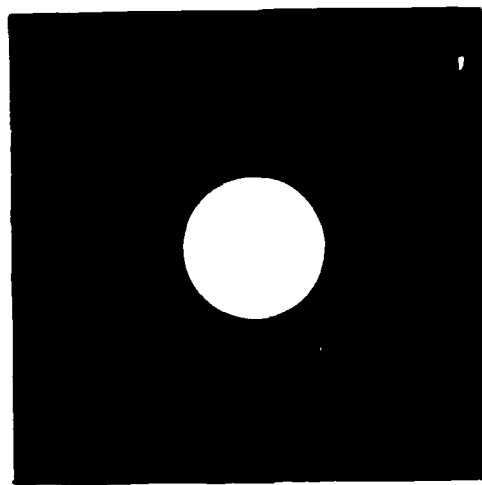


Fig. 10. Uniform output of Fourier transform processor
for pinhole illumination representing an
incoherent point source.

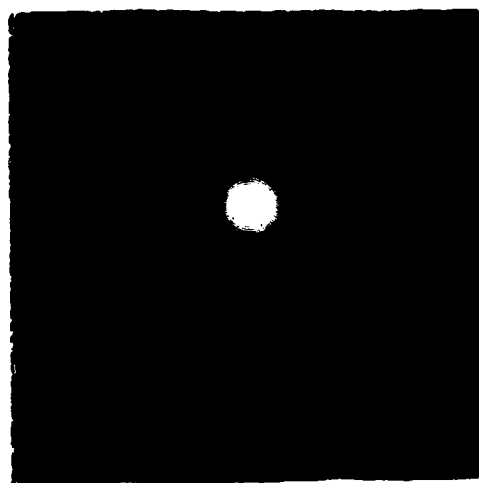
and experimental results were photographed and presented in Fig. 11(b) and Fig. 12(a) respectively for comparison. Radial amplitude plots at a given angular cut ($\alpha = \text{constant}$) are also given in Fig. 11(c) and 12(b) to show the output Fourier transform in detail. In Figs. 11 and 12 the central lobe and first ring of Bessel function are observed for the simulated result as well as the experimental result. Note that the number of rings (sidelobes) appearing depends on the dimension of object scene, the frequency extent of the sine/cosine mask, and on the system configuration. The discrepancy between the theoretical and experimental radial distribution of the output is shown in Fig. 12(b) where a 15% maximum error is observed. Possible sources of such an error are:

- (a) Imperfect alignment of the experimental set-up,
- (b) Defects in the fabrication of sine/cosine mask.

For the square rectangular aperture object scene shown in Fig. 13(a) the results of both the simulation and experiment are presented in Fig. 13(b) and Fig. 15. In addition, several radial distributions (angular cuts) for different values of α are shown in Fig. 14 (simulated results) and in Fig. 16 (experimental results). From Figs. 13, 14, 15, and 16, we find that first sidelobes of the theoretical 2-D sinc function are observed along the u_x and u_y directions for both the simulated and experimental results. The number of sidelobes observed is a function of the dimension of object scene, the frequency extent of the sine/cosine mask, and the system configuration.



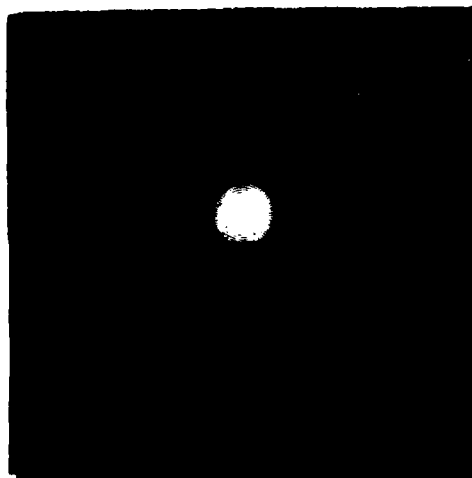
(a)



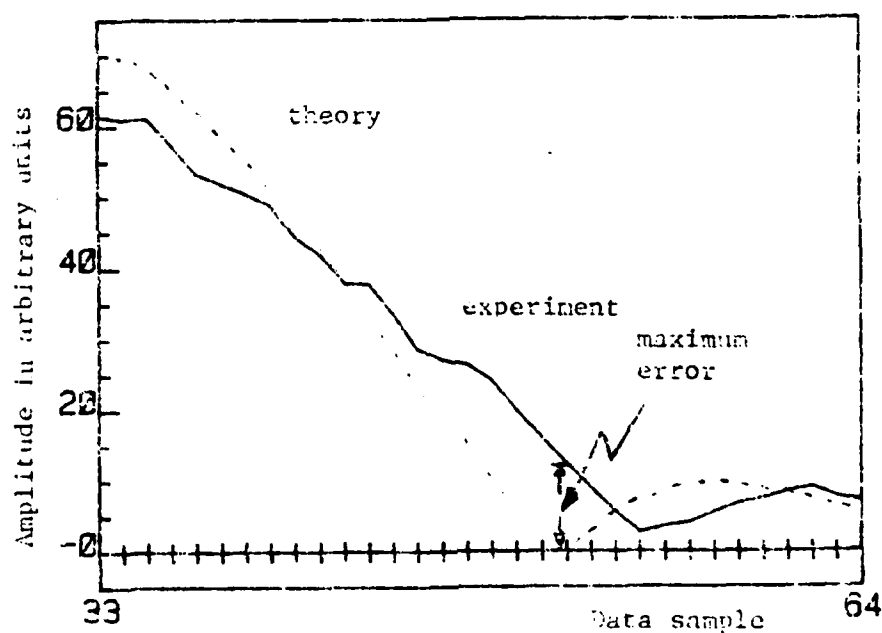
(b)

Fig. 11. Simulation Results:

- (a) Object scene: circular aperture (bright disc on black background).
- (b) Output Fourier transform: Bessel function.



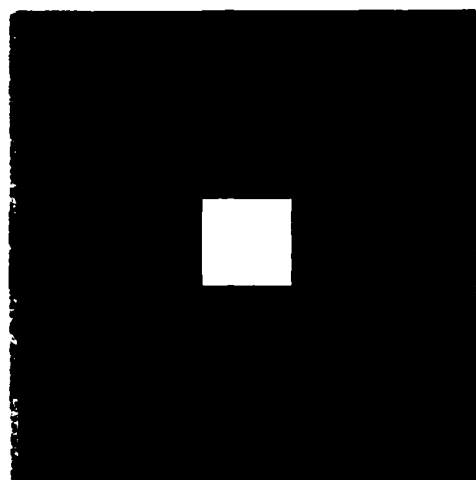
(a)



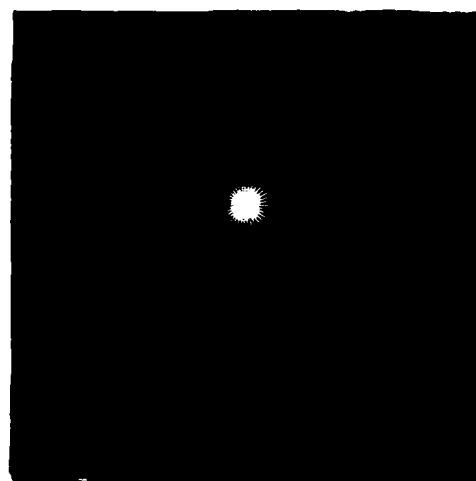
(b)

Fig. 12. Experimental results: Output of Fourier transform processor for the circular aperture object of Fig. 11(a).

- (a) Output showing central lobe and first ring of Bessel function.
- (b) Plot of the radial distribution of the output shown compared with the theoretical result of Fig. 11(b). The maximum error is 15%.



(a)



(b)

Fig. 13. Simulation results: (a) Object scene-Square rectangular aperture. (b) Output Fourier transform showing central region of two dimensional sinc function.

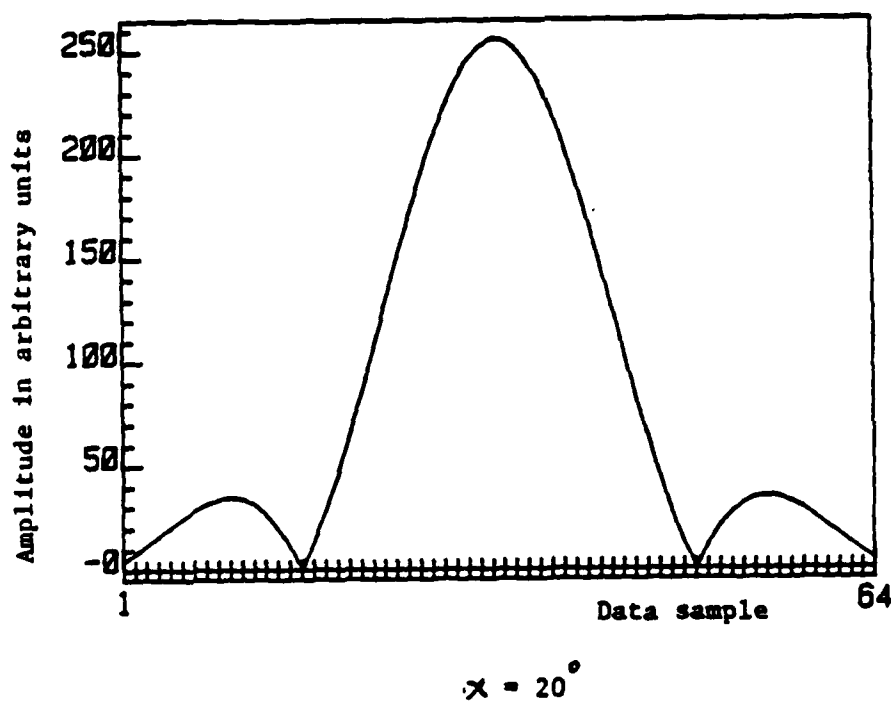
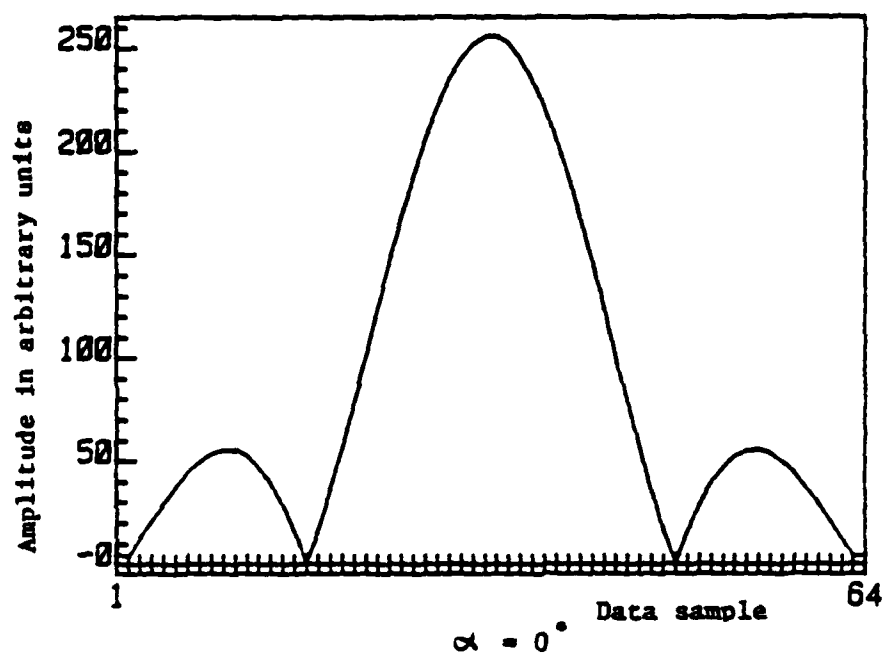


Fig. 14. Simulation results of square rectangular aperture: Radial plots of Fourier transform along $\alpha = 0^\circ$ and 20° .

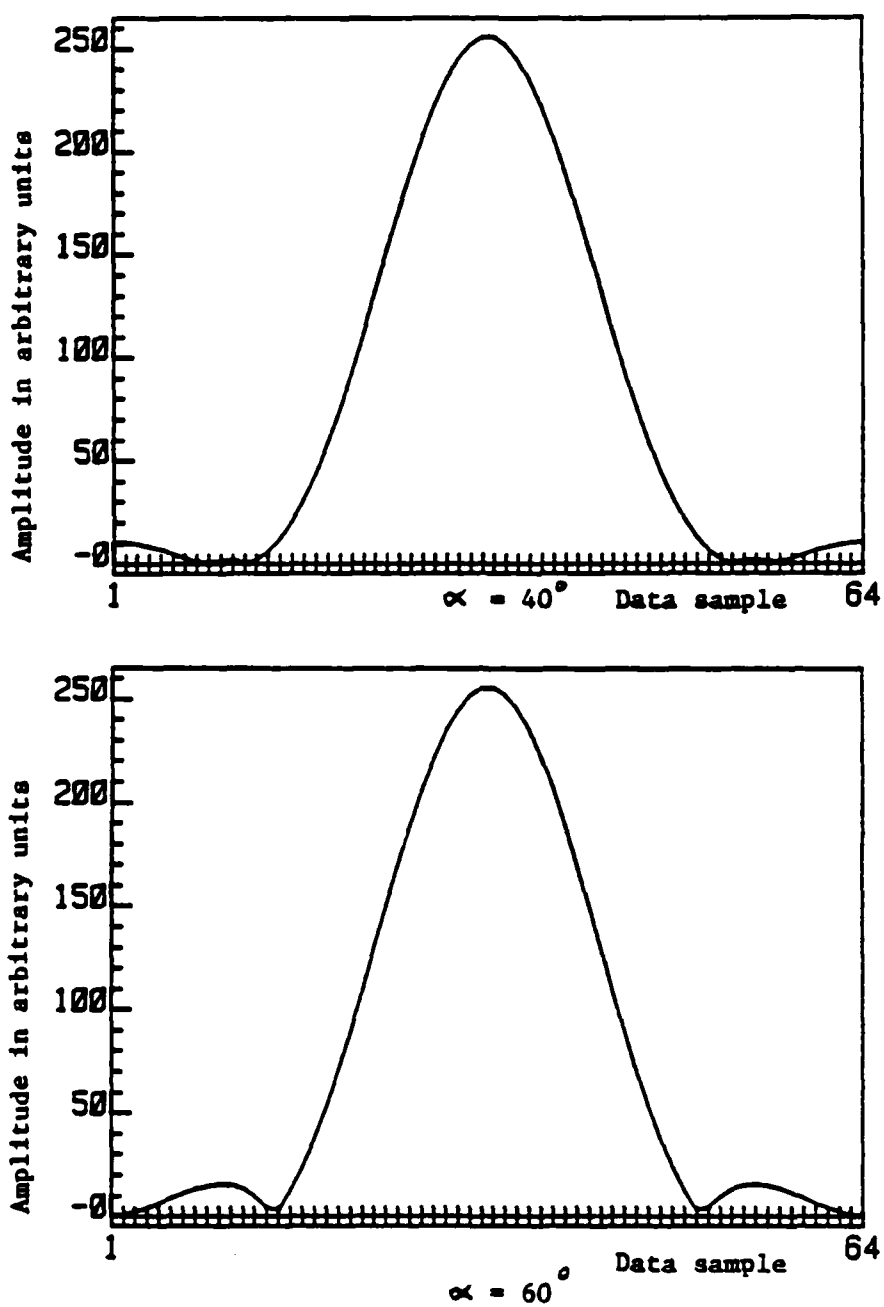


Fig. 14. (Contd.) Simulation results of square rectangular aperture: Radial plots of Fourier transform along $\alpha = 40^\circ$ and 60° .

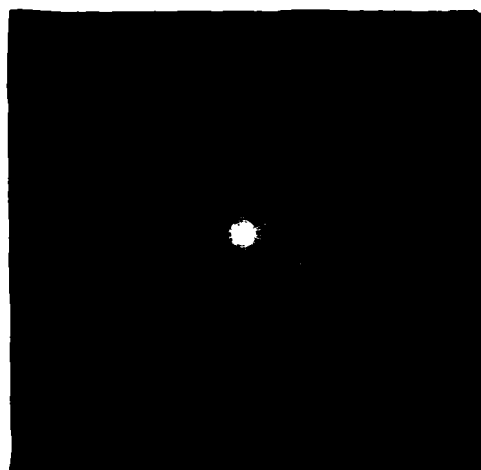


Fig. 15. Experimental result for square rectangular aperture showing central region of the Fourier transform.

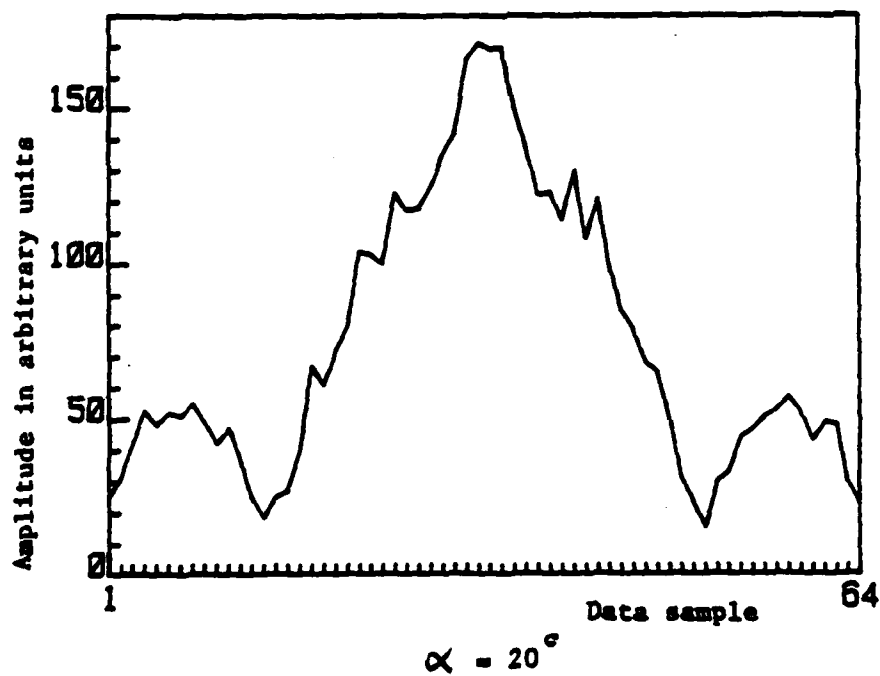
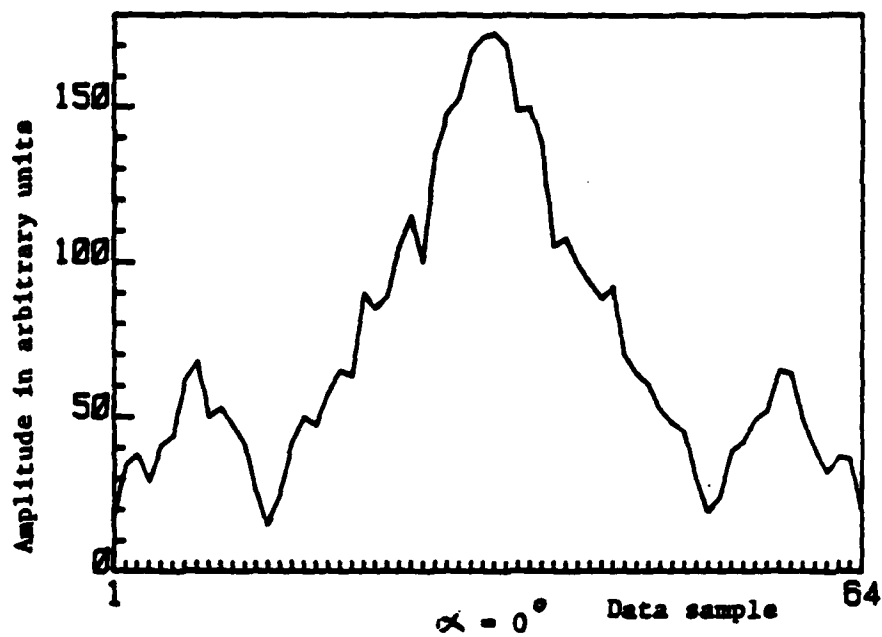


Fig. 16. Experimental results for square rectangular aperture showing radial plots of the output F.T. along $\alpha = 0^\circ$ and 90° .

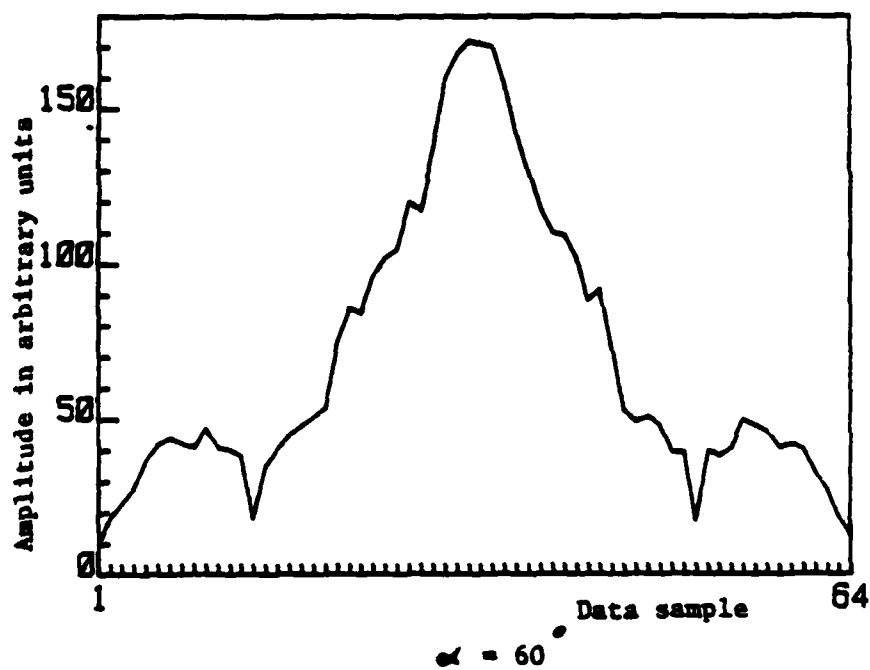
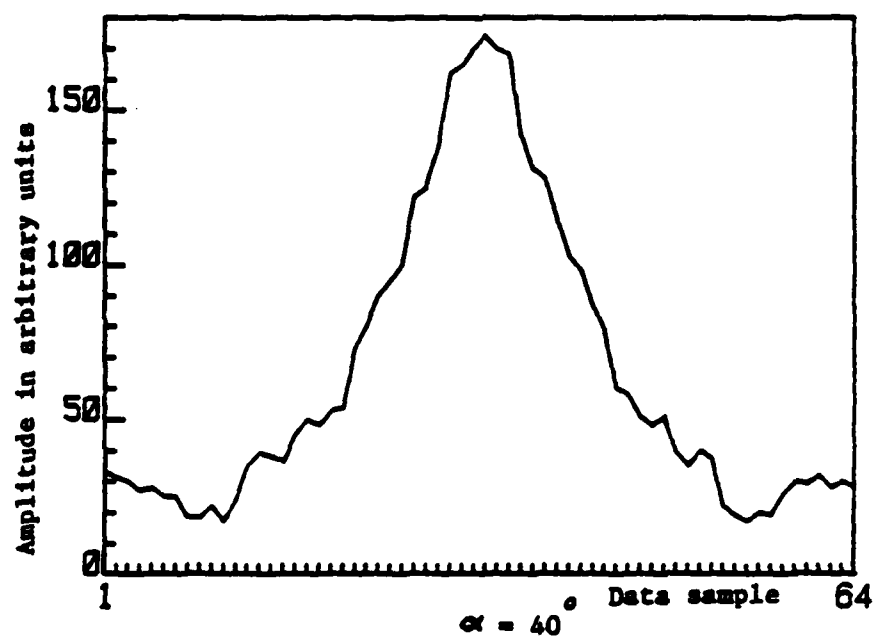
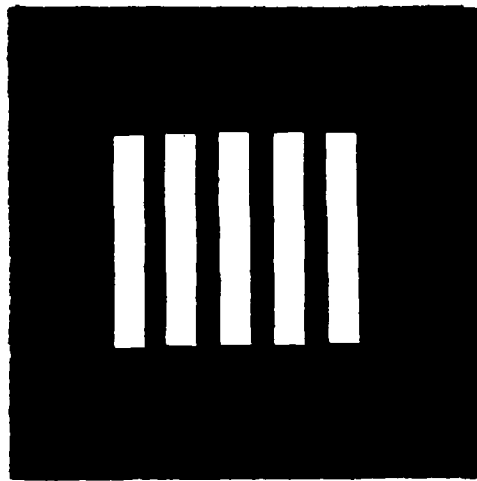


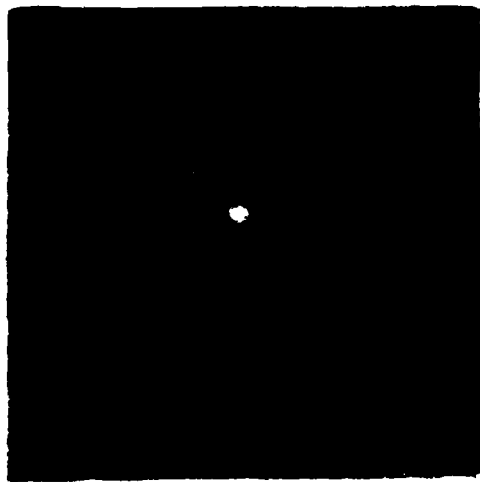
Fig. 16. (Contd.) Experimental result for square rectangular aperture showing radial plots output F.T. along $\alpha = 40^\circ$ and 60° .

A bar stripe object (see Fig. 17(a)) was also introduced in our experiment. A photograph of the output Fourier transform is presented in Fig. 17(b). Two amplitude plots of angular cuts of the output Fourier transform are given in Fig. 18. In this result the first sidelobes of the sinc function are observed along the ω_x direction. The result is in agreement with equations (43) and (45).

The quality of the sine/cosine mask, the dynamic range of the optical sensor array, and the accuracy of A/D converter control dynamic range of our opto-electronic scheme. Such a dynamic range of the opto-electronic scheme will limit the contrast of the output Fourier transform of the processor. Even with these limitations, the experimental results shown in this chapter demonstrate the capability of Fourier transformation of our novel incoherent opto-electronic system.



(a)



(b)

Fig. 17. Experimental results for a bar stripe object rectangular grating.

(a) Test object.

(b) Output F.T. showing central lobe and first side-lobe of expected sinc function.

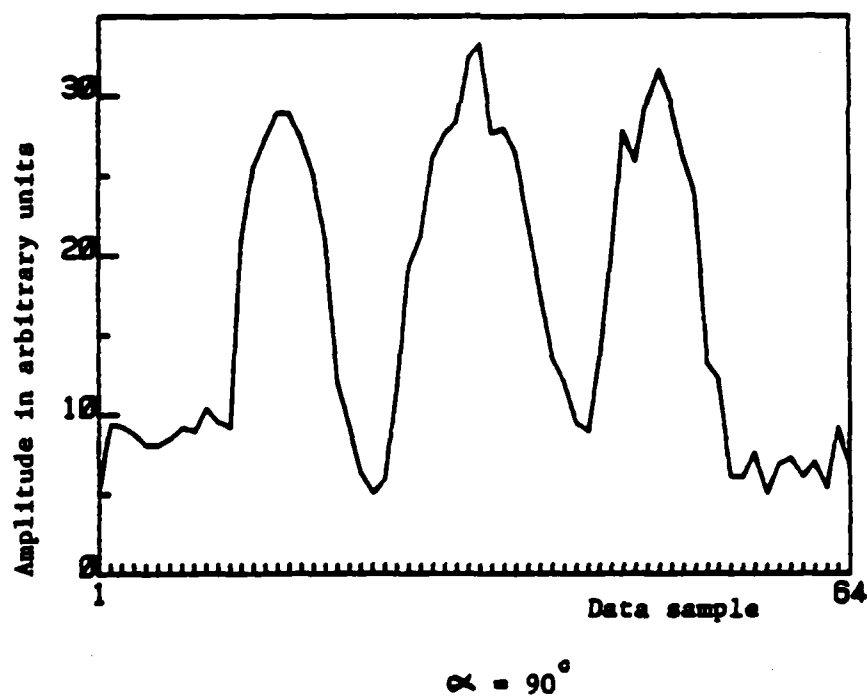
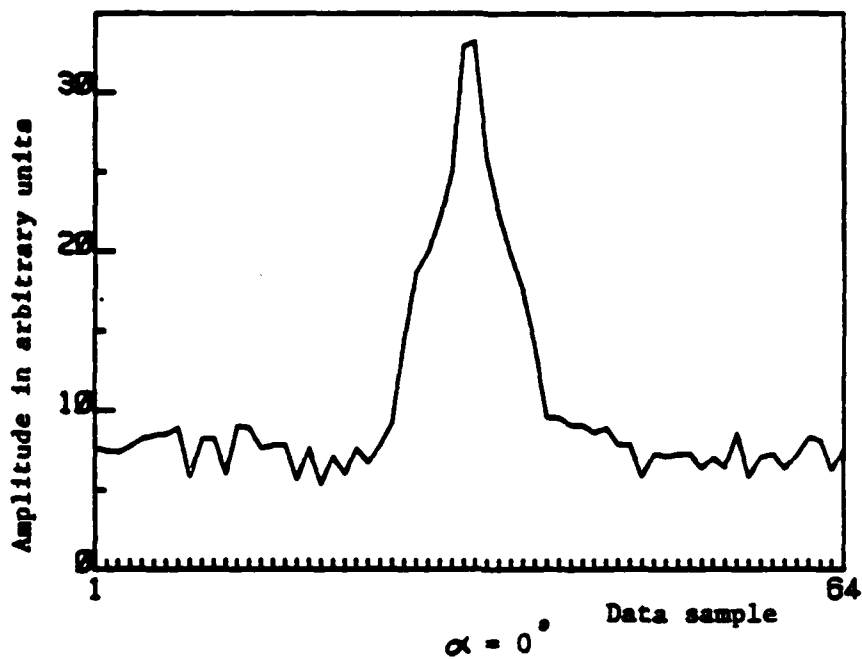


Fig. 18. Experimental result for rectangular grating showing plots of angular cuts of output F.T. along $\alpha = 0^\circ$ and 90° .

The above preliminary results show good agreement between theory and experiment. Better accuracy can be expected with a better design of the image rotator. Excellent contrast in the output is obtained because of the wide dynamic-range achieved by dynamic bias and d.c. bias suppression. Dynamic range of the order of 60 dB equivalent to an accuracy of about 20 bits should be attainable. This could be obtained by using a very fine precisely fabricated sine/cosine mask using state of the art microphotographic technique and by using a high dynamic range commercially available optical sensor array in the output detection portion of the system. Linear radial weighting of the output was applied in our work to compensate for the inherent excessive central brightness of the radial polar format and produce a more subjectively pleasing CRT display of the output of the processor. The image rotation required in the scheme involves a dove prism rotated by a stepper motor through a 1:1 belt drive that allows $90^\circ/0.9^\circ = 100$ steps to cover the required 180° rotation of the projected image needed to produce one Fourier transform from covering 360° in the output made-up of 2-sided radial lines. This means that the angular spacing between lines is $180^\circ/100 = 1.8^\circ$. When this spacing is too coarse for certain applications, a 2:1 gear drive could be then used to produce 0.9° angular spacing in the output (i.e., 200 radial lines) and give a higher resolution display of the spectral power density of the input function than that realized with the current system if desired. As mentioned earlier this opto-electronic Fourier camera has the potential for high data throughput. An estimate of the time required to obtain a Fourier transform of a given stationary input function presented to the processor can be determined as follows: The time required to complete, for example, 200 rotational steps

with a fast stepper motor capable of 20,000 steps/sec is $200/2 \times 10^4 = 10^{-2}$ sec = 10 msec. The speed with which the output of the processor can be read-out in each step is determined by the bandwidth and the number of elements of the self-scanned detector array used. For the RL256G detector array used in this work the bandwidth is 1 MHz, the time needed to read out the 256 elements would be about $256/10^6 = 2.56 \times 10^{-4}$ sec. The time needed to read the detector array 200 times is 5.12×10^{-2} sec. Note that two detector arrays with 256 elements each read-out in parallel would be used to realize a complex F.T. of 1.28×10^4 pixels (64 frequency points x 200 radial lines). The complete F.T. would be completed in $10^{-2} + 5.12 \times 10^{-2} = 6.12 \times 10^{-2}$ sec. The throughput of the system defined as the number of complex Fourier transform points per second is therefore $1.28 \times 10^4 / 6.12 \times 10^{-2} = 2 \times 10^5 / \text{sec} = 200 / \text{msec}$, which is equivalent to the throughput of a typical array processor.* Note however that our opto-electronic Fourier transforming scheme achieves this throughput at a fraction of the cost of an array processor. Moreover, if we use 1024 elements detector arrays of 5 MHz bandwidth with the appropriate sine/cosine mask, then the throughput of the system can be increased to 1000 complex F.T. s/msec. Refinements and changes in the architecture employed in our work is expected to lead to improvement of this throughput figure by at least one order of magnitude. Such refinements will be considered in future research at the Electro-Optics and Microwave Optics Laboratory.

Instead of the sine/cosine mask and output anamorphic optics in the original implementation of the Fourier camera [4] it is possible to use a high speed discrete Fourier transform chip as illustrated in Fig. 19. The throughput of this proposed scheme depends also on the bandwidth and number of elements of the detector arrays, the

*For example, Floating Point System (P.O. Box 23489, Portland, Oregon 97233). Model AP-120B, has a throughput of 1024 complex FFT's in 4.75 msec.

R : image rotator
 L₁ : spherical lens
 L₂ : cylindrical lens
 P² : dispersive prism
 D_R : Red line scan detector
 D_B : Blue (or green) line scan detector
 DFT: Discrete Fourier Transform
 Signal Processor

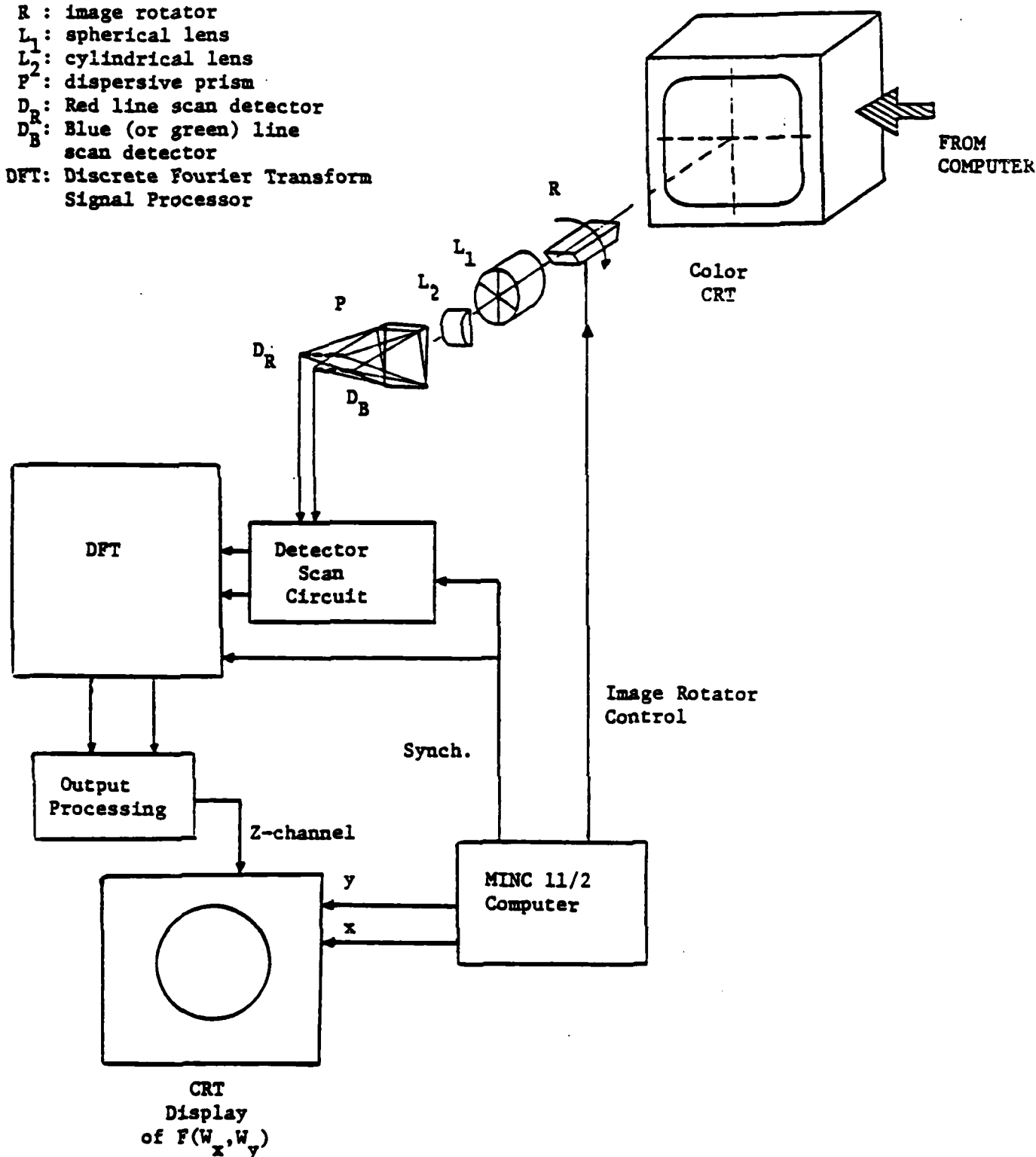


Fig. 19. An implementation of the Fourier camera using an electronic Fourier transform chip instead of the sine/cosine mask and output detectors approach described in ref. [4].

maximum sampling rate of the DFT signal chip and on the rotation rate of the image rotator. Using 512 elements detector arrays of 5 MHz bandwidth (Reticon S series), the image rotator used in our work, and a Reticon R5601 DFT signal processor of 2 MHz maximum sampling rate, a throughput of 2000 complex F.T.'s/msec should be attainable. Investigation of this scheme is underway.

Relation of the Fourier Camera to the Fourier Theory Model of Human Vision

In recent years a Fourier theory model of human vision has been advanced by several workers [6],[7]. An excellent recent review of research in this field in optical information processing in the human visual system in general is given in [8]. The model postulates the existence of parallel spatial frequency channels in the human visual system (eye-brain system) that can analyze the spatial frequency content of a natural scene. Neural, phsyco-physical, and electrophysiological evidence is mounting on the presence of elements in the neural network that are sensitive only to specific spatial frequency components of a scene at specific orientations. Note that the value of the Fourier transform $F(\omega_x, \omega_y)$ at any point ω_x, ω_y of the ω_x - ω_y plane represents the amplitude and phase of the spatial frequency component of frequency $\omega_r = (\omega_x^2 + \omega_y^2)^{1/2}$ and orientation $\tan^{-1} (\omega_y/\omega_x)$. The Fourier camera produces the 2-D Fourier transform $F(\omega_x, \omega_y)$ of a natural 2-D object scene $f(x,y)$ in individual radial lines that form a polar format. This is achieved by rotating the image of the scene before taking its projection and its 1-D Fourier transformation which in accordance to the projection-slice theorem yields one radial line in the polar formatted Fourier transform F of the scene. It is clear then that the data contained in this line is nothing but a repre-

sentation of the spatial frequency components of the scene along the direction of the line. Such spatial frequency analysis could have been obtained for example by superimposing on the object source $f(x,y)$ a series of masks or gratings of cosinusoidal transmittance of different frequencies but all at the same orientation (normal to the direction of the line in the Fourier plane) and measuring the integrated brightness. The Fourier camera performs this superposition and analysis simultaneously. As the object is rotated relative to the input plane of the camera or vice versa (by means of an image rotating dove prism) polar formatted Fourier analysis of the 2-D scene is realized. This is a unique and extremely important property of the Fourier camera. Its possible similarity to human vision makes it a valuable tool in the study of modeling of human and insect vision and for application in robotic vision and remote sensing. Of great significance is the possibility of interfacing of the Fourier camera with feature extraction schemes that are insensitive to object distortion (displacement, rotation, scaling) and automatic classification [9],[10] or to content addressable memories [11].

Another intriguing potential application of the Fourier camera is in airborne 3-D mapping using a spot-light imaging mode. An airborne Fourier camera can be automatically oriented during flight over an area of interest to look allways at the same scene area but from different aspect angles determined by the flight path. The resulting multiaspect 2-D Fourier transforms obtained in this fashion and stored in a digital memory represent in accordance to the projection-slice theorem central or meridional slices of the 3-D Fourier transform of the scene. Thus an efficient and fast way of accessing the 3-D Fourier transform of the scene can be realized. Fourier inversion of the data collected

in this manner can yield a 3-D image of the scene area which can be presented tomographically in vertical (height) slices for example to give a true 3-D height contour map. Note this capability could simplify and increase the accuracy of stereo-photogrammetry. Because of a potential for multispectral Fourier transforming capability in the Fourier camera, the above 3-D Fourier analysis and 3-D image reconstruction can be performed for different selected color components of the scene separately and simultaneously providing thereby a valuable capability hitherto unattainable in other airborne and satellite-borne remote sensing systems. Such 3-D multispectral capability can be very useful in scene analysis and surveillance and also for automatic recognition and classification and robotic vision.

Cross-Spectral Power Density Measurement with the Fourier Camera

In the theory of partial coherence the Van Cittert-Zernike theorem [12], [13] provides an expression for the cross-spectral power density $W(\bar{r}, \bar{r}, \nu)$ of the optical field produced by a planar spatially incoherent source in terms of the intensity distribution $I_\nu(\bar{\rho})$ of the source at spectral frequency ν . More specifically referring to Fig. 20,

$$W(\bar{r}_1, \bar{r}_2, \nu) = C e^{-j\frac{k}{2R} (r_1^2 - r_2^2)} \int_S I_\nu(\bar{\rho}) e^{-j\frac{k}{R} (\bar{r}_1 - \bar{r}_2) \cdot \bar{\rho}} d\bar{\rho} \quad (46)$$

where $\bar{\rho}$ is a position vector of a point on the source, $d\bar{\rho}$ is an element of area of the source, S is the area of the source, $k = 2\pi\nu/C$, C being the velocity of light is the wavenumber, C is a constant and \bar{r}_1 and \bar{r}_2 are position vectors of two points P_1 and P_2 in the observation plane for which the cross-spectral

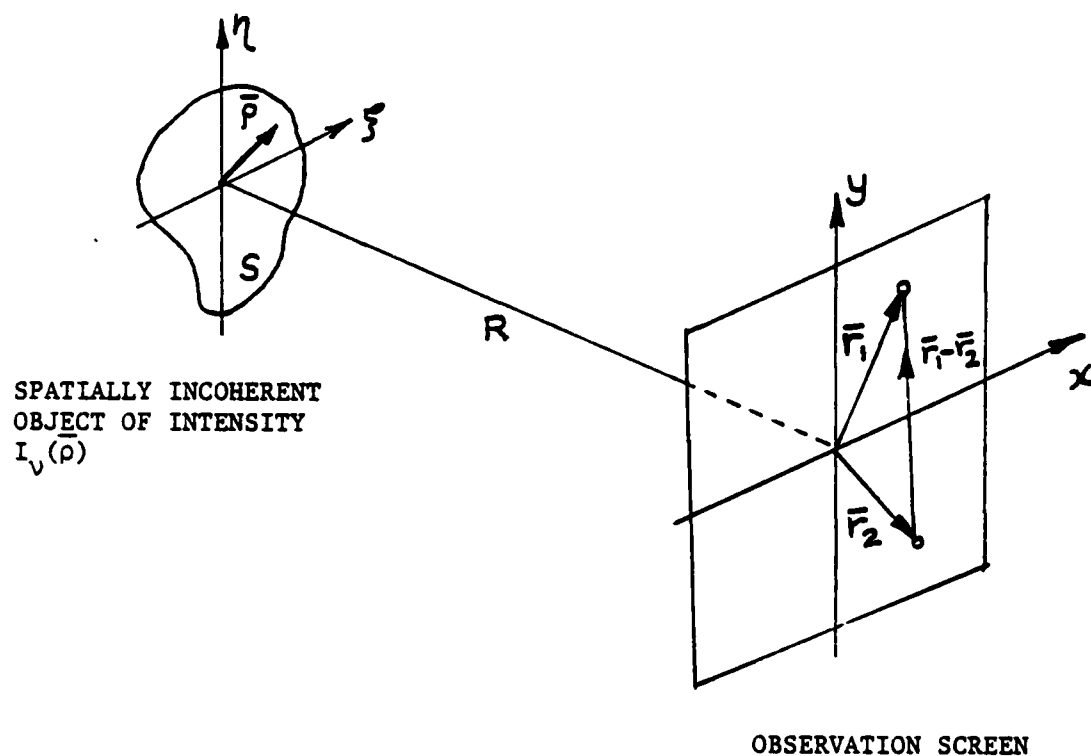


Fig. 20. Geometry for the Van Cittert-Zernike Theorem establishing the relation between the cross-spectral power density and the source intensity distribution $I_v(\bar{\rho})$.

power density is being computed. We note immediately that when $r_1 = r_2 = r$, i.e., case of symmetric scanning of P_1 and P_2 on the circumference of a circle of radius r , the above expression for $W(\bar{r}_1, \bar{r}_2, \nu)$ reduces to a Fourier transform relationship.

$$W(\Delta\bar{r}, \nu) = \int_{-\infty}^{\infty} I_{\nu}(\bar{\rho}) e^{-j\frac{k}{R} \Delta\bar{r} \cdot \bar{\rho}} d\bar{\rho} \quad (47)$$

where the constant C has been dropped and the integration extended to the entire ξ - η plane since the object is of finite extent. In the above expression $\Delta\bar{r} = \bar{r}_1 - \bar{r}_2$ is the vector joining P_2 to P_1 which is a chord of a circle of radius r . Because the Fourier camera can also measure the Fourier transform of the intensity distribution of an incoherent source viewed through a narrow optical filter of mean frequency ν we conclude that it also can measure the cross-spectral power density of the random wavefield produced by the source by simply using a series of optical filters of narrow adjacent pass bands. This spectrally selective measurement operation can be implemented more simply in our optical bench arrangement of the Fourier camera by inserting a rotating dispersive prism or other dispersive element before the detector array as shown for example in Fig. 19.

In our research during the current period, we have also developed a tomographic formulation of incoherent imaging of blackbody radiators which utilizes $W(\Delta\bar{r}, \nu)$ data. To see this we assume that the object is a black body radiator or one whose spectral dependence is independent of $\bar{\rho}$ such that,

$$I_{\nu}(\bar{\rho}) = G(\nu) B(\bar{\rho}) \quad (48)$$

where $B(\bar{\rho})$ is the brightness distribution of the object and $G(\nu)$ is its spectral distribution.

Then eq. (47) can be expressed as,

$$W(\Delta\bar{r}, \nu) = G(\nu) \int_{-\infty}^{\infty} B(\bar{\rho}) e^{-j\frac{k}{R} \Delta\bar{r} \cdot \bar{\rho}} d\bar{\rho} \quad (49)$$

Accordingly knowledge of $G(\nu)$ permits Fourier inversion of $W(\Delta\bar{r}, \nu)/G(\nu)$ to obtain the object spatial brightness $B(\bar{\rho})$. It is interesting to note however that a back-projection reconstruction algorithm can also be applied in this case. To see this let the object be composed of a collection of *point emitters* or *emitting centers* described by,

$$B(\bar{\rho}) = \sum_i a_i \delta(\bar{\rho} - \bar{\rho}_i) \quad (50)$$

where a_i is the strength of each emitter and $\bar{\rho}_i$ is its position vector. Combining eqs. (49) and (50) we obtain,

$$\begin{aligned} W(\Delta\bar{r}, \nu) &= G(\nu) \sum_i a_i \int_{-\infty}^{\infty} \delta(\bar{\rho} - \bar{\rho}_i) e^{-j\frac{k}{R} \Delta\bar{r} \cdot \bar{\rho}} d\bar{\rho} \\ &= G(\nu) \sum_i a_i e^{-j\frac{k}{R} \Delta\bar{r} \cdot \bar{\rho}_i} \end{aligned} \quad (51)$$

Inverse Fourier transforming the above equation from the temporal frequency domain ν to a fictitious time domain t , we obtain,

$$\begin{aligned} h(\Delta\bar{r}, t) &= g(t) * \sum_i a_i \int_{-\infty}^{\infty} e^{-j\frac{2\pi\nu}{cR} \Delta\bar{r} \cdot \bar{\rho}} e^{j2\pi\nu t} d\nu \\ &= g(t) * \sum_i a_i \delta\left(t - \frac{\Delta\bar{r} \cdot \bar{\rho}_i}{cR}\right) \end{aligned} \quad (52)$$

or,

$$h(\Delta\bar{r}, t) = \sum_i a_i g(t - \frac{\Delta\bar{r} \cdot \bar{\rho}_i}{cR}) = \sum_i a_i g(t - t_i) \quad (53)$$

where

$$t_i = (\Delta\bar{r} \cdot \bar{\rho}_i) / cR \quad (54)$$

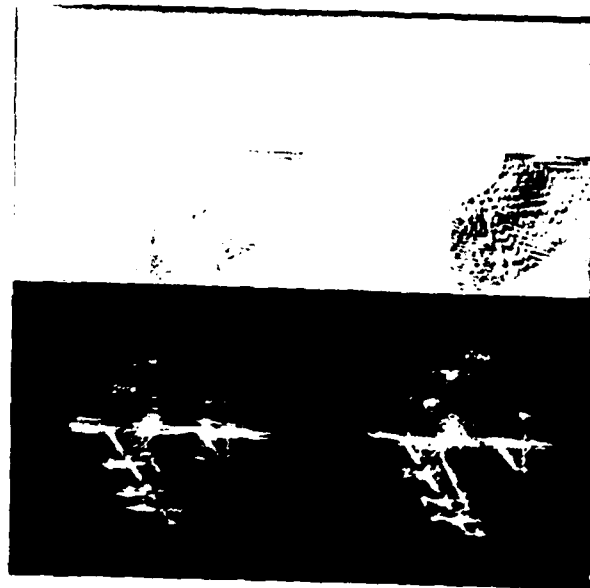
Now if $G(v)$ is of sufficiently broad extent, $g(t)$ will be quite narrow and $h(\Delta\bar{r}, t)$ will consist of a series of narrow weighted impulses located at t_i . In view of eq. (54) all emitting centers for which $\Delta\bar{r} \cdot \bar{\rho}_i = \text{const.}$ contribute to the same time delayed peak. Since $\Delta\bar{r} \cdot \bar{\rho}_i = \text{const.}$ describes the position vectors $\bar{\rho}_i$ of points lying on lines normal to $\Delta\bar{r}$ we conclude that Fourier transforming $W(\Delta\bar{r}, v)$ yields the projection of the emitting center of the object on $\Delta\bar{r}$. Because $\Delta\bar{r}$ can be altered in direction alone by symmetric scanning of both \bar{r}_1 and \bar{r}_2 in Fig. 20 (i.e., by rotating \bar{r}_1 and \bar{r}_2 while keeping the angle between them fixed) we conclude that projections of the emitting centers of the object in any desired direction in the ξ, η plane of Fig. 19 can be obtained by the above measurement procedure. A filtered back-projection algorithm identical to that used in the coherent active imaging case discussed in Section 2.1 is therefore applicable. The above considerations provide a new way of viewing incoherent imaging in general and establish a relation between the Fourier camera, cross spectral power density measurements by symmetric scanning, and projection imaging.

In light of the above discussion the distinct possibility emerges that the human visual system also processes the information in $W(\bar{r}_1, \bar{r}_2, v)$. Is it

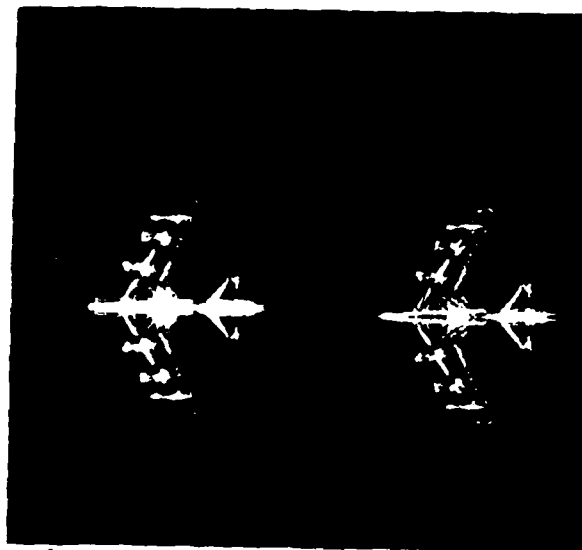
possible that symmetric scanning or more correctly, sampling, is also utilized in the retina by proper neural interconnections?. This and many other questions and ramifications of the above briefly described investigation will be examined in our proposed future research. It can be shown that $W(\bar{r}_1, \bar{r}_2, v)$ immediately in front of the pupil is not altered by the eye's lens and therefore $W(\bar{r}_1, \bar{r}_2, v)$ on the retina is that of the object wavefield. Our future research under the Fourier camera task and the 3-D incoherent imaging task to be discussed below will continue to examine these relationships with the aim of developing new insights in optical information processing by the eye-brain system. Such insights would naturally be of value in the design of man made systems for automatic pattern recognition and classification in general and for our microwave tomographic imaging radars in particular.

2.3 Image Enhancement Studies

During the current period our effort of seeking super-resolved imagery from our λ and polarization diversity data continued. Figure (21) shows an example of recent refined results demonstrating the degree of image enhancement achieved by combining polarization diversity, symmetry, and edge enhancement in the imaging of our metalized 100:1 scale model of the B-52 employing realistic microwave scattering data collected in our anechoic chamber facility. The frequency range employed was (6-17.1) GHz and the data was collected for 128 azimuthal aspect angles extending from 0° (head-on orientation of the B-52) to 90° (broad-side orientation). Fig. 21 (a) shows the copolarized Fourier



(a)

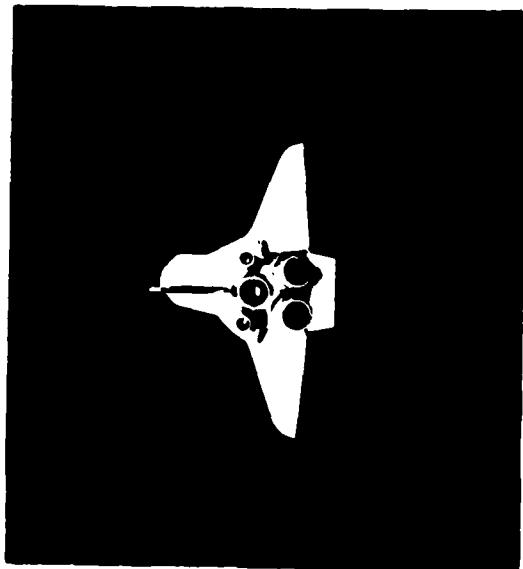
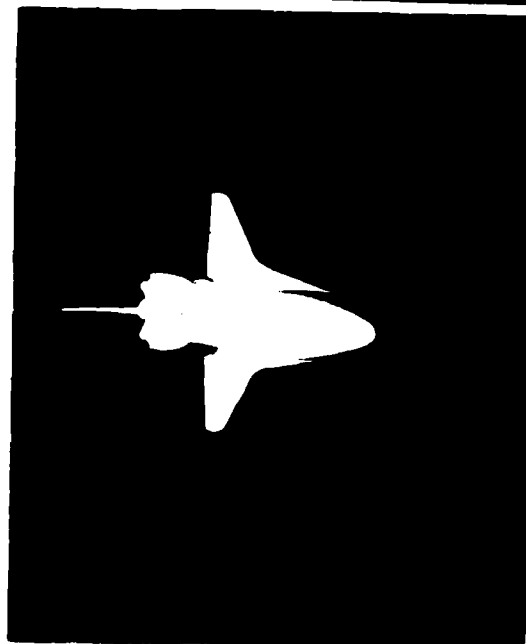


(b)

Fig. 21. New results demonstrating microwave image enhancement by polarization diversity and apriori knowledge of symmetry in the (6-17.1) GHz range utilizing a 90° angular aperture.

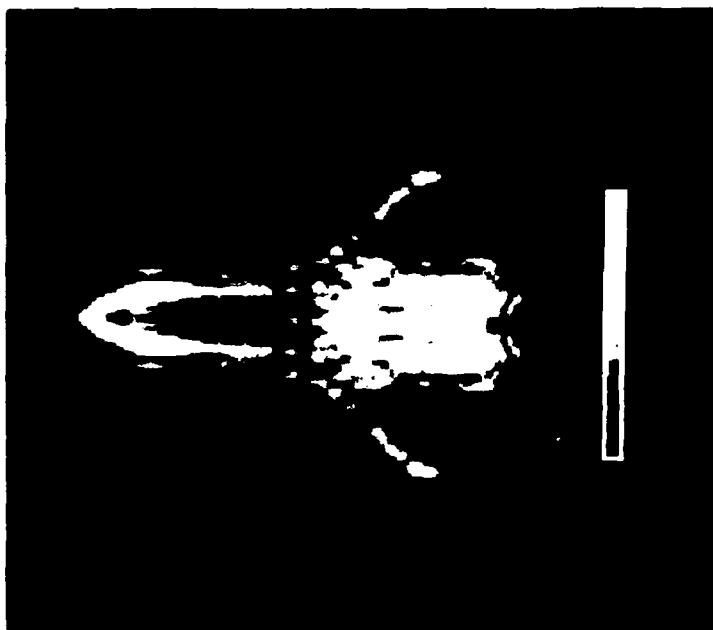
space slice data obtained in this fashion (top left) and the cross-polarized Fourier space slice (top right). Underneath each of these is shown the image retrieved by 2-D Fourier inversion of the data in each slice. Figure 21(b) shows the polarization and symmetry enhanced image (left) obtained by adding the co-polarized and cross-polarized images of Fig. 21(a) followed by symmetrization. The result of edge enhancement of the polarization and symmetry enhanced image by application of a 16-th order 2-D FIR Hamming filter [14] is shown in Fig. 21(b) (right). It is seen that the filtering operation brings out the dual cylindrical structure of the jet engines and other fine characteristic features traceable to the model. In future research we intend to examine the effect on the above images of adding (2-6) GHz scattering data to cover a (2-17) GHz range. The gear for extending the operational range of our imaging facility down to 2 GHz has been received and incorporated in the measurement system. Future plans under this task will also include the application of iterative spectral extrapolation namely the Gerchberg-Papoulis algorithm [15],[16] and comparison of the result with actual measurements over the extrapolated range. The results of this task will be of practical importance specially when data is acquired in several narrow non-overlapping bands and interpolation techniques are applied to fill in the gaps to enhance image quality.

Another recent example is the polarization and symmetry enhanced image of a 72:1 metalized scale model of the space shuttle shown in Fig. 22(b). The Fourier space data for this test object was obtained in exactly the same manner as for the B-52 test object. Comparison of the detail in the image in Fig. 22(b) with the pictorial views of the space shuttle model given in Fig. 22(a) shows



(a)

Fig. 22. Three pictorial views of the space shuttle test object (a), and symmetry enhanced microwave image showing intricate detail of the engines and tail section (b).



(b)

2.4 Dielectric Imaging

Summarized here is our progress to date in the study of frequency and polarization diversity projective and tomographic imaging of dielectric bodies. Noticeable improvement in image quality over that reported earlier has been achieved.

(i) Theory of Three-Dimensional Conductive and Dielectric Projective Imaging

Detailed vector treatments of 3-D tomographic microwave imaging by wavelength and polarization diversity have been given in earlier work [19],[25]-[27]. Here we recall the main results in the context of imaging dielectric bodies. The notation used here differs slightly from that used earlier.

The problem geometry assumed in our projective dielectric and conductive imaging studies, shown in Fig. 23, is that of an incident plane wave which scatters from a *homogeneous* dielectric of index N or a perfectly conducting shell. From knowledge of the incident and scattered wavevectors \underline{k}_{inc} and \underline{k}_{sc} and the scattered field $\underline{\psi}_{sc}(\underline{x})$ at the observation point defined by \underline{r} , one can find the vector object function $\underline{\gamma}(\underline{x})$ as follows. The scattered field is given exactly by

$$\begin{aligned} \underline{\psi}_s(\underline{x}, k) = i\omega\mu \int \underline{J}(\underline{x}') G(\underline{x}, \underline{x}') d\underline{x}' \\ + \frac{i}{\omega\epsilon} \int \nabla\nabla \cdot \underline{J}(\underline{x}') G(\underline{x}, \underline{x}') d\underline{x}' \end{aligned} \quad (55)$$

where $G(\underline{x}, \underline{x}')$ is the free-space Green's function, \underline{J} is the induced current in the object and μ_0 and ϵ_0 are the permeability and permittivity, respectively.

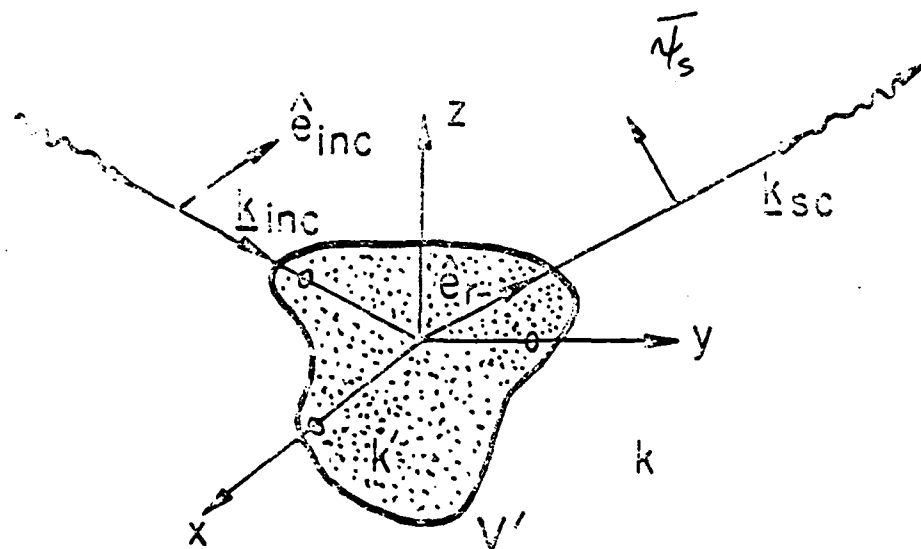


Fig. 23. Geometry of three-dimensional scattering problem.

Invoking the following approximations:

<u>Conductor</u>	<u>Dielectric</u>
o Far field	o Far field
o Physical optics or Born	o Rayleigh-Gans or Born
o Plane wave illumination	o Plane wave illumination

yields the following integral expression for the object function $\gamma(\underline{x})$.

$$\psi_s(\underline{x}, p) \approx \underbrace{\alpha_D}_\text{constant} \underbrace{e^{ikr}}_\text{Range term} \int_{\substack{S' \\ V'}} \underbrace{\gamma(\underline{x}')_C}_\text{Object function} \underbrace{e^{ip \cdot \underline{x}'}}_\text{Fourier kernel} d\underbrace{x'}_3 \quad (56)$$

where

$$p \triangleq \underline{k}_s - \underline{k}_i \quad (57)$$

$$\alpha_C = \frac{i\omega\mu_0}{2r} \quad (58)$$

$$\alpha_D = \frac{k^2}{4\pi r} \quad (59)$$

and where r is the distance from the scatterer to the observer. Here the subscripts C and D refer to "conductor" and "dielectric", respectively and the subscripts "2" and "3" indicate the dimension of integration over value V' or its covering surface S' . The two vector object functions of interest are given as

$$\underline{j}(\underline{x}')_C = \begin{cases} \underline{j}_s(\underline{x}') - [\underline{j}_s(\underline{x}') \cdot \hat{n}] \hat{n} & \text{\underline{x}' on S'} \\ 0 & \text{elsewhere} \end{cases} \quad (60)$$

and

$$\underline{\gamma}(\underline{x}')_D = \begin{cases} [\hat{\epsilon} - (\hat{\epsilon} \cdot \hat{n}) \hat{n}] (N^2 - 1) & \underline{x}' \text{ in } V' \\ 0 & \text{elsewhere} \end{cases} \quad (61)$$

The unit vector \underline{n} is the unit vector in the normal direction of observation while $\hat{\epsilon}$ denotes the unit polarization vector of the illuminating field.

Relation (56) can be inverted to yield the Fourier transform pair

$$\underline{\Gamma}(\underline{p}) = \int \underline{\gamma}(\underline{x}) e^{i\underline{p} \cdot \underline{x}} d\underline{x} \quad (62)$$

$$\underline{\gamma}(\underline{x}) = (2\pi)^{-3} \int \underline{\Gamma}(\underline{p}) e^{-i\underline{p} \cdot \underline{x}} d\underline{p} \quad (63)$$

where

$$\underline{\Gamma}(\underline{p}) = \alpha_C^{-1} e^{-ikr} \underline{\psi}_S(\underline{x}, \underline{p}) \quad (64)$$

To image dielectrics or conductors, the following steps are taken.

- o Measure $\underline{\psi}_S(\underline{x}, \underline{p})$
- o Calculate $\underline{\Gamma}(\underline{p})$ using (64)
- o Calculate the vector image $\underline{\gamma}(\underline{x})$ from (63)
- o Calculate the scalar image

$$\gamma(\underline{x}) \triangleq [\underline{\gamma}(\underline{x}) \cdot \underline{\gamma}(\underline{x})^*]^{1/2}$$

It is often useful to use the backprojection algorithm to calculate the necessary Fourier transforms in (65) and (66). This can be done starting with

(65) and introducing the variable

$$\xi \triangleq x \cos\phi + y \sin\phi$$

where the angle ϕ is defined by

$$p_x \hat{e}_x + p_y \hat{e}_y = p \cos\phi \hat{e}_x + p \sin\phi \hat{e}_y$$

and \hat{e}_x and \hat{e}_y denote unit vectors. Defining

$$B(\xi) \triangleq \int_0^\infty \underbrace{|p| \Gamma_{\text{proj}}(p, \phi)}_{\text{filtered projection}} e^{ip\xi} \frac{dp}{2\pi} \quad (67)$$

one finds

$$\gamma_{\text{slice}}(x, y) = \frac{1}{2\pi} \int_0^{2\pi} B(\xi) d\phi \quad (68)$$

Thus the two-dimensional Fourier transform of (66) has been reduced to the one-dimensional Fourier transform of (67) plus an integration. The results of this signal processing are exemplified in the figures below for actual experimental data. Fig. 24 shows the magnitude of the Fourier-space (\bar{p} -space) data $|\Gamma_{\text{proj.}}(p_x, p_y)|$ (left-side) collected in the regime 6-17 Hz. for a thin-walled 30 cm dielectric cylinder containing a smaller offset dielectric cylinder. The cylinders are rotated through 2π steradians in our anechoic chamber and the complex backscattered signal \underline{x} , is recorded. The interference pattern of the two cylinders is evident in the Fourier-space data. The reconstruction, using a two-dimensional Fourier transform to evaluate the object function slice (66) is also shown in Fig. 2 (right-side). This high resolution image of the dielectric clearly shows the internal structure of

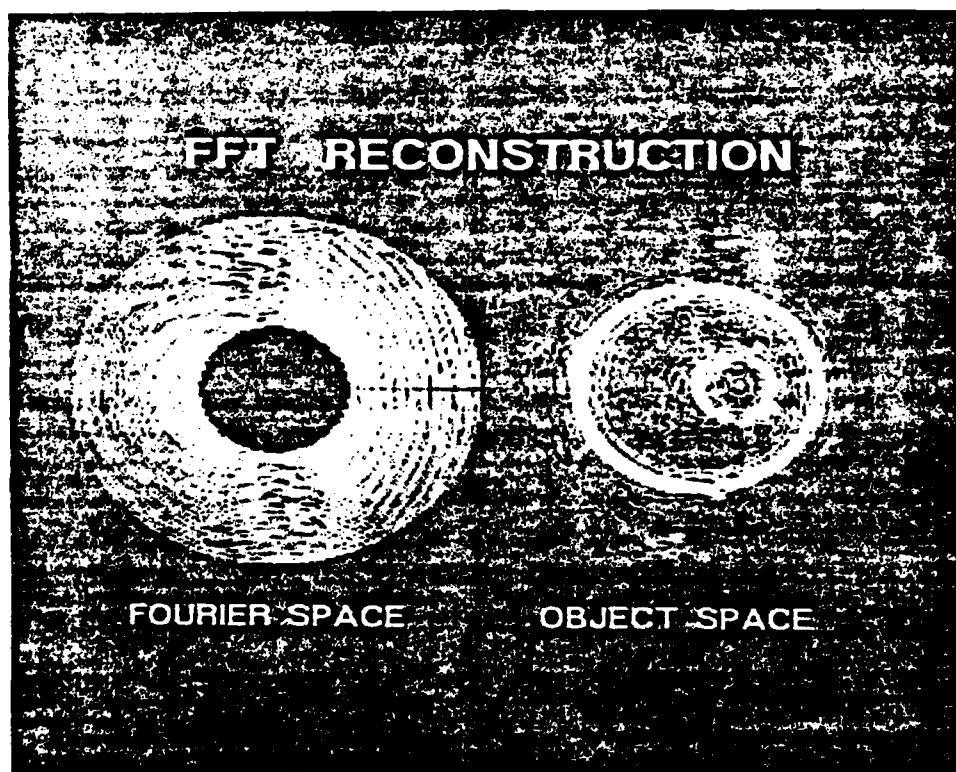


Fig. 24. Magnitude of Fourier domain projection data $|\Gamma_{\text{proj.}}(p_x, p_y)|$ (left) and the reconstructed object slice $|\gamma_{\text{slice}}(x, y)|$ for an offset cylinder inside a larger cylinder (right).

the imaged object. The resolution R is given by

$$R = \frac{c}{2 \Delta f N} 1.5 \text{ cm} \quad (69)$$

in agreement with observed results.

A comparison of the experiment with a computer simulated experiment is shown in Fig. 25, again using the two-dimensional Fourier transform to evaluate the object function slice. Here the similarities between the two reconstructions is striking down to the interference artifacts along the object boundaries.

Further reconstruction techniques involved with the back projection reconstruction as defined in (67) and (68) and appropriate sampling techniques are presently under evaluation. A preliminary result using a cylinder containing several dielectric plates is shown in Fig. 26. Here the back projection reconstruction (left) is compared with the two-dimensional Fourier transform reconstruction (right). The artifacts introduced by the discrete implementation of these two schemes and their comparative efficiency and quality and under present study.

(ii) Theory of One Dimensional Profile Reconstructions

A method has been developed here for a fast and efficient numerical scheme which can be used to invert inhomogeneous refractive profiles from a scattering data (see Fig. 27). This data is in terms of the reflection coefficient $r(k)$ or the impulse response

$$R(y) = \frac{1}{2\pi} \int_C r(k) e^{-iky} dk \quad (70)$$

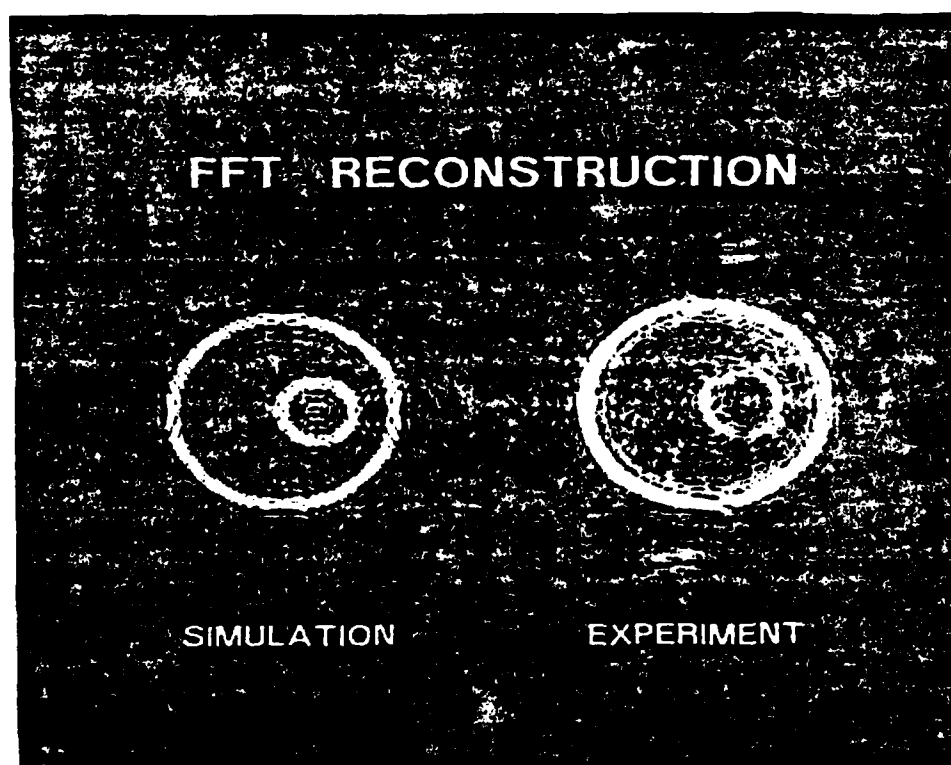


Fig. 25. Comparison of reconstruction using computer simulated data (left) with a reconstruction using experimental data (right). Note the similarities.

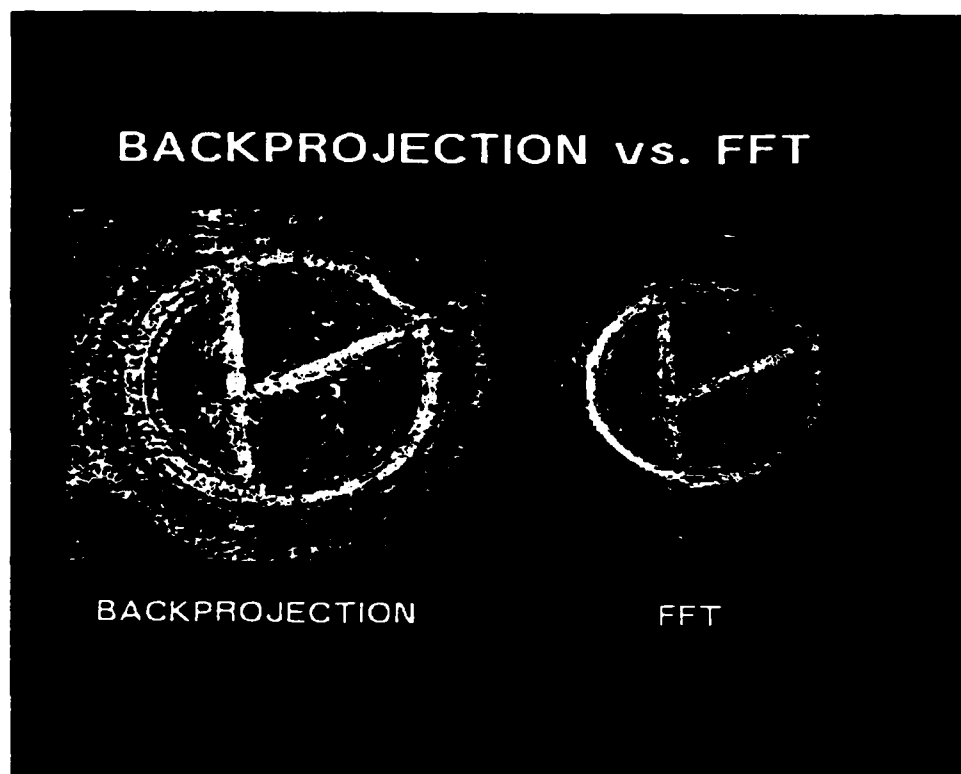


Fig. 26. Preliminary comparison of the backprojection reconstruction with the two-dimensional Fourier transform reconstruction for two dielectric plates bounded by a circular cylinder. Both reconstructions use real experimental data.

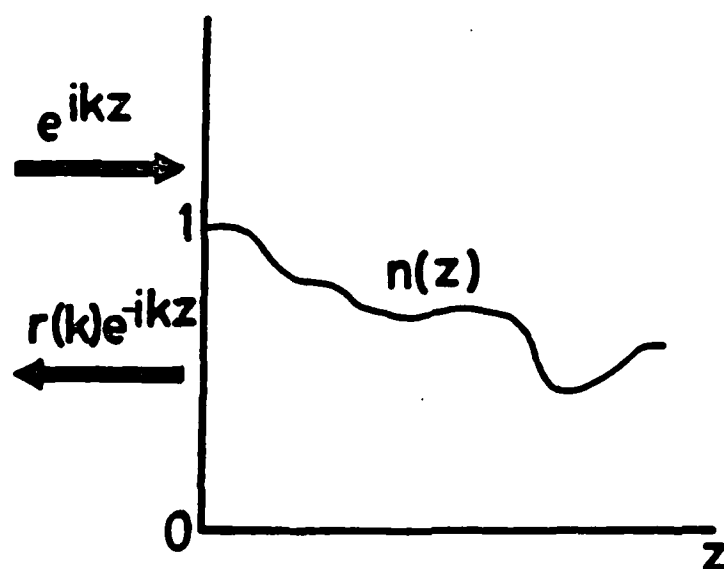


Fig. 27. Geometry of the problem considered here showing the incident and reflected waves e^{ikz} and $r(k)e^{-ikz}$, respectively. The (known) reflection coefficient is $r(k)$ and the (unknown) refractive index is $n(z)$. Here k is the wavenumber of the incident wave and z is the coordinate.

when y is normalized time and the contour C is chosen to preserve causality. As shown by us elsewhere [18] the solution to this problem is given by numerically solving the integral equation

$$K(x, y) = \int_{-y}^x [1 + K(x, x')] R(y + x') dx' \quad (71)$$

where $R(y + x')$ is known from the reflection data and the use of (70) for the unknown kernel function $K(x, y)$. It can be shown that the kernel function also satisfies the nonlinear hyperbolic equation [17]

$$\frac{\partial^2 K(x, y)}{\partial x^2} - \frac{\partial^2 K(x, y)}{\partial y^2} - \frac{2}{[1 + K(x, x)]} \frac{\partial K(x, y)}{\partial x} \frac{dK(x, x)}{dx} = 0 \quad (72)$$

with the condition

$$K(x, y) = 0 \quad |x| < y. \quad (73)$$

The refractive index profile is reconstructed from the kernel function by the relation

$$n[z(x)] = [1 + K(x, x)]^{-2} \quad (74)$$

where coordinates z and x are related by the integral

$$z(x) = \int_0^x [1 + K(x', x')]^2 dx'. \quad (75)$$

It is assumed that the refractive index and its first derivative are continuous at the origin and that the refractive index is finite although those requirements may apparently be relaxed. A useful application of this method is to imprecise or imperfect reflection data. Most exact methods fail under these conditions. Consider the reconstructions shown in Fig. 28 for the case of noisy reflection data. Here the impulse response is contaminated with noise so that (70) is now replaced by

$$\tilde{R}(y) \triangleq R(y) [1 + (S/N)^{-1} q(y)] \quad (76)$$

where S/N is the (amplitude) signal to noise ratio and $q(y)$ is a stochastic random process with a uniform probability distribution between -1 and $+1$. Here the tilde denotes the corrupted impulse response. Note the excellent reconstructions far into the slab for moderate and small values of signal to noise ($S/N \lesssim 1$). Clearly, the method developed here is extremely robust with respect to noise. Other attributes are given in [18].

Present work is involved with the examination of the effect of band-limited reflection data on the profile reconstructions, the experimental verification of this method and the determination of highly accurate approximate methods.

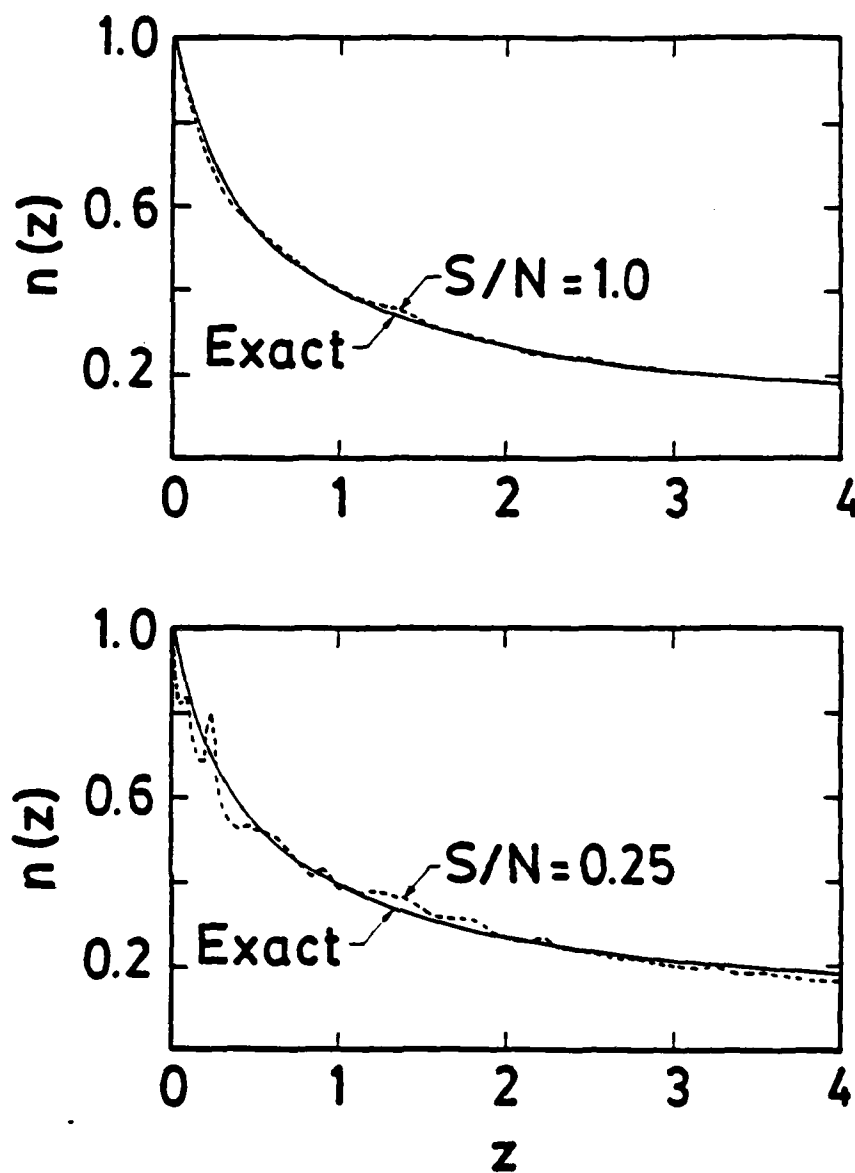


Fig. 28. Profile reconstruction for refractive index $n(z)$ as a function of coordinate z using a noise contaminated impulse response. The (amplitude) signal to noise ratio S/N is noted.

2.5 Projective and Tomographic Imaging of Incoherent 3-D Objects by Cross-Spectral Power Density Measurement

In this section we summarize our progress to date under this task. Theoretical considerations show that the concept of 3-D tomographic imaging by wavelength diversity is extendable to incoherent radiation and thus to thermally emitting objects [28]. Verification of this concept can lead to true passive 3-D imaging (radiometry or thermography) capabilities with important implications in surveillance, remote sensing and possibly radio-astronomy. Specifically we have shown, [28], that spectrally selective cross-correlation measurements or equivalent cross-spectral density measurements of the random wavefield emitted by a 3-D incoherent source of brightness distribution $b(\vec{r})$ can be employed to access the 3-D Fourier space $B(\vec{p})$ of the emitter where $\vec{p} = k(\vec{l}_{R_1} - \vec{l}_{R_2})$. \vec{l}_{R_1} and \vec{l}_{R_2} being unit vectors from an origin in the object in the directions of the observation points located at \vec{r}_1 and \vec{r}_2 and k being the wavelength (central wavelength of the synchronously tuned filters used to achieve spectral selectivity in the correlator arms).

Successful verification of the concept was achieved recently employing acoustic noise emission rather than microwave emission because of easier and less costly implementation. Because of the large ratio of velocity of light to velocity of sound ($\approx 10^6$) the same wavelength ranges of interest in incoherent microwave frequencies can be achieved with sound frequencies that are 10^6 times lower i.e., sound spectra in the KHz range.

Two acoustic measurement systems have been implemented to experimentally verify and study 3-D interferometric imaging of incoherent objects. Both measure the cross-spectral power density. One directly by spectrally selective cross-correlation measurements (see Fig. 29) and the other indirectly (see Fig. 30), by measuring the coherence function $\Gamma(\vec{r}_1, \vec{r}_2, \tau)$ first, then Fourier trans-

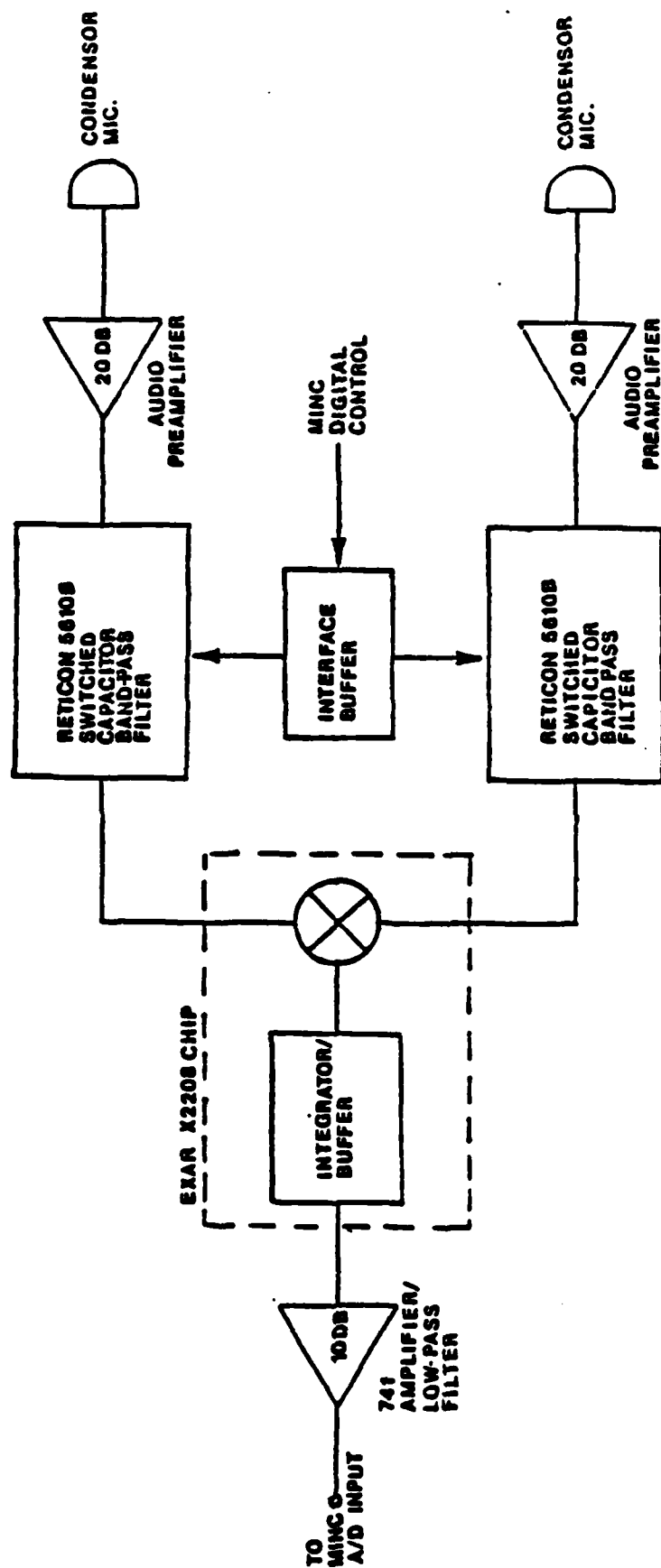


Fig. 29. System for 3-D imaging of incoherent acoustic objects by automated spectrally selective cross-correlation measurement in the (4 - 18) KHz acoustic range.

forming $w \cdot r$ to τ , to obtain the cross-spectral power density $w(\bar{r}_1, \bar{r}_2, \nu)$, ν being the frequency and where \bar{r}_1 and \bar{r}_2 are the position vectors of the transducers. The receiving transducers in both systems are wide-band condenser microphones each located approximately 8 meters from the object. The angle between them as seen from the object is approximately 60° . The object itself shown in Figs. 32(b), 34 and 35 consists of 5 dome tweeters arranged in a 3-D array on an elevation azimuth positioner. The rotation of the pedestal is controlled via stepper motors SM1 and SM2 by a MINC 11 Computer which also coordinates system data acquisition and storage.

The first system shown in Fig. 29 utilizes digitally controlled dual switched capacitor band-pass filters that select quasimonochromatic bands of the received signals. The Q of these filters is on the order of 200 which implies a 50 Hz bandwidth at 10 KHz. The filter outputs are multiplied and integrated to form an estimate of the cross-spectral density. The second system is based upon measurement of the mutual coherence function. By the well known Weiner-Kintchin Theorem the cross-spectral power density and the mutual coherence function are a Fourier transform pair. Hence knowledge of the former leads to determination of the latter via a discrete Fourier Transform. This system is shown in Fig. 30. It utilizes two CCD20 48 stage bucket brigade devices in order to achieve a programmable analog delay. The MINC 11 Computer can program the delay time in $7\mu s$ increments. The mutual coherence function is measured by changing the delay in one channel relative to the other channel. The product of the two channels is then integrated to yield an estimate of the coherence function. The width of the correlation peak resulting from a point source is inversely related to the bandwidth of the systems which in turn determines the range resolution. System resolution is found to be on the order of 1.5 cm. An example of a measured cross-correlation function of an incoherent point source, a single dome tweeter, is shown in Fig. 31. This was obtained with the arrangement of Fig. 30.

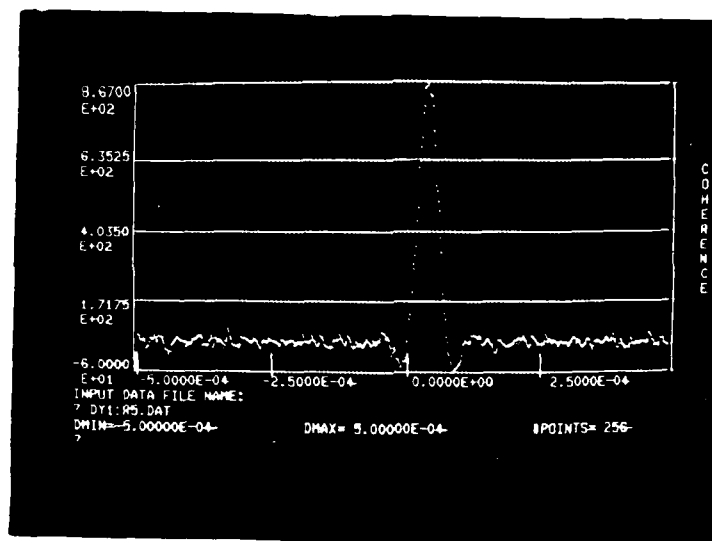


Fig. 31. Results of a cross-correlation measurement of an incoherent point source.

In order to obtain a three dimensional image of the 3-D test object described earlier the multiaspect cross-spectral density must be measured over as large a volume of Fourier space as possible. Successive slices of the object can then be retrieved using Fourier's domain projection theorems.

Recently, single slices or *correlograms* of the 3-D Fourier space $\bar{B}(\bar{p})$ of the incoherent test object were obtained. These correlograms were employed in a digital reconstruction scheme identical to that used in the reconstruction of our wavelength diversity holograms to produce the first projection images of a 3-D incoherent object.

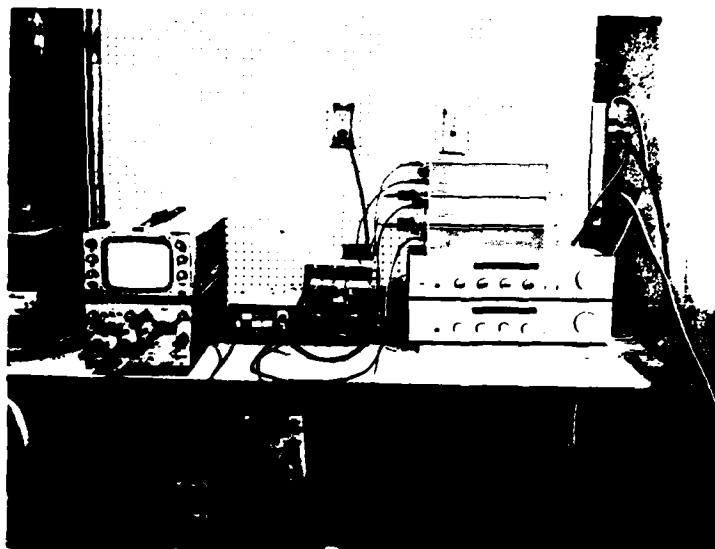
The results to be described below show the validity of applying the projection-slice theorem in the context here and are therefore indicative of the feasibility of tomographic imaging of 3-D incoherent objects from cross-spectral power density data. Note that our work differs from medical radio-

emissive tomography that is based on flux density measurements that are noninterferometric in nature.

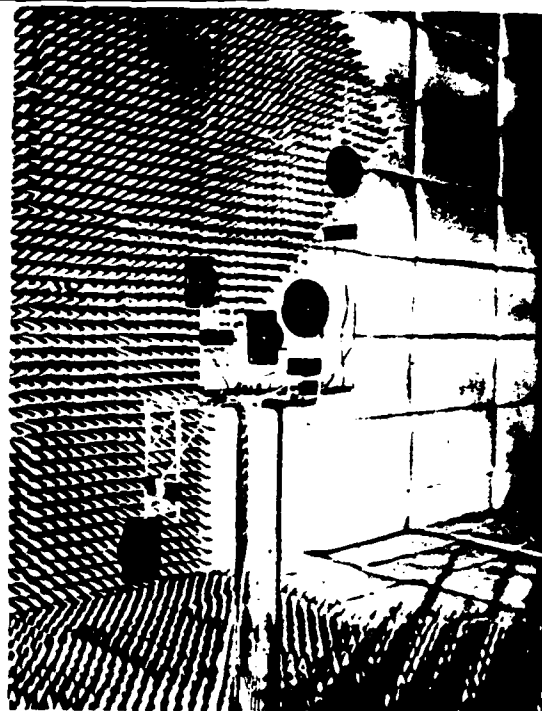
Pictorial views of the measurement system utilized are given in Fig. 32(a). The 3-D noise emitting object, shown in Figs. 32(b), 34, and 35, was realized using a 3-D formation of five acoustic tweeters as mentioned earlier excited from independent random noise generators in the (.6 - 13.5) KHz range. The tweeter assembly is mounted on a computer controlled elevation over azimuth positioner that is used to change their elevation angle θ and azimuthal angle ϕ relative to the sensors. The random wavefield produced was transduced at two points in space separated as seen from the object by angle $\theta \approx 60^\circ$ with the aid of two condenser microphones shown in Fig. 32(c) and the cross-spectral power density of their outputs was obtained using the indirect arrangement of Fig. 31.

The correlogram recorded when only two of the five tweeters, indicated in the top view given in Fig. 33(a), were excited is shown in Fig. 33(b).

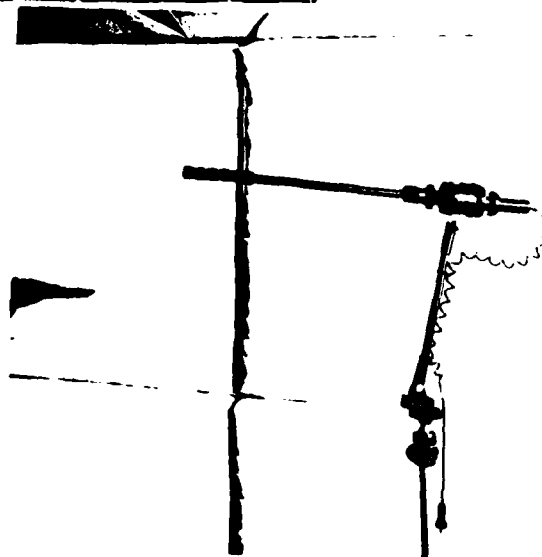
Figure 33(b) is the real part of the correlogram as recorded by changing ϕ in Fig. 33(a) over a range of 180° in 196 steps and plotting the measured cross-spectral density radially over a range equivalent to the (.6 - 13.5) KHz spectral window utilized. The correlogram consists of 196 radial lines each consisting of 48 frequency points and represents the data in a slice of the Fourier space of the object. A digitally interpolated version of this correlogram was obtained by a four-nearest-neighbors algorithm [20]. In accordance with the projection-slice theorem, Fourier inversion of the data in this slice should yield a projection image of the brightness distribution of the source as projected on a plane parallel to that of the slice. The results of 2-D digital Fourier inversion of the correlogram slice of Fig. 33(b) after interpolation is shown in Fig. 33(c). The result



(a)

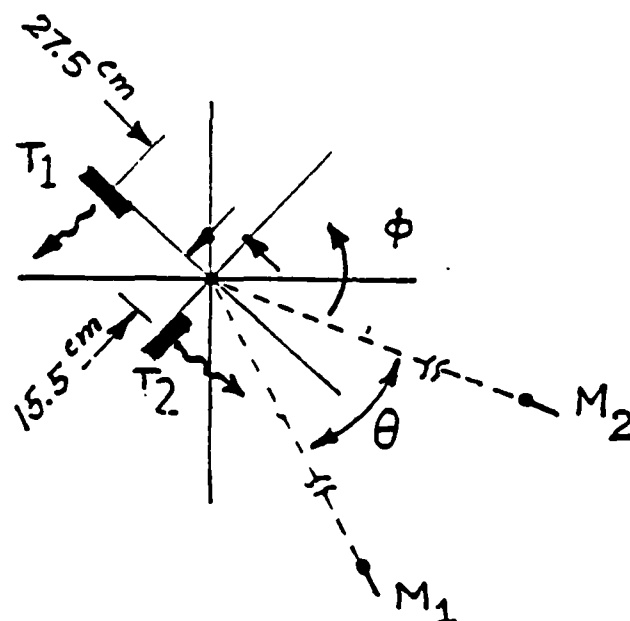


(b)

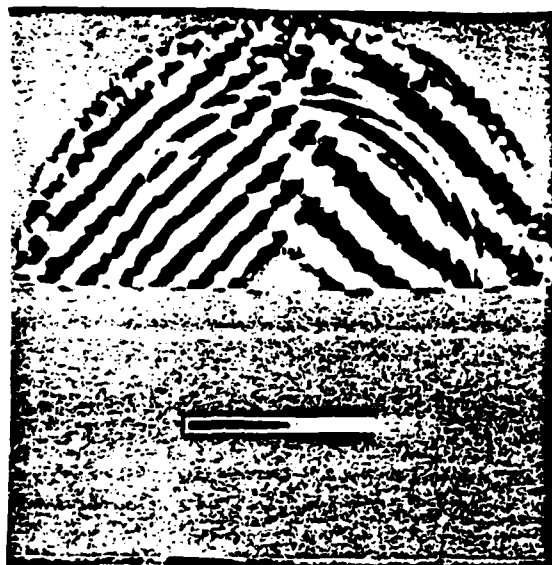


(c)

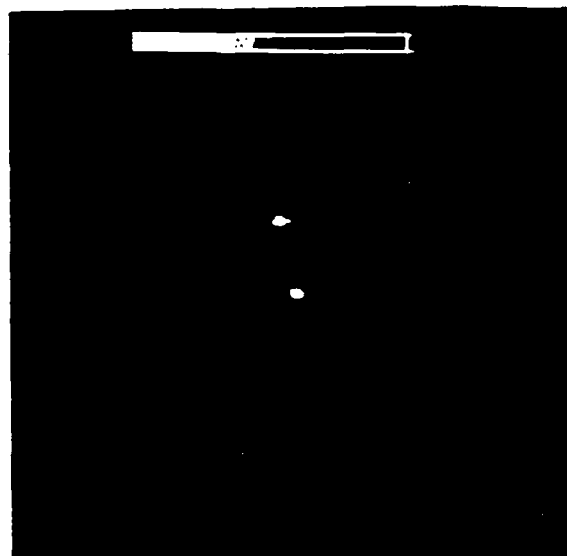
Fig. 32. Pictorial detail of measurement system employed in accessing a slice of the 3-D Fourier space of an incoherent 3-D acoustic source. (a) Instrumentation including amplifiers, programmable delays and multiplier. (b) View of 3-D distribution of five acoustic noise emitters (tweeters). (c) View of one of the two condenser microphones used for sensing the random acoustic field in the (.6 - 13.5) KHz range.



(a)

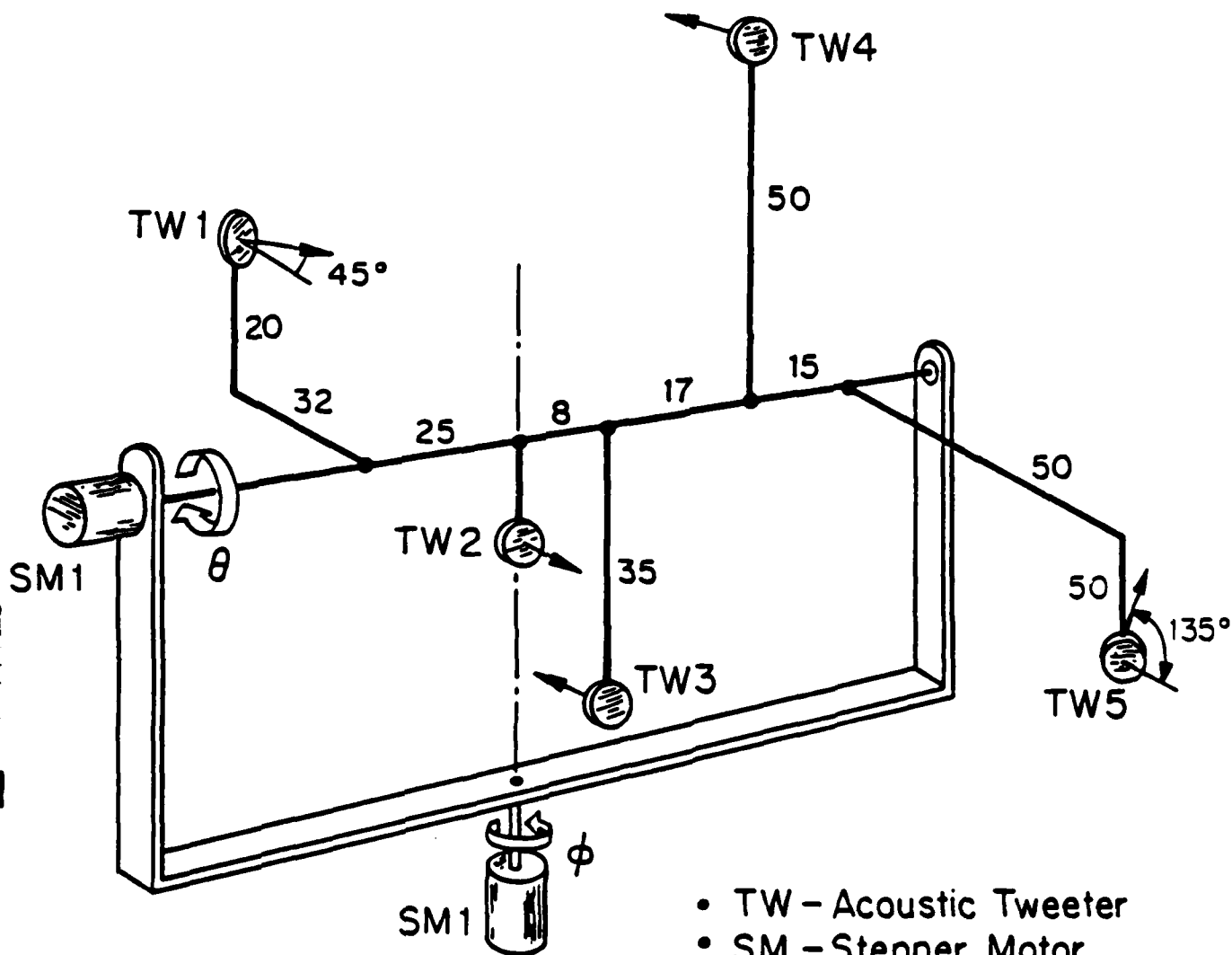


(b)



(c)

Fig. 33. Results of the first wavelength diversity correlation imaging experiment of two acoustic noise emitters (tweeters) in the (.6-13.5) KHz range. (a) Top view of source geometry (T_1 and T_2) relative to transducer microphones (M_1 and M_2). (b) Real part of Correlogram and (c) Digitally retrieved projection image.



- TW - Acoustic Tweeter
- SM - Stepper Motor
- Numbers indicate distances in cm
- Arrows on tweeters give directions of main beam

Fig. 34. Geometry of 3-D acoustic emitter consisting of 5 tweeters.
(Drawing is not to scale. See Fig. 35 for pictorial view)

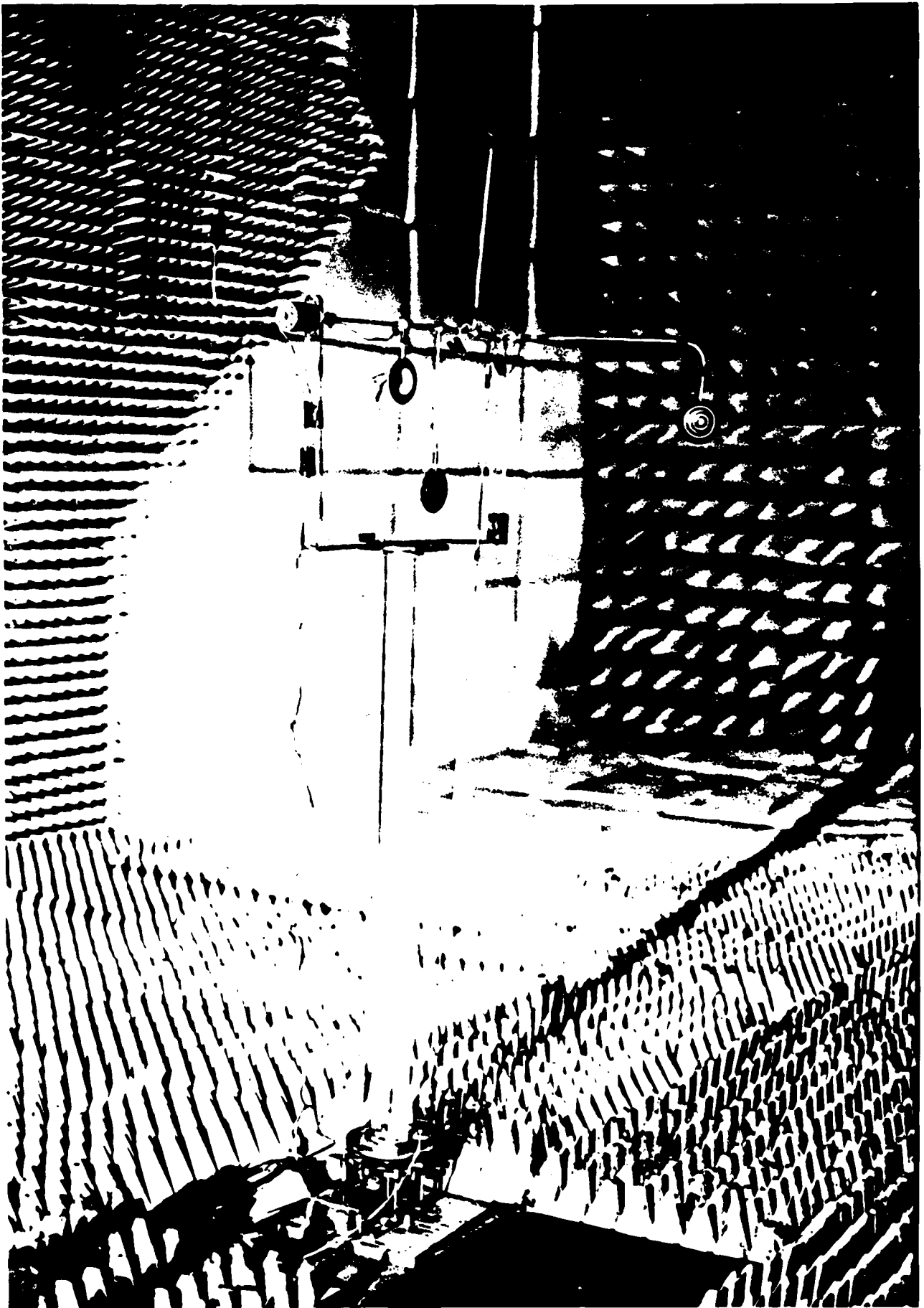


Fig. 35. Pictorial view of 3-D acoustic emitter consisting of 5 tweeters.

represents the first successful experimental verification of the concept of projective imaging of 3-D detail of an incoherently emitting object employing spectrally selective cross-correlation measurements or equivalent cross-spectral density measurement.

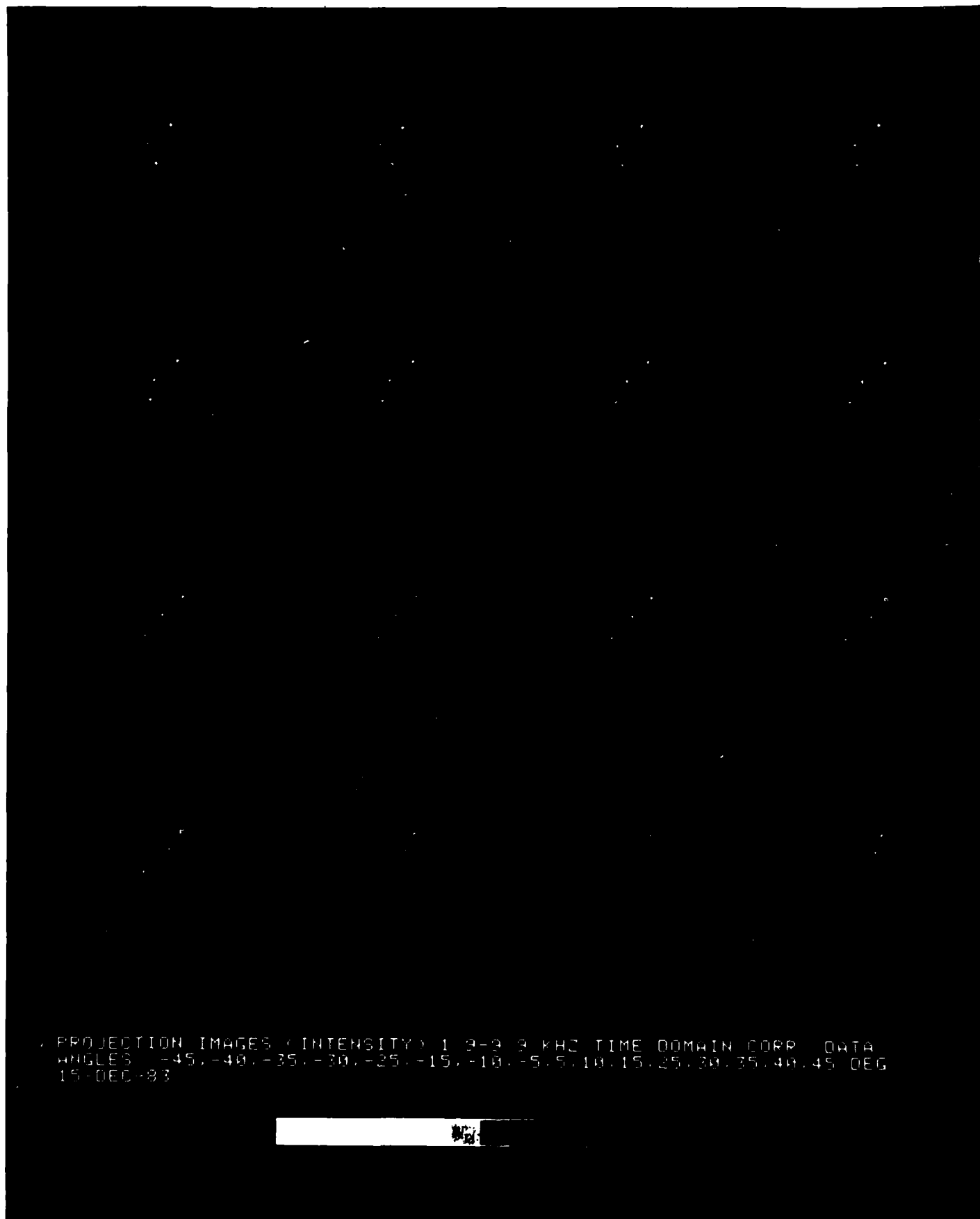
More recently similar slices of $B(\bar{p})$ were taken in steps of $\Delta\theta = 5^\circ$ for $-45^\circ \leq \theta \leq 45^\circ$. In this case three tweeters TW1, TW3 and TW5 (see Fig. 34) were activated. The rest were silent. The slices obtained are shown in Fig. 36. The corresponding reconstructed projection images are shown in Fig. 37. These agree exactly with the projection of the three tweeters on a horizontal plane as obtained for each value of θ . The above situation was also numerically simulated assuming 3 equivalent but isotropic noise sources distributed exactly as the 3-D configuration shown in Figs. 34 and 35. The slices of $B(\bar{p})$ computed for the same values of elevation angle θ and the same range of ϕ are shown in Fig. 38. These exhibit the same features of the measured results of Fig. 36 but the fringes of the correlograms shown are more defined because of the ideal (isotropic) nature of the radiators assumed in the simulation. The corresponding projection images obtained from these numerically produced correlograms are shown in Fig. 39. Comparison of these with the projection images shown in Fig. 38 as obtained from the measured data show excellent agreement.

The above results pave the way to true 3-D tomographic imaging of such objects and raise intriguing questions on the 3-D object information content in random wave-fields produced by thermally emitting objects.

It is worth noting that, as in the Fourier camera and the Fourier theory model of human vision (see Section 2.2), the cross-spectral power density $W(\bar{r}_1, \bar{r}_2, \nu)$ plays an important role also here in correlation imaging of incoherent 3-D objects. Our future research program will therefore also con-



Fig. 36. Sixteen slices of $B(\bar{p})$ (correlograms) taken at different values of θ . (Measurement).



PROJECTION IMAGES (INTENSITY) 1 3-3 3 KHZ TIME DOMAIN CORR DATA
ANGLES -45,-40,-35,-30,-25,-15,-10,-5,5,10,15,25,30,35,40,45 DEG
15-DEC-83

Fig. 37. Projection images obtained from the experimentally obtained correlograms of Fig. 36.

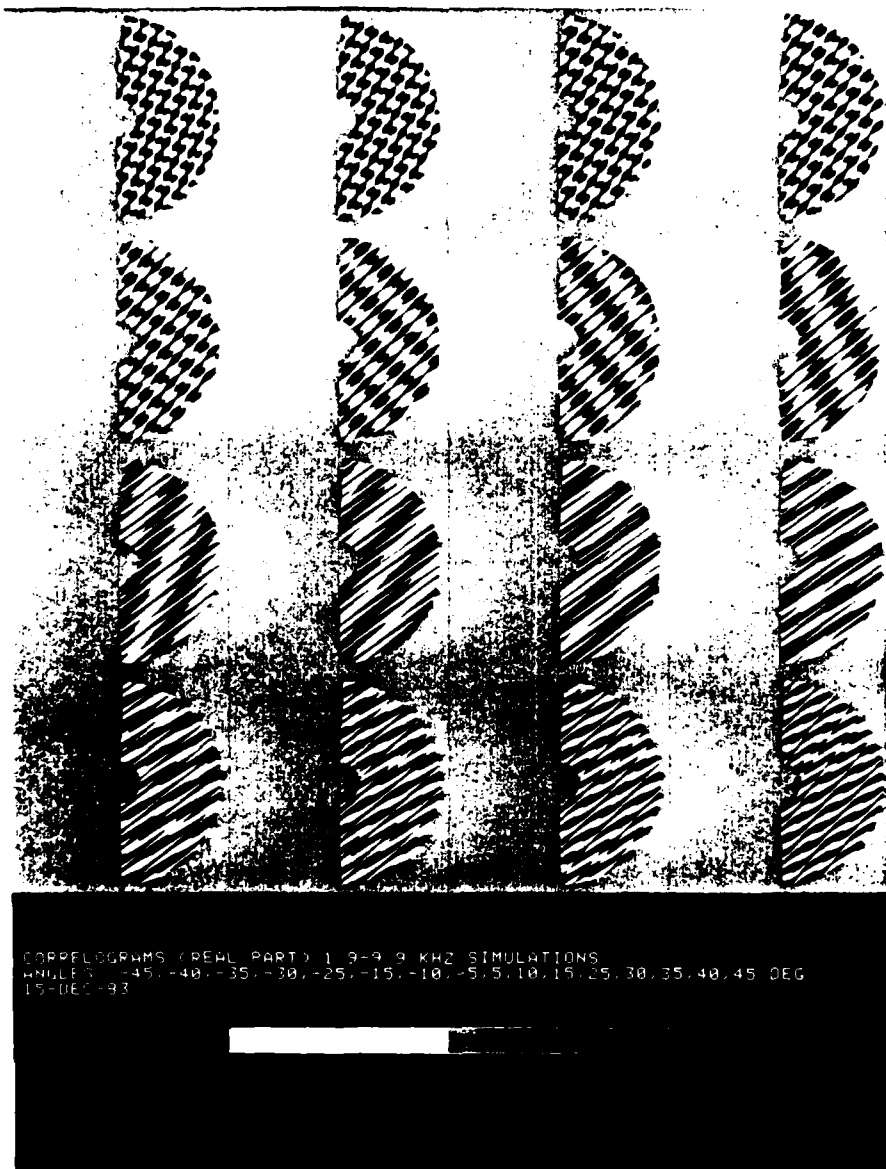


Fig. 38. Numerical simulation results. Sixteen correlograms corresponding to those measured and shown in Fig. 37.

PROJECTION IMAGES (INTENSITY) 1 3-9 9 KHZ SIMULATIONS
ANGLES -45, -40, -35, -30, -25, -15, -10, -5, 5, 10, 15, 25, 30, 35, 40, 45 DEG
15 DEC 83

Fig. 39. Projection images reconstructed from the numerically obtained data of Fig. 38.

centrate on examining the connection between the three situations to clarify if $W(\bar{r}_1, \bar{r}_2, \nu)$ plays a ubiquitous role in all broad-band incoherent imaging system. Again we hope the understandings and insights developed in this proposed task to be of value in the design of intelligent man-made imaging systems and remote sensing system capable of recognition, categorization, and classification.

2.6 Influence of the Sizes of the Angular and Spectral Apertures on Retrieved Image Quality

We have studied in the past the relation between the sizes of the angular and spectral windows used in data acquisition and retrieval image detail and quality. The results of this study are described here because of the relevance to the proposed research. Our studies to date have focused on the use of large highly thinned (sparse) broadband apertures that subtend relatively large solid angles as seen from the receiver for the imaging of remote objects. The images presented and discussed in Section 2.3 for example were obtained with a synthetic azimuthal aperture of 90° .

In practice, details of a given scatterer may be reconstructed when imaged in some directions but not in others, depending on which views are available. The effect of this phenomenon on reconstructed image quality can be studied by dividing the target frequency response (or Fourier space slice data) for example of the B-52 airplane (see Fig. 21) into two equal segments as shown in Fig. 40. The digitally reconstructed images from the data in these two aperture parts are shown in Fig. 41 and 42. The results show that segment I of the Fourier domain data contains information about scattering centers visible in a nearly front view of the target which include front parts of the wings, tails, fuselage and engines. On the other hand, the right half or segment II of the Fourier domain data contains mainly information on scattering centers that are seen in a more broadside view of the target which yields broadside detail of the fuselage, engines and fuel tanks. This demonstrates as expected that in practice the image information content, and therefore the resolution, depend on the target nature and on the range of aspect angles over which it is observed.

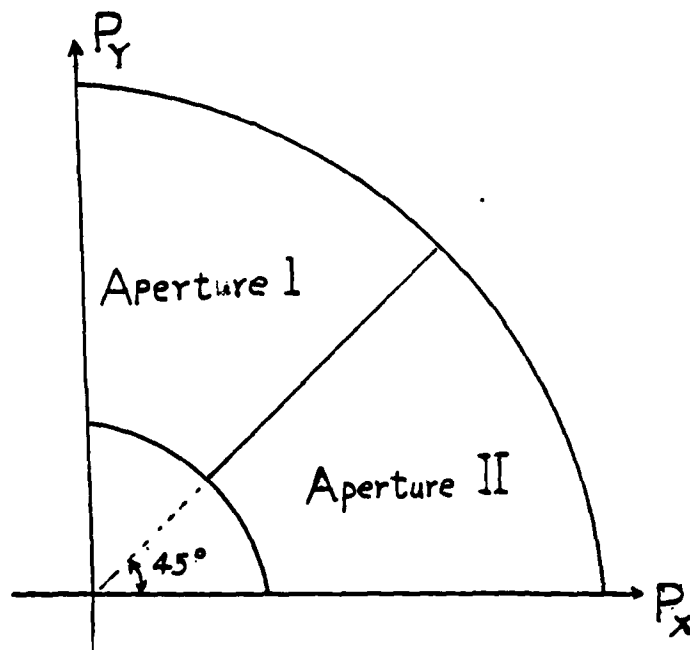


Fig. 40. Geometry for angular segmentation experiment.

AD-A150 098

RESEARCH IN IMAGE UNDERSTANDING AS APPLIED TO 3-D
TOMOGRAPHIC IMAGING WIT. (U) MOORE SCHOOL OF ELECTRICAL
ENGINEERING PHILADELPHIA PA ELECTR. N H FARHAT ET AL.

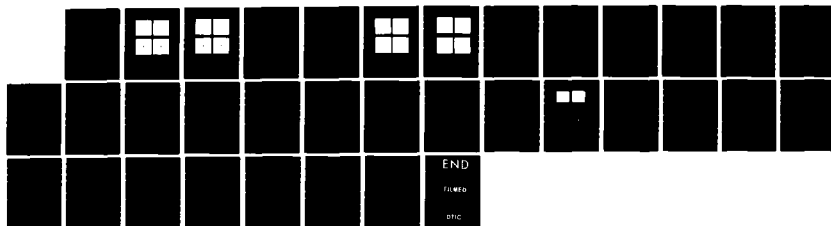
2/2

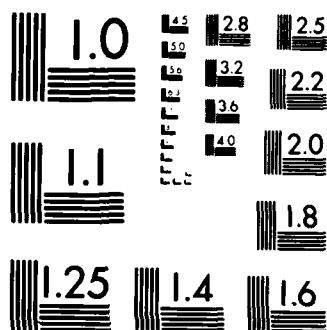
UNCLASSIFIED

30 NOV 84 EO/MO-7 AFOSR-TR-84-1230

F/G 17/9

NL





MICROCOPY RESOLUTION TEST CHART
NATIONAL BUREAU OF STANDARDS 1963-A

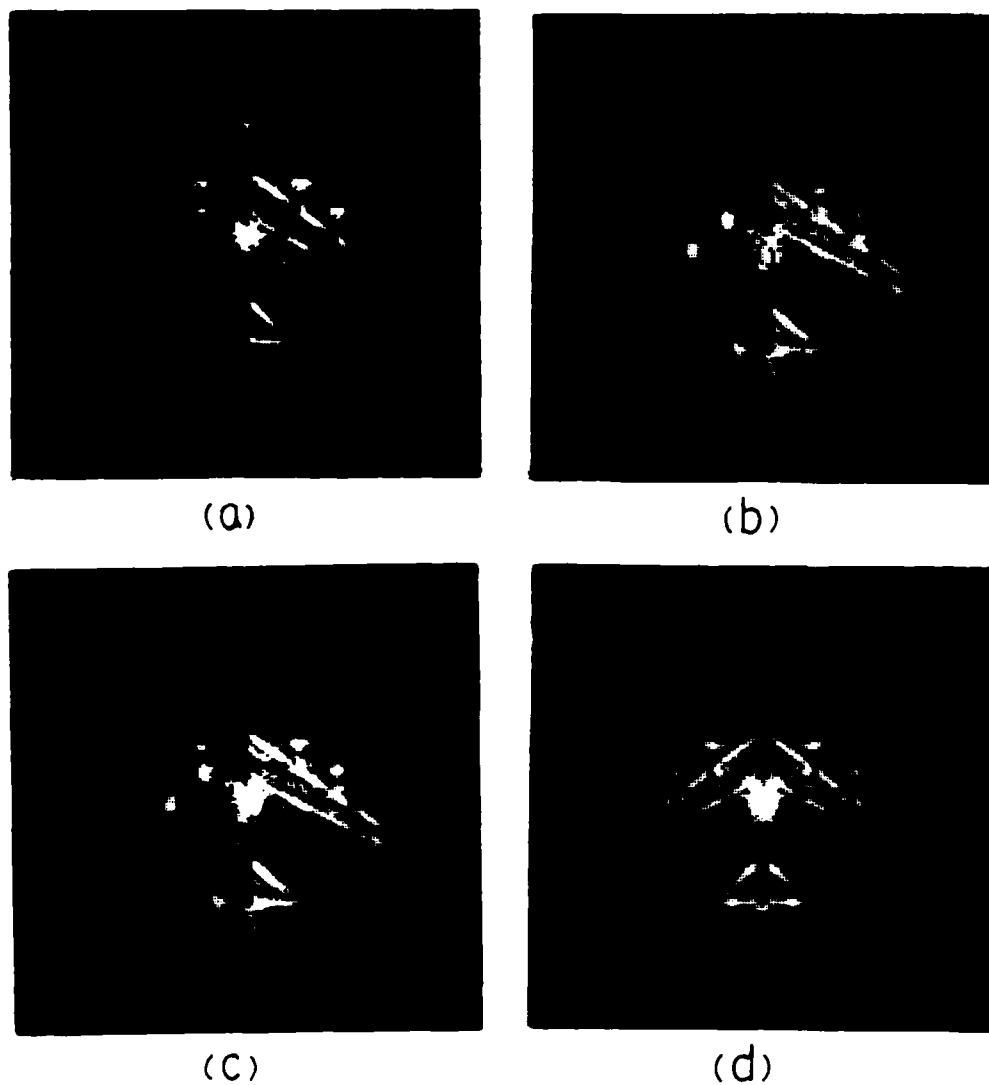
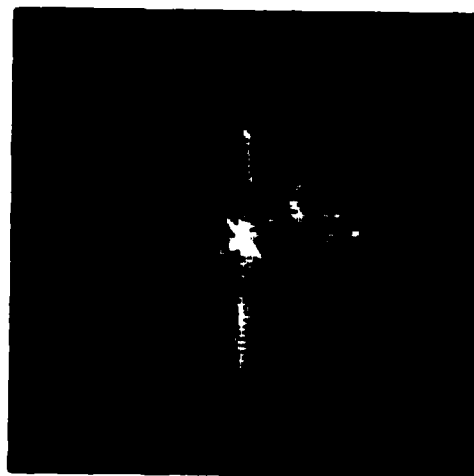
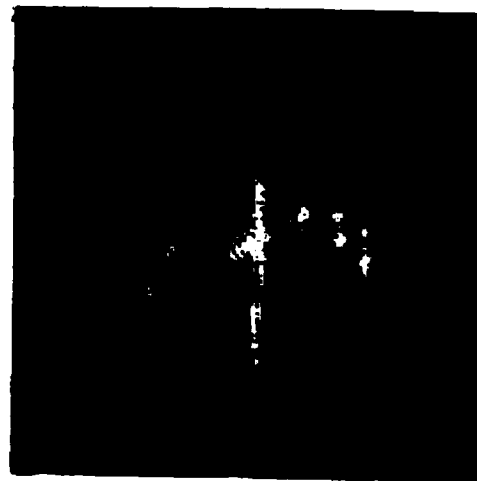


Fig. 41. Results obtained from aperture I of the frequency response of the B-52 airplane obtained from the data in Fig. 21.

- (a) co-polarized image (b) cross-polarized image
- (c) "polarization enhanced" image
- (d) "symmetry and polarization enhanced" image



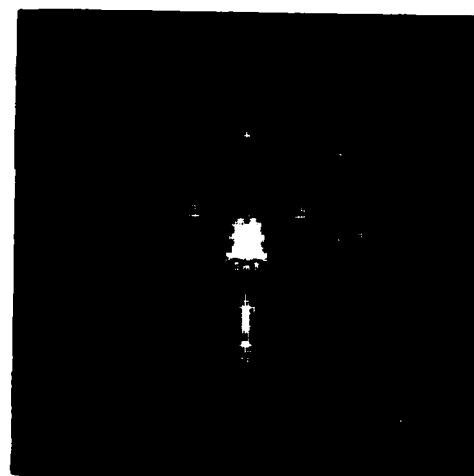
(a)



(b)



(c)



(d)

Fig. 42. Results obtained from aperture II of the frequency response of the B-52 airplane obtained from the dat in Fig. 21.

- (a) co-polarized image (b) cross-polarized image
- (c) "polarization enhanced" image
- (d) "symmetry and polarization enhanced" image

In a similar experiment, the B-52 model frequency response $\Gamma(\bar{p})$ is divided into two frequency bands, as shown in Fig. 43. The frequency band in the lower half section in the range of (6.1-12.1) GHz contains part of C-band and the entire X-band. The frequency band in the upper half section ranges from (11.1-17.1) GHz which contains the Ku-band. Both sections have a frequency bandwidth of 6 GHz, and as a result, the range resolution in each should be equal but lower than the range resolution achieved with the entire (6-17) GHz band by about a factor of two. The digitally reconstructed images for these two sections are given in Figs. 44 and 45. These figures show that the target scattering centers from the higher band illumination are delineated with slightly more detail and "ringing" than from the lower band but that both are poorer than quality of the images in Fig. 21 obtained from the entire available spectral window.

The above results show that when limited angular apertures must be used due to practical limitations higher frequency bands or spectral windows should be utilized. This statement can be appreciated by referring to Fig. 46 which depicts schematically the Fourier space or \bar{p} -space accessible by the same angular aperture (same angular diversity) with two equally sized spectral windows one in the (6-18) GHz and the other in (28-40) GHz. It is seen that the \bar{p} -space volume accessed in the (28-40) GHz range is larger than that accessed in the (6-18) GHz. A smaller angular aperture can therefore be used in the higher frequency band to access a volume equal to that accessed in the lower frequency band. This shows the desirability of working with shorter spectral windows when a limitation exists on the extent of the angular apertures that can be utilized. It must be kept in mind however that as the spectral window is moved to shorter wavelengths image "ringing" caused by the

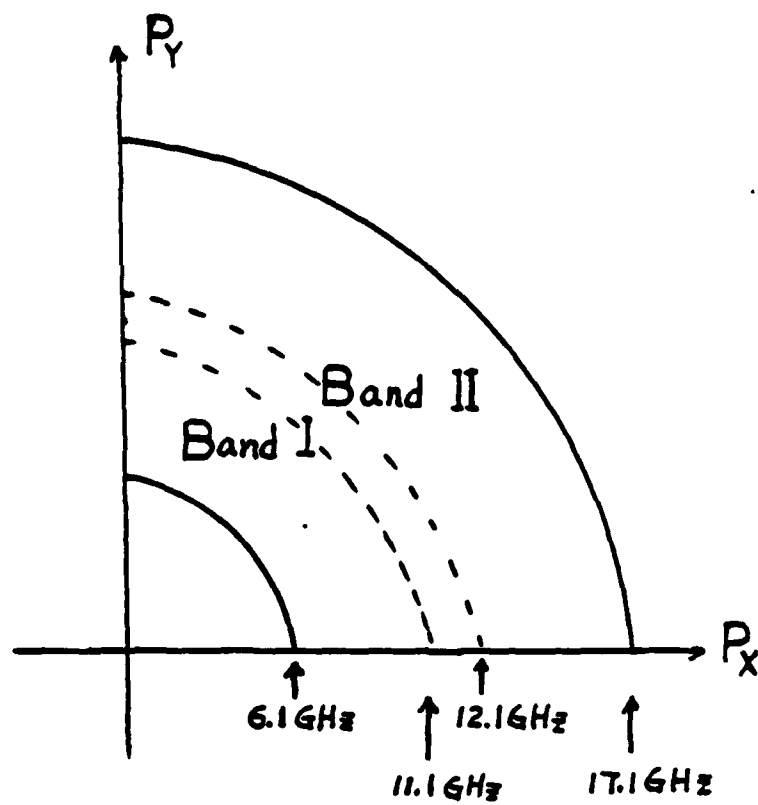


Fig. 43. Geometry for frequency band segmentation.

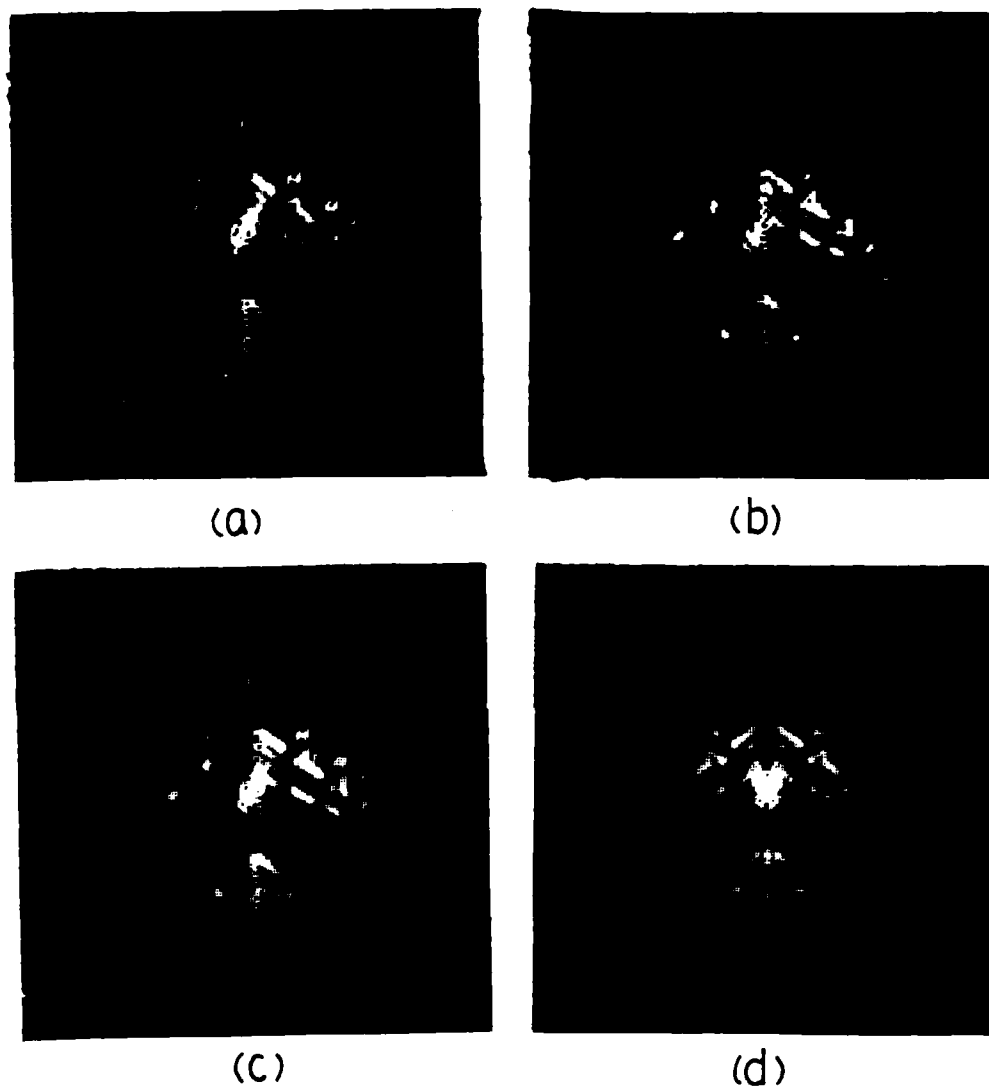


Fig. 44. Results obtained from band I of the frequency response of the B-52 airplane obtained from the data in Fig. 21.
(a) co-polarized image (b) cross-polarized image
(c) "polarization enhanced" image
(d) "symmetry and polarization enhanced" image

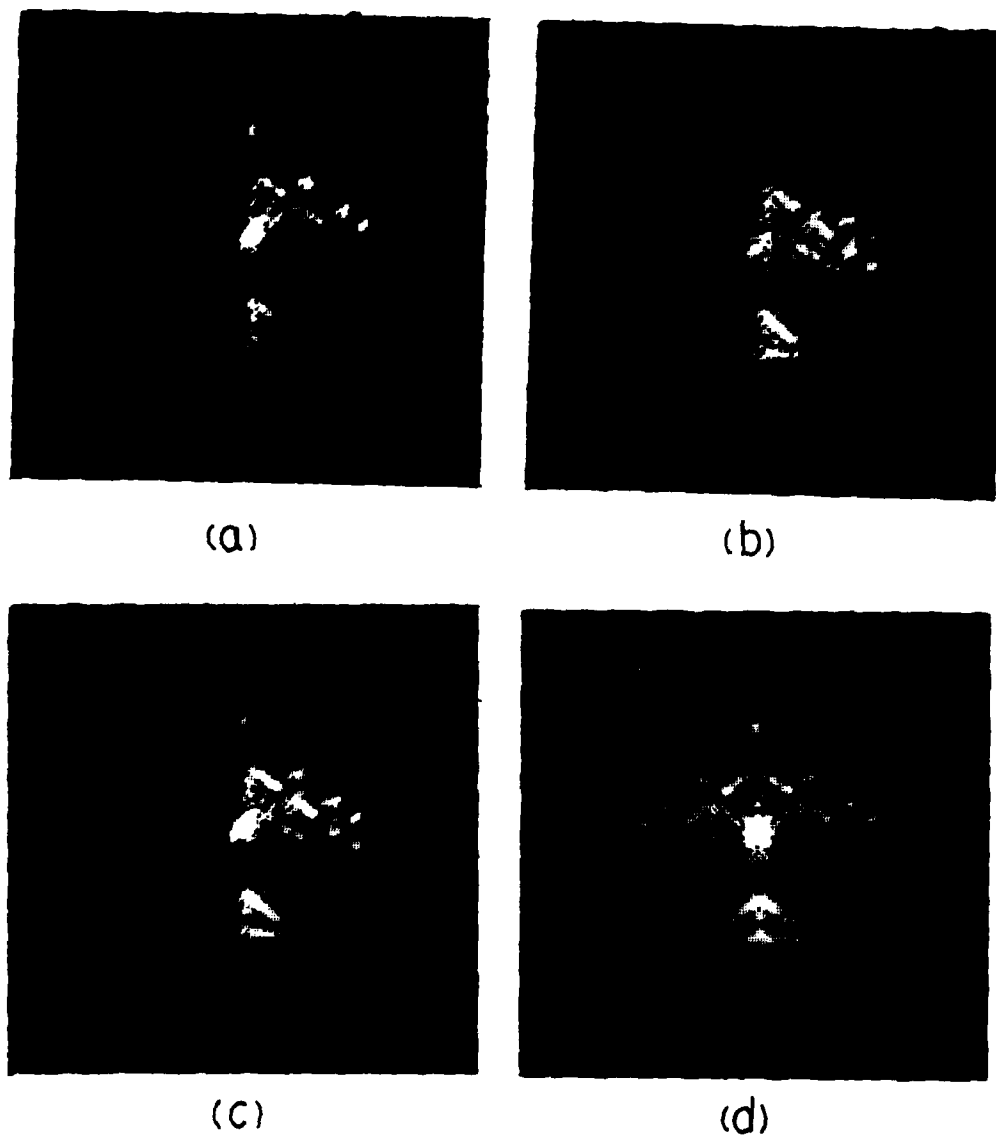


Fig. 45. Results obtained from band II of the frequency response of the B-52 airplane obtained from the data in Fig. 21.
 (a) co-polarized image (b) cross-polarized image
 (c) "polarization enhanced" image
 (d) "symmetry and polarization enhanced" image

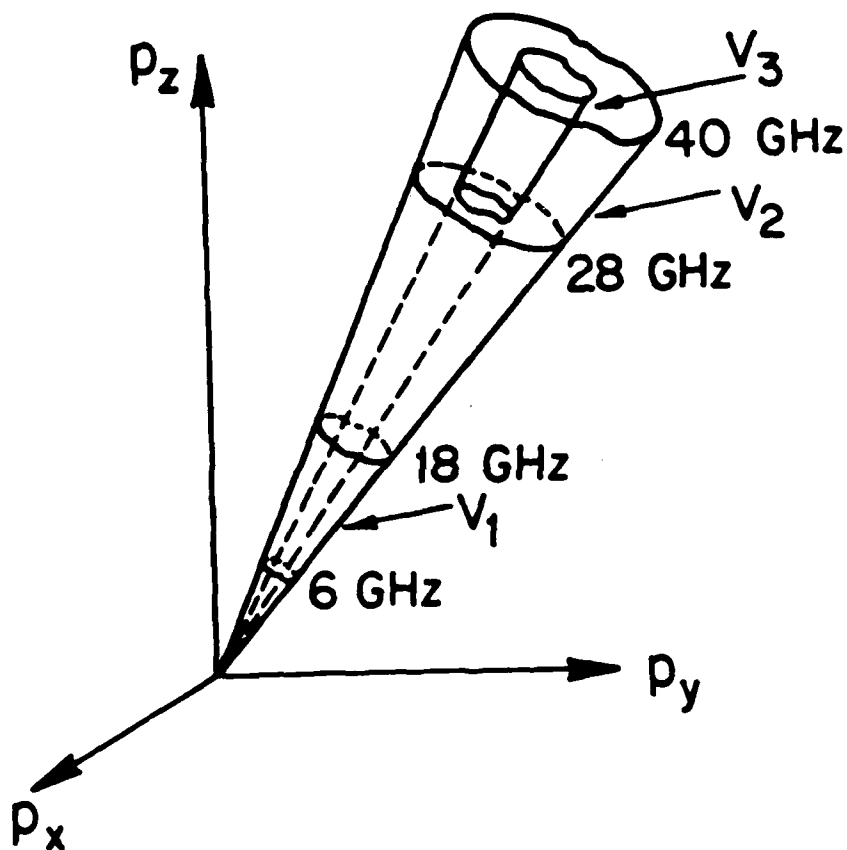


Fig. 46. Schematic representation of Fourier space volumes V_1 and V_2 accessed using spectral windows of the same extent one in the microwave range and the other in the millimeter wave range employing the same angular aperture. $V_3 = V_1$ is accessed in the millimeter wave range employing a much narrower angular aperture.

appearance of a higher frequency carrier in the system impulse response will occur. We conclude that narrowing the angular aperture requires extending the upper limit of the spectral window to shorter wavelengths but while keeping the lower limit fixed in order to minimize ringing. The study and verification of this conclusion is part of our future research were extension of the capabilities of our experimental microwave imaging facility into the millimeter wave range is planned.

2.7 Measurement System and Methodologies

So far in our experimental study of λ and polarization diversity imaging an automated frequency stepped mode of data acquisition has been developed and employed. The method utilizes a unique synthetic target derived reference method to remove the range phase information. The frequency stepped method has been shown to be well suited for laboratory applications where the scattering target is stationary. In the presence of target motion more rapid data acquisition methods are required. The aim of this task is to find efficient data acquisition modes that are specially suited for use with moving scatterers. Also, since it is highly desirable to extend the operational range of our measurement facility to the mmw range, methodologies for mmw frequency response measurement of stationary and moving objects in the laboratory are being considered under this task. The aim here is to increase resolution so as to be able to resolve fine detail on our 100:1 and 75:1 scale models of the B-52 and space shuttle that is equivalent to detail we expect to resolve on their actual (real-size) counterparts employing lower microwave windows which we expect to be used in λ and polarization imaging radars. This aspect of our study is also important for our future radar cross-section (diaphonization) studies.

During this period we continued to examine a group delay method for determining the object phase. The method as discussed elsewhere [29] measures the derivative of the object plane with respect to frequency. It provides an easy way of removing the unknown phase-range term and is related to measuring the instantaneous frequency of the return echo

from the moving target. An amplitude modulated group delay measurement method was analyzed in which amplitude modulated frequency swept (or stepped) illumination of the target is considered. Initially the target is assumed to be stationary. Later this requirement will be relaxed. Our interest in the AM group delay measurement is also motivated by its attractiveness for mmw scattering measurements in that it eliminates the long and lossy rigid waveguide connection between the receiver and the receiving antenna allowing its replacement by ordinary low frequency cabling and allowing thereby motion of the receiving antenna if needed as would be required in bistatic microwave or mmw imaging or scattering experiments. To appreciate the AM group delay experiment the following analytical considerations are presented:

Let

$$s_T(t) = A (1 + m \cos \omega_m t) \cos \omega_c t \quad (77)$$

be the amplitude modulated illumination signal transmitted towards the scattering object. Here ω_c is the carrier frequency which can be changed at will in discrete steps or continuously, ω_m is a fixed modulation frequency where $\omega_m \ll \omega$, $m \leq 1$ in the modulation index, and A is the amplitude.

The backscattered signal received at a monostatic receiver a distance R from the scatterer will be,

$$s_R(t) = \sqrt{\sigma} \left\{ A \cos \left[\omega_c \left(t - \frac{2R}{c} \right) + \phi(\omega) \right] + \frac{mA}{2} \cos \left[(\omega_c + \omega_m) \left(t - \frac{2R}{c} \right) + \phi(\omega_c + \omega_m) \right] + \frac{mA}{2} \cos \left[(\omega_c - \omega_m) \left(t - \frac{2R}{c} \right) + \phi(\omega_c - \omega_m) \right] \right\} \quad (78)$$

where σ is the radar cross-section of the target and ϕ is the phase shift due to scattering from the target, both being dependent on its shape and aspect

relative to the monostatic transmitter/receiver.

We expand next the phase $\phi(\omega)$ about any frequency ω_c in a Taylor series,

$$\phi(\omega) = \phi(\omega_c) + (\omega - \omega_c) \phi'(\omega_c) + \frac{1}{2!} (\omega - \omega_c)^2 \phi''(\omega_c) + \dots \quad (79)$$

where the primes designate differentiation with respect to ω . Now when $\phi(\omega)$ is slowly varying $\phi(\omega)$ can be approximated by the first two terms in (79).

Then

$$\phi(\omega_c \pm \omega_m) \approx \phi(\omega_c) \pm \omega_m \phi'(\omega_c) \quad (80)$$

Combining eqs. (83) and (85) we obtain,

$$\begin{aligned} s_R(t) = \sqrt{\sigma} A \cos \left[\omega_c \left(t - \frac{2R}{c} \right) + \phi(\omega_c) \right] \\ \cdot \{ 1 + m \cos \left[\omega_m \left(t - \frac{2R}{c} \right) + \omega_m \phi'(\omega_c) \right] \} \end{aligned} \quad (81)$$

Demodulation of this signal with an envelope detector yields,

$$s_m(t) = C \cos \left[\omega_m \left(t - \frac{2R}{c} \right) + \omega_m \phi'(\omega_c) \right] \quad (82-a)$$

or

$$s_m(t) = C \cos \left[\omega_m \left(t - \frac{2R}{c} - t_g(\omega_c) \right) \right] \quad (82-b)$$

which shows that the envelope is delayed by the propagation time $t_d = \frac{2R}{c}$ and by the group delay

$$t_g(\omega_c) = - d\phi(\omega_c)/d\omega_c. \quad (83)$$

While the propagation delay is a function of the object range, the group delay is seen to be dependent on object characteristics and as such bears information about it just as the phase $\phi(\omega_c)$ bears information about the object. Therefore

by measuring at the T/R the phase $\phi_m(\omega_c) = \omega_m \phi'(\omega_c)$ of the envelope in eq. (82-a) relative to the amplitude modulation signal we can obtain,

$$\phi_m(\omega_c) = \omega_m \left[\frac{2R}{c} - \phi'(\omega_c) \right] \quad (84)$$

Now if $\phi'(\omega_c)$ does not contain a constant level we can isolate it from (89) by d.c. filtering. For example, by passing the signal $\phi_m(\omega_c)$, as ω_c is linearly swept in time through a d.c. blocking filter to obtain $\omega_m \phi'(\omega_c)$. Since ω_m is known $\phi'(\omega_c)$ can be determined. This latter quantity can now be integrated between ω_{c_1} and ω_c where ω_{c_1} is the initial sweep frequency to obtain,

$$q(\omega_c) = \phi(\omega_c) - \phi(\omega_{c_1}) \quad (85)$$

and since $\phi(\omega_{c_1})$ is a constant, $\phi(\omega_{c_1})$ can also be removed by d.c. filtering to yield the target phase $\phi(\omega_c)$ which we seek.

The above procedure depends on the assumption that $\phi'(\omega_c)$ contains no constant level or equivalently that $\phi(\omega_c)$ does not contain a linear term in ω_c . It is well known that simple targets such as the cylinder and the sphere have a linear dependence of phase on frequency [24] and therefore the above procedure is not applicable to them. However most targets of practical interest are complex in shape and as such their phase will not contain a linear dependence on frequency. To see this consider the expression for the 3-D Fourier transform $\Gamma(\bar{p})$ of the object scattering $\gamma(\bar{r})$ as obtained by measuring the multiaspect frequency response of the scatterer, i.e.,

$$\Gamma(\bar{p}) = \int_{-\infty}^{\infty} \gamma(\bar{r}) e^{j\bar{p} \cdot \bar{r}} d\bar{r} \quad (86)$$

where $\bar{p} = \frac{2\omega_c}{c} \bar{l}_R$, \bar{l}_R being a unit vector pointing from the common origin, (phase center) on the scatterer towards the T/R and \bar{r} and \bar{p} are position vectors in scatterer space and Fourier space respectively. Consider next a target consisting of a collection of N scattering centers which we model for simplicity as a collection of point scatterers of strengths a_i located at $\bar{r} = \bar{r}_i$, $i=1,2 \dots N$, that is,

$$\gamma(\bar{r}) = \sum_{i=1}^N a_i \delta(\bar{r} - \bar{r}_i) \quad (87)$$

Combining eqs. (86) and (87) we obtain,

$$\Gamma(\bar{p}) = \sum_{i=1}^N a_i e^{j\bar{p} \cdot \bar{r}_i} \quad (88)$$

or

$$\Gamma(\omega_c, \bar{l}_R) = \sum_{i=1}^N a_i e^{j \frac{2\omega_c}{c} \bar{l}_R \cdot \bar{r}_i} \quad (89)$$

Thus at any T/R in a fixed direction \bar{l}_R the signal $\Gamma(\omega_c, \bar{l}_R)$ will be the sum of N phasors each of which will rotate in the complex plane as ω_c is changed with a different angular velocity because $\bar{l}_R \cdot \bar{r}_i$ is ordinarily different for each scatterer. The sum phasor therefore will not rotate with constant velocity and its phase can not vary linearly with ω_c which is the result we set out to show. The above simplified analysis also serves to show why information about a scattering object can be derived by changing the frequency of illumination but not by changing the phase because changing the phase of the illumination results in equal rotation of all phasors in eq. (89) and in a predictable rotation of the sum phasor that is independent of object characteristics.

As an illustrative example of the group delay method we consider the case of an object consisting of two point (or line) scatterers S_1 and S_2 spaced a distance d apart and situated a distance R in front of a monostatic T/R as shown in Fig. 47.

The received signal, taking the transmitted signal as phase reference, will be,

$$s_r(t) = A(\sqrt{\sigma_1} e^{-j2k(R - \frac{d}{2})} + \sqrt{\sigma_2} e^{-j2k(R - \frac{d}{2})}) \quad (90)$$

where σ_1 and σ_2 are the scattering strengths of scatterers S_1 and S_2 respectively. For simplicity we take $\sigma_1 = \sigma_2 = \sigma$. Equation (90) reduces then to,

$$\begin{aligned} s_r(t) &= 2A \sqrt{\sigma} e^{-j2kR} \cos kd \\ &= 2A \sqrt{\sigma} |\cos kd| e^{j\phi(k)} \end{aligned} \quad (91)$$

where

$$\phi(k) = -2kR + f(k) \quad (92)$$

and we have expressed

$$\cos kd = |\cos kd| e^{jf(k)} \quad (93)$$

with $f(k)$ representing the phase of $\cos kd$ which assumes the value of zero where $\cos kd > 0$ and π where $\cos kd < 0$ as illustrated in Fig. 48(c).

Noting next that $k = \omega_c / c$ and taking the derivative of eq. (92) with respect to ω_c we obtain by definition the group delay,

$$\tau_g(\omega_c) = \frac{\Delta}{d\omega_c} \frac{d\phi(\omega_c)}{d\omega_c} = -\frac{2R}{c} + \frac{df(\omega_c)}{d\omega_c} \quad (94)$$

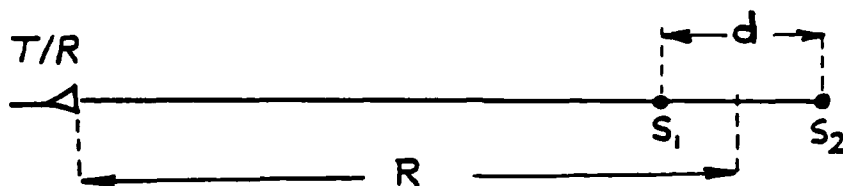


Fig. 47. Geometry referred to in determining the monostatic group delay and scattering phase of a two point or line scatterers.

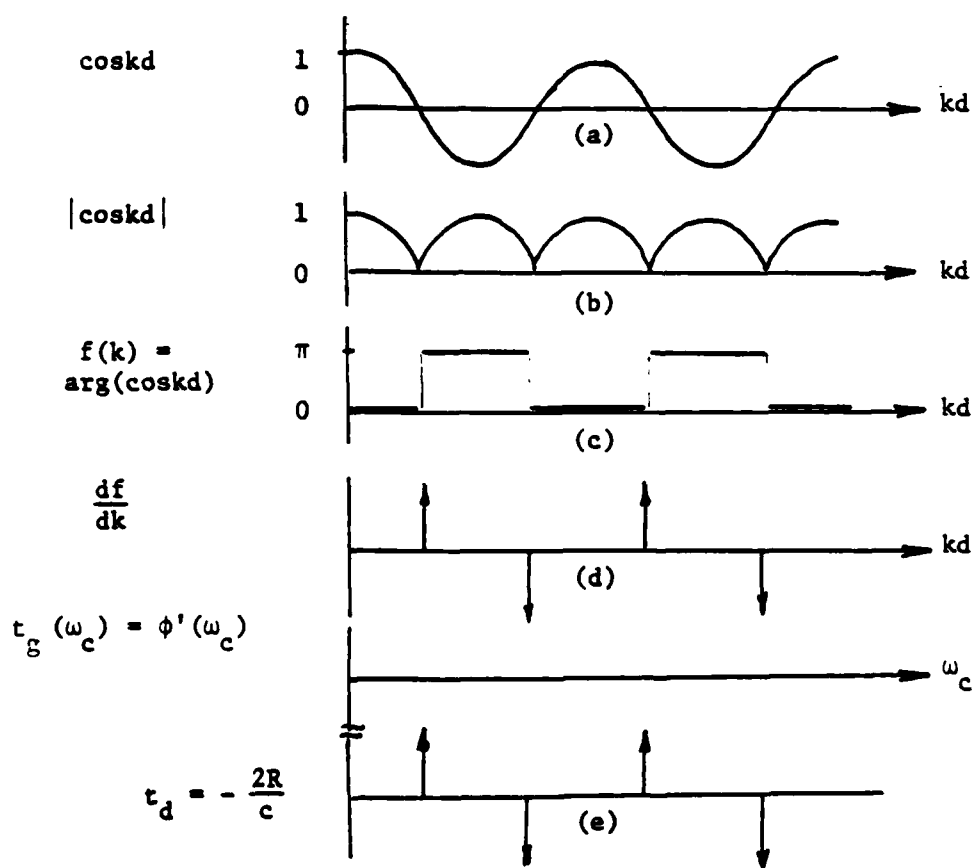


Fig. 48. Interpretation of the group delay associated with the example of Fig. 47.

shown in Fig. 48(e). The group delay in eq. (99) which can be d.c. filtered to obtain $df(\omega_c)/d\omega_c$ from which the phase $\text{Arg}(\cos kd)$ can be obtained by integration. It is clear the integration of the delta functions in $tg(\omega_c)$ in Fig. 48(e) will give back the "square wave" of the phase $f(k)$ or $f(\omega_c)$ shown in (c) of the same figure.

In view of the above analytical considerations we see that the group delay measurement and in particular the AM group delay measurement offers an attractive means for measuring the object phase $\phi(\omega_c) = \text{Arg } \Gamma(\omega_c)$. It is necessary however to examine the expected accuracy of the method. The resolution of the AM group delay measurement is given by [29]

$$\delta tg = - \frac{1}{360^\circ} \frac{\delta \phi_m}{f_m} \quad (95)$$

where f_m is the modulation frequency and $\delta \phi_m$ is the resolution of the phase meter used to measure the phase of the envelope of eq. (82).

The corresponding range resolution on the object is related to δtg through,

$$\delta R = |c \delta tg| = \frac{c}{360^\circ} \frac{\delta \phi_m}{f_m} \quad (96)$$

A high quality phase meter such as the Dranetz Model 305C with options 102, 103 and 104 is capable of measuring the phase of signals in the (5-700) KHz range with a resolution of 0.01° and a time constant of 1 msec (~ 1 KHz bandwidth). Assuming $f_m = 500$ KHz is used, eq. (101) predicts a range resolution of $\delta R = 1.6$ cm. Obviously both δtg and δR will depend on SNR (signal-to-noise ratio) [29]. However, for laboratory applications where the SNR can be kept quite high the degradation in resolution is expected to be negligible.

Our future research calls for the purchase of a Dranetz Model 305C phase meter with the options indicated for experimental study of the group-

delay method in λ and polarization diversity imaging. Special attention will be given to speedy data acquisition and extension of the method to millimeter wavelengths because of the simplification in cabling that can result then [29]. Initial work will focus on realizing a high value of f_m to keep δt_g and δR small and on comparison of the object phase obtained by the group delay method with the direct microwave phase measurement method used to date in our work. Once the experimental validity of the group-delay method is verified, it will be used in the acquisition of scattering data in our anechoic chamber facility using our standard test objects and the resulting imagery will be compared with earlier results. It is important to mention again that the method will be extremely important for: (a) simplifying bistatic data acquisition procedures (because of flexible cabling) where considerably larger amounts of object information is conveyed by the depolarized components of the scattered field than in the monostatic case and (b) for simplifying mmw laboratory implementation of λ and polarization diversity imaging.

3. DISCUSSION AND NEW RESEARCH DIRECTIONS

A detailed outline of our future research plan has been given in our 1983 AFOSR Research Proposal [29]. The research tasks proposed there include the following:

1. Studies in image understanding, enhancement and restoration
2. Dynamic data acquisition for the inverse SAR roof experiment
3. Image retrieval by backprojection
4. 3-D image reconstruction from incomplete data
5. Vector formulation of the dielectric inverse scattering problem
6. *Diaphonization* studies or reduction of the imaging and radar cross-sections for detection avoidance
7. Use of symmetries to increase information content to aid in object classification
8. Design of optimal interrogating signals
9. Information content in the presence of speckle noise
10. Formulation of a generalized theory of holography, SAR and inverse scattering
11. Production of a library of test data for use in image enhancement studies
12. Investigation of optimal data utilization techniques
13. New architectures for high throughput incoherent 2-D optical Fourier Transformation
14. 3-D Incoherent Imaging: New modalities

Progress during the current research period under a number of the tasks listed above has already been described in some detail in the preceding section (Section 2) of this annual report. The material in Section 2 represents important progress covering tasks 1,3,5,7 and 14. Some progress in tasks 2, 10 and 11 has also been achieved but not discussed explicitly. Our future proposed research will continue to address the above tasks as a whole with special attention to be given to those tasks not considered to-date and particularly to those discussed in Section 2 that have spawned new important findings. For example, emphasis will be placed in task 13 on high throughput incoherent Fourier transformation with particular attention to be given to the investigation of the Fourier camera concept and its relation to human and insect vision because of the advances this could produce in image understanding and processing. In task 2 special emphasis will be placed in the future on analytical and experimental study of efficient methods for: (a) data acquisition over extended spectral windows reaching into the millimeter wave range and (b) for realistic data acquisition in the presence of target motion. Task 14 on 3-D incoherent imaging will continue to be vigorously studied because of the new insights in image understanding it can produce as to its possible relation to the Fourier camera and human vision. The prospect of passive 3-D imaging of remote objects provides also a practical motive for this study. We expect that a generalized theory of 2-D and 3-D coherent and incoherent imaging based on projection theory will also be formulated during the coming period. The generalized projection approach may not only be confined to "hard" scattering bodies (conducting objects) but may also be extendable to "penetrable" dielectrics and as such will be of importance in our dielectric imaging work in task 5. Both a modified version of the

backprojection approach of image reconstruction already used in our back-projection reconstruction of conducting bodies and a *backpropagation* algorithm [23] will be considered in this task.

More specifically in the Fourier camera task we are interested in incoherent 2-D scenes characterized by their intensity $f(x,y)$ whose projection in any direction yields a positive-real one-dimensional function of a single coordinate. For example if the projection is taken on the x axis we have,

$$f_p(x) = \int_{-\infty}^{\infty} f(x,y) dy \quad (97)$$

with $f_p(x)$ being a positive-real function whose Fourier transform is,

$$F(\omega_x) = \int_{-\infty}^{\infty} f_p(x) e^{-j\omega_x x} dx = \int_{-\infty}^{\infty} f_p(x) [\cos\omega_x x + j \sin\omega_x x] dx \quad (98)$$

This shows that $F(-\omega_x) = F^*(\omega_x)$ where $*$ designates conjugation indicating that the negative frequency spectrum is obtainable from the positive frequency spectrum by conjugation. Therefore the sine/cosine mask of the Fourier camera need not include negative frequency components as was required previously in order to be able to Fourier transform color coded complex input functions [4]. This simplifies greatly mask fabrication, but more importantly it allows doubling the spatial frequency range of the camera for the same available detector array. Thus, for example, while for a detector array of 512 elements at the output of the camera, the range of spatial frequencies attainable with a sine/cosine mask consisting of positive and negative frequencies would be $-128 \leq f_x \leq 128$, (f_x being measured in cycles/unit length) a sine/cosine mask with positive frequencies only can yield Fourier transforms with spatial

frequency components in the $-256 \leq f_x \leq 256$ range provided that a suitable network for computing $F^*(\omega_x)$ from $F(\omega_x)$ is incorporated. Because $F(\omega_x)$ at the output of the Fourier camera is available as $\text{Re}F(\omega_x)$ and $\text{Im}F(\omega_x)$ separately the conjugate $F^*(\omega_x) = \text{Re}F - \text{Im}F$ can be easily formed. In this manner one can effectively double the throughput of the camera. Figure 49 shows sample sine and cosine screens with positive frequencies only produced in our laboratory. Note the same area modulation scheme devised for implementing a bipolar transmittance in incoherent light opto-electronically as described in [4] is employed. During the next research period we intend to implement a Fourier camera employing an available 512 element Reticon self-scanning detector array and a high precision positive frequency sine/cosine mask of maximum frequency $f_{x_{\text{max}}} = 256$ that will be fabricated outside our laboratory per our specifications. The cost of this fabrication is included in the proposed budget. The configuration of the Fourier camera we propose to implement and study is shown in Fig. 50. The required image rotation will be realized initially by rotating a photographic object scene as shown with the aid of a computer controlled stepper motor instead of using the dove prism used in earlier work until a precise method for mounting and centering the dove prism in the image rotator to increase precision is found. Schemes for such precision mounting are being considered by the staff of our machine shop. A simple electronic scheme for combining the outputs of the two halves of the detector array that provide the real and imaginary parts of $F(\omega)$ will be utilized to obtain $F(\omega)$ and $F(-\omega) = F^*(\omega)$ and to also form $|F(\omega)|^2$ for display purposes. The performance of the Fourier camera described will be evaluated and compared to the performance of a single channel of the

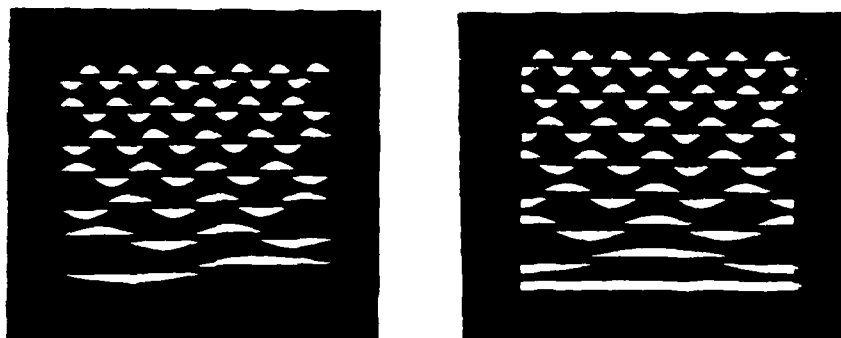


Fig. 49. Example of area modulated sine (left) and cosine (right) masks with positive frequencies only. $0 < f_x < 7$ cycles.

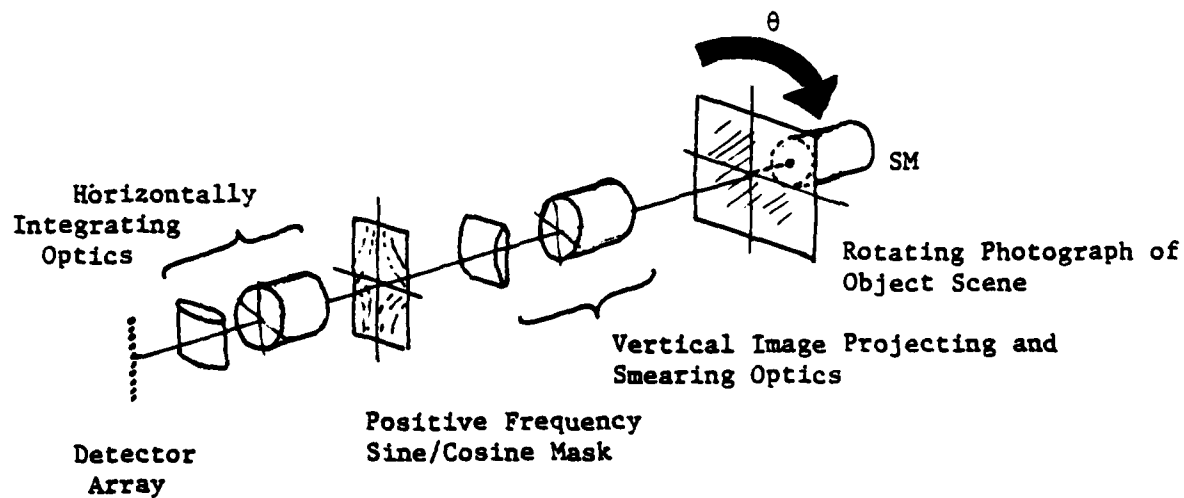


Fig. 50. Geometry of Fourier Camera

2-D incoherent opto-electronic Fourier transformation scheme shown in Fig. 51 proposed earlier [29] which employs a discrete Fourier transforming chip to perform the Fourier transform instead of the sine/cosine mask of the scheme of Fig. 50. This comparison is important since if performance in both schemes proves to be roughly equal the sine/cosine mask approach will be considerably more economical and will therefore be selected for implementing either of the high speed space-time multiplexed scheme depicted in Fig. 51 or a totally space-multiplexed version of it. A Fourier camera employing an array of identical parallel channels each forming the Fourier transform of a different angular projection of the object scene can provide a throughput exceeding 10^9 complex Fourier transforms per second employing two 5 MHz bandwidth 512 element detector arrays. This exceeds the throughput of the best digital array processor by three orders of magnitude and will open the way for real-time recording of the Fourier transform of complex scenes as in airborne mapping. The use of such a Fourier camera in a spot-light imaging mode will also enable, in accordance to the projection-slice theorem, the accessing of the 3-D Fourier space of the spotlighted ground detail. This capability furnishes a new approach to topographic mapping.

In another new task we intend to extend the capability of our measurement facility to bistatic measurements where we will be able to measure the object scattered wavefield over a wide range of aspect angles for a fixed direction of incident illumination by moving the receiving antenna. Bistatic measurements are important for gathering information about the object contained in the depolarized components of the scatterer. It is well known that the monostatic mode of data acquisition employed to date in our work yields considerably lower depolarization information than the bistatic mode [24] and yet it has provided noticeable image enhancement when the depolarized and the copolarized images were added. The availability of a bistatic measurement capability in our anechoic chamber facility will allow us to

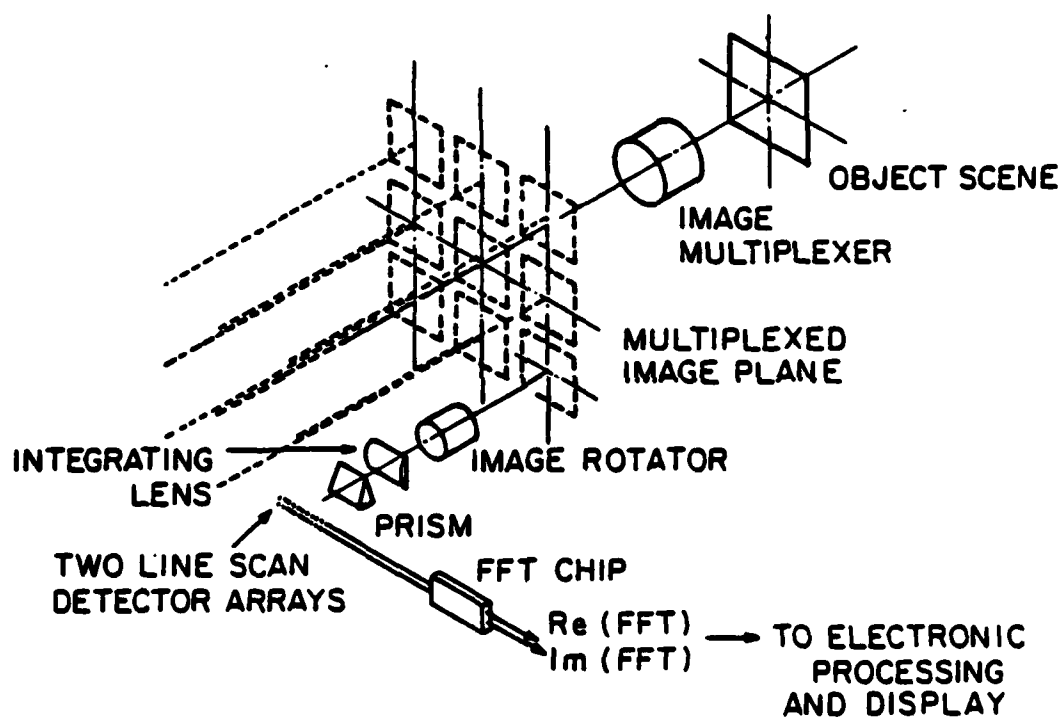
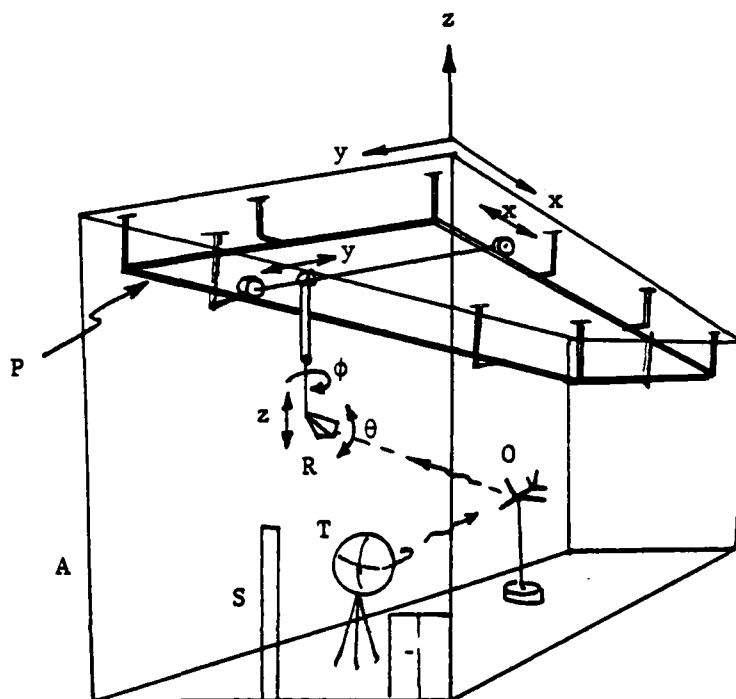


Fig. 51. High speed 2-D incoherent Fourier transformer based on the projection-slice theorem employing space-time multiplexing architecture and electronic FFT chips.

demonstrate cost-effectively the degree of image quality we can expect from bistatic imaging radar networks. Since the implementation of bistatic networks is considerably more complex than the monostatic network described and proposed in our work [21], the information yielded by this task will provide an idea of the cost-effectiveness of bistatic imaging radar networks.

Modification of our present microwave imaging facility to enable bistatic measurements requires the fabrication in our machine shop of a computer controlled x, y, z, θ, ϕ positioner for positioning the receiving antennas at any desired position and orientation relative to the scattering test object and the stationary illuminator antenna within the anechoic chamber. A simplified sketch of the positioner concept is given in Fig. 52 showing the positioner suspended rigidly from the ceiling of the anechoic chamber. An important consideration in the design is to use a minimum of metallic parts, using mostly plastic and reinforced fiber glass structures and materials that have low radar cross-section to keep down room clutter to a minimum. Note that our automated measurement techniques [21] incorporate removal of residual clutter from the measured data. As a result the inclusion of the positioner structure within the anechoic chamber will not compromise the accuracy of our scattering measurements. In the bistatic mode of data acquisition, unlike the monostatic mode, room clutter (i.e., background scattering data vs. frequency and polarization) must be measured and stored for all positions and orientations of the receiving antenna that will be used in data acquisition in order to be able to remove the effect of clutter from the acquired data properly. This requires precise positioning and orientation of the receiver horn. The planned positioner will therefore incorporate computer controlled stepper motor actuators, and linear bearings moving on precision shaft and



- A - Anechoic chamber
- T - Transmitting antenna (illuminator)
- O - Test Object (scatterer) mount on its own elevation over azimuth positioner.
- R - Positioner mounted receiving antenna
- P - Positioner frame
- S - Opening for interconnecting equipment outside and inside chamber

Fig. 52. Simplified sketch of proposed x, y, z, θ, ϕ positioner for use in bistatic λ and polarization diversity imaging studies.

rails. Most of the components and structures needed and their suppliers have been identified. An estimate of the cost of the positioner including labor has been included in the proposed budget. The incorporation of the bistatic positioner in our experimental microwave and millimeter wave anechoic chamber measurement facility will result in unique capabilities unavailable elsewhere. Virtually any microwave (and eventually millimeter wave) imaging confirmation can then be simulated cost-effectively by the facility employing scale models of the actual target or objects of interest. For example, to study the imaging of a moving scatterer the x, y, z, θ, ϕ positioner can be used in a programmed mode to move a test object of interest in front of a visually and manually tracking T/R antenna in a spot-light imaging mode to acquire realistic data at a fraction of the cost of acquiring the same data with an actual moving target.

In yet another aspect of our proposed research we will study the feasibility of further enhancing the quality of our polarization and symmetry enhanced images (see Section 2.3) through the use of iterative deconvolution based on the Gerchburg-Papoulis' algorithm [30],[31]. Because of the good SNR of our data and our a priori knowledge of object extent and spectral domain extent this algorithm is expected to yield good results. The aim here is to determine the degree of image improvement expected from applying this algorithm and other possible spectral estimation algorithms to realistic microwave scattering data. To facilitate our digital signal processing, and automated data acquisition and control effort an upgrading of the computer facilities of our Electro-Optics and Microwave-Optics laboratory as illustrated in Fig. 53 is being planned.

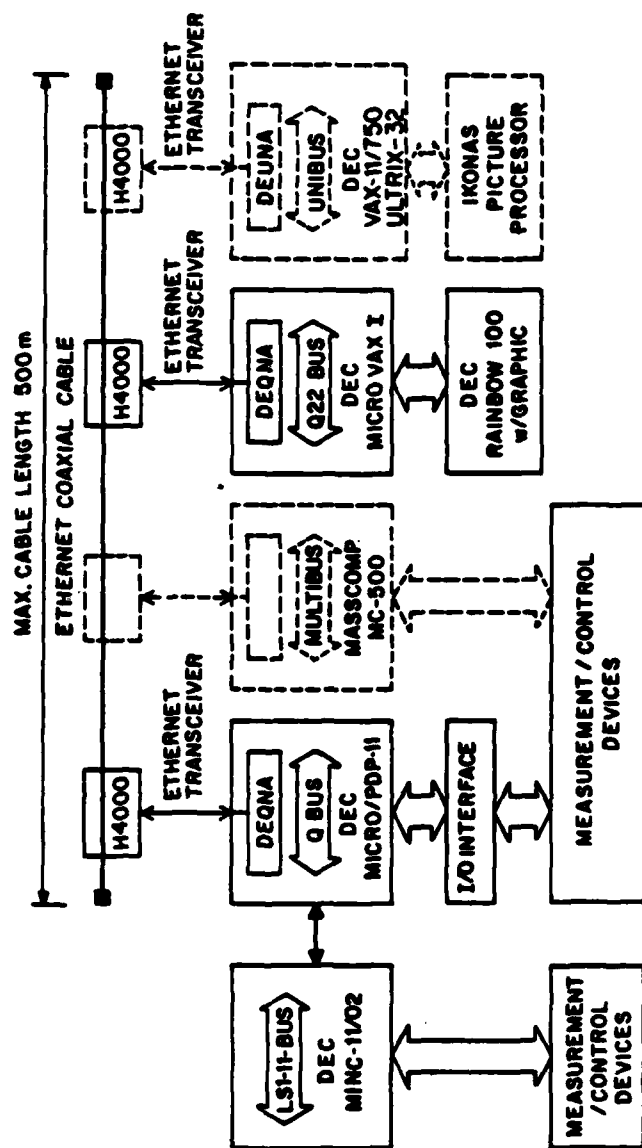


Fig. 53. ELECTRO-OPTICS & MICROWAVE-OPTICS LABORATORY
COMPUTER NETWORK CONFIGURATION

4. LIST OF PUBLICATIONS AND OTHER ACTIVITIES

During the past period of our research program the following papers were published or presented at national or international symposia:

1. N.H. Farhat, C. Yi Ho and Lie Szu Chang, "Projection Theorems and Their Application in Multidimensional Signal Processing", *Advances in Optical Information Processing*, G. Michael Morris, Editor, Proc. SPIE 388, pp. 140-149, (1983).
2. N.H. Farhat, T.H. Chu and C.L. Werner, "Tomographic and Projective Reconstruction of 3-D Image Detail in Inverse Scattering", Proc. 10-th Int. Optical Computing Conference, IEEE Cat. No. 83CH7880-40, pp. 82-88, (1983).
3. N.H. Farhat, C.L. Werner and T.H. Chu, "Prospects of 3-D Tomographic Imaging Radar Networks", Proc. of the 1983 URSI Symposium on Electromagnetic Theory, Santiago de Compostella, Spain, pp. 297-301 (1983). (An expanded version of this paper has also been submitted to *Radio Science* by invitation).
4. N.H. Farhat, "Projection Imaging of 3-D Microwave Scatterers with Near Optical Resolution", in *Indirect Imaging*, J.A. Roberts (Ed.) Cambridge University Press, (1984).
5. D.L. Jaggard and K.E. Olson, "Analytical and Numerical Strategies for Inverse Scattering from Almost Periodic Media", presented at the 3rd Annual Benjamin Franklin Symposium on Advances in Antenna and Microwave Technology", Philadelphia (1983).
6. N.H. Farhat, D.L. Jaggard, T.H. Chu, D.B. Ge and S. Mankoff, "Microwave Imaging of 3-D Dielectric Bodies", presented at the 3rd Annual Benjamin Franklin Symposium on Advances in Antennas and Microwave Technology", Philadelphia, (1983).
7. D.L. Jaggard and A.K. Jordan, "Inversion Theory for Almost Periodic Media", Proc. of the 1983 URSI Symposium on Electromagnetic Theory, Santiago de Compostella, Spain, pp. 263-266 (1983). (An expanded version of this paper has also been submitted to *Radio Science* by invitation.)
8. N.H. Farhat, D.L. Jaggard, T.H. Chu, D.B. Ge and S. Mankoff, "Microwave Tomographic and Projection Imaging of 3-D Dielectric Bodies", presented at the 1983 International IEEE/AP Symposium and National Radio Science Meeting, Houston (1983).
9. A.K. Jordan, S. Ahn and D.L. Jaggard, "Applications of Almost-Periodic Functions to Inverse Scattering Theory", presented at the NATO Advanced Research Workshop on Inverse Scattering Methods for Electromagnetic Imaging (1983).

10. D.B. Ge, D.L. Jaggard and H.N. Kritikos, "Perturbational and High Frequency Profile Inversion", *IEEE Trans. AP-29*, (1983).

Also, during this period the following Thesis were completed.

1. Lie Szu Chang, "High-Speed Incoherent Opto-Electronic Fourier Transforms", Msc Thesis, University of Pennsylvania, (1983).
2. K.E. Olson, "A Numerical Method for Dispersionless Dielectric Profile Reconstruction", MSc Thesis, University of Pennsylvania, (1983).

Also during this period the following paper was presented at the 13-th Congress of the International Commission for Optics, Sapporo, Japan, Aug. 1984:

1. N.H. Farhat and T.H. Chu, "Tomography and Inverse Scattering"
- and at the XXI General Assembly of the International Union of Radio Science, Florence, Italy, August/September 1984:

1. D.L. Jaggard, et. al., "Tomographic Microwave Imaging".

Papers Submitted and Accepted for Publication:

1. N.H. Farhat, C.L. Werner and T.H. Chu, "Prospects for Three-Dimensional Projective and Tomographic Imaging Radar Networks", Radio Science.
2. D.L. Jaggard and A.K. Jordan, "Inversion Theory for Almost Periodic Media", Radio Science,

Other Activities

During this period a group from the Western Space and Missile Center, Vandenberg, AFB, headed by Mr. Edgar Hall, visited our Laboratory on Aug. 17, 1983.

Dr. Farhat participated in the ERIM/Army Research Office Workshop on "Limits of Passive Imaging" held at Mackinac Island, Mich., May 1983 and spent a sabbatical leave at Caltech and JPL working on various aspects of radar imaging and optical information processing related to the research reported here.

5. REFERENCES

1. G.N. Ramachandran and A.V. Lakshminarayan, "Three Dimensional Reconstruction from Radiographic and Electron Micrographic Application of Convolution Instead of Fourier Transforms", Proc. Mat. Acad. Sci. U.S., Vol. 68, pp. 2236-2240, 1970.
2. C.C. Aleksoff, I.J. LaHaie and A.M. Tai, "Optical-Hybrid Backprojection Processing", Proc. 10-th Int. Opt. Computing Conference, IEEE Cat. No. 83CH1880-4, p. 89.
3. D. Munson Jr., J.D. O'Brien and W.K. Jenkins, "A Tomographic Formulation of Spotlight-Mode Synthetic Aperture Radar", Proc. IEEE, Vol. 71, Aug. 1983, pp. 917-925.
4. N.H. Farhat, et. al., "Projection Theorems and Their Application in Multi-Dimensional Signal Processing", in Advances in Optical Information Processing, G. Michael Morris (Ed.), Proc. SPIE, Vol. 368, pp. 140-149, (1983).
5. A. Papoulis, Systems and Transforms in Optics, Table 1-2, pp. 66, McGraw-Hill, New York, 1963.
6. F.W. Campbell and J.G. Robson, "Application of Fourier Analysis to the Visibility of Gratings", J. Physiol. (London) Vol. 197, pp. 551-556, (1968).
7. M.B. Sachs, J. Nachmias and J.G. Robson, "Spatial-Frequency Channels in Human Vision", J. Opt. Soc. Am., Vol. 61, pp. 1176-1186, Sept. 1971.
8. Bahaa E.A. Saleh, "Optical Information Processing and the Human Visual System", in Applications of Optical Fourier Transforms, H. Stark (Ed.), Acad. Press, New York, 1982.
9. D. Casasent and W-T Chang, "Generalized Chord Transformation for Distortion-Invariant Optical Pattern Recognition", App. Optics, Vol. 22, pp. 2087-2094, July 1983.
10. H.J. Caulfield and M.H. Weinberg, "Computer Recognition of 2-D Patterns Using Generalized Matched Filters", App. Optics, Vol. 21, pp. 1699-1704, May 1982.
11. J.J. Hopfield, "Neural Networks and Physical Systems with Emergent Collective Computational Abilities", Proc. Natl. Acad. Sci., USA, Vol. 79, pp. 2554-2558, April 1982.
12. M. Born and E. Wolf, Principles of Optics, 3rd (revised) edition, Pergamon Press, pp. 508-512, New York, 1965.
13. A. Devaney, "Optical Coherence: A Self-Perpetuating Science", Optical Spectra, pp. 37-41, Oct. 1979.

References (Cont'd)

14. A.V. Oppenheim and R.W. Schaffer, Digital Signal Processing, Prentice Hall Inc., Englewood Cliffs, 1975.
15. R.W. Gerchberg, "Super-Resolution Through Error Energy Reduction", Opt. Acta, Vol. 21, pp. 709-720, 1974.
16. A. Papoulis, "A New Algorithm in Spectral Analysis and Bandlimited Extrapolation", IEEE Trans. on Circuits and Systems, Vol. CAS-22, pp. 735-742, Sept. 1975.
17. G.N. Balanis, "Inverse Scattering Theory: Determination of Inhomogeneities in Sound Speed", J. Math. Phy., Vol. 23, pp. 2562-2568, 1982.
18. D.L. Jaggard and K.E. Olson, "Numerical Reconstruction for Dispersionless Refractive Profiles", submitted for publication.
19. N.H. Farhat, "High Resolution 3-D Tomographic Imaging by Wavelength and Polarization Diversity", University of Pennsylvania Research Proposal, Submitted to Air Force Office of Scientific Research, March 16, 1982.
20. R.M. Mersereau and A.V. Oppenheim, "Digital Reconstruction of Multi-dimensional Signals From Their Projections", Proc. IEEE, Vol. 62, pp. 1319-1338, October 1978.
21. N. Farhat, T.H. Chu and C.L. Werner, "Prospects of 3-D Tomographic Imaging Radar Networks", Proc. of the 1983 URSI Symposium on Electromagnetic Theory, Santiago De Compostella, Spain (1983).
22. "Vector Measurement of High Frequency Networks" Hewlett Packard Application Note, Sept. 1978, pp. 53-61.
23. A.J. Devaney, "Inverse Source and Scattering Problems in Ultrasonics", Proc. of the 1982 Ultrasonics Symposium, IEEE publication (1982).
24. G.T. Ruck, et. al., Radar Cross-Section Handbook, G.T. Ruck (Ed.), Vol. 1, Ch. 2., Plenum Press, New York (1970).
25. N.H. Farhat, "High Resolution 3-D Tomographic Imaging by Wavelength and Polarization Diversity", Univ. of Pennsylvania Proposal submitted to AFOSR, April 1981.
26. N.H. Farhat, "High Resolution 3-D Wavelength Diversity Imaging", University of Pennsylvania, Final Report, Prepared under grant No. AFOSR-81-0281, Sept. 1981.
27. T.H. Chu, "Optimal Methodologies in Inverse Scattering Utilizing Wavelength, Polarization, and Angular Diversity", University of Pennsylvania, PhD dissertation, 1983.

References (Cont'd)

28. N. Farhat, "High Resolution 3-D Tomographic Imaging by Wavelength and Polarization Diversity", Univ. of Pennsylvania Annual Report, prepared under grant No. AFOSR-81-0240B, July 5, 1984.
29. N.H. Farhat, "Research in Image Understanding as Applied to 3-D Microwave Tomographic Imaging with Near Optical Resolution", University of Pennsylvania Renewal Proposal AFOSR-81-0240B, March 1984.
30. R.W. Gerchberg, "Super-Resolution Through Error Energy Reduction", Opt. Acta, Vol. 21, pp. 709-720, 1974.
31. A. Papoulis, "A New Algorithm in Spectral Analysis and Bandlimited Extrapolation", IEEE Trans. on Circuits and Systems, Vol. CAS-22, pp. 735-742, Sept. 1975.

END

FILMED

3-85

DTIC